



TECHNISCHE  
UNIVERSITÄT  
WIEN

DIPLOMARBEIT

# Experimental Physics with a Superconducting Atomchip

ausgeführt am Atominstitut



der Technische Universität Wien  
Fakultät für Physik

unter der Anleitung von  
**Univ.Prof. Dipl.-Ing. Dr.techn. Hannes-Jörg Schmiedmayer**  
und  
**Projektass. Dr.rer.nat Fritz Diorico MSc.**  
**Projektass. Dr.techn. Dipl.-Ing. Stefan Minniberger**

durch

**Thomas Weigner**

Matrikelnummer: 00822106

Ettenau 5  
5121 Ostermiething

Wien, am 21.09.2018

*"Life would be tragic, if it weren't so funny!"*  
STEPHEN HAWKING



# Abstract

Combining two distinct different things to create one more powerful hybrid system is a well known method. A hybrid quantum system of ultra cold atoms and superconductors, based on this method, has the advantage that the sub systems complement each other. This thesis reports on a complex experimental setup with the aim to realize such a hybrid quantum system and all the prospects it has. To combine ultra cold atoms and superconductors, laser cooled atoms are magnetically transported into a 4 K cryostat. This makes the setup rather complicated, while at the same time giving the opportunity to use the magnetic conveyor belt and the cryogenic environment as a feature. The magnetic transport might be employed to recombine atomic clouds and superconducting properties probed with cold atoms, lead to novel techniques to trap atoms. In order to realize strong coupling in the planned hybrid quantum system, the experimental setup was improved for stability and the time spent on maintenance was greatly reduced. The first superconducting resonators were designed and the evaporative cooling towards a BEC has been optimized.

## Zusammenfassung

Das Kombinieren zweier verschiedener Dinge, um ein überlegenes hybrides System zu erschaffen, ist eine allseits bekannte Methode. Ein hybrides Quantensystem, basierend auf dieser Methode, bestehend aus ultra-kalten Atomen und Supraleitern, hat den Vorteil, dass sich die Teilsysteme gegenseitig ergänzen würden. Diese Diplomarbeit berichtet über einen komplexen experimentellen Aufbau mit dem Ziel, solch ein hybrides Quantensystem zu realisieren und dessen Perspektiven. Um ultra-kalte Atome und Supraleiter zu kombinieren, werden Laser gekühlte Atome magnetisch in einen 4 K Kryostaten transportiert. Obwohl dies den Aufbau ziemlich kompliziert macht, ergibt sich daraus die Möglichkeit, das magnetische Förderband und die kryogene Umgebung für weitere Aspekte zu verwenden. Der magnetische Transport könnte verwendet werden, um atomare Wolken zu kombinieren und Eigenschaften von Supraleitern können mittels ultra-kalter Atome untersucht werden, was zu neuen Techniken um Atome zu fangen führt. Um starke Kopplung in dem angedachten hybriden Quantensystem zu erreichen, wurde der experimentelle Aufbau in seiner Stabilität verbessert und die notwendige Zeit für Instandhaltung drastisch reduziert. Weiters wurden die ersten supraleitenden Resonatoren entworfen und das Verdampfungskühlen, mit dem Ziel ein BEC zu erzeugen, stark verbessert.

# Contents

<b>1. Introduction</b>	<b>1</b>
1.1. Ultra Cold Atoms . . . . .	1
1.2. Superconductors . . . . .	2
1.3. Hybrid Quantum Systems . . . . .	2
<b>2. Theoretical Background</b>	<b>4</b>
2.1. Rubidium . . . . .	4
2.1.1. $^{87}\text{Rb}$ Hyperfine Structure . . . . .	4
2.1.2. ZEEMAN Shift . . . . .	7
2.1.3. Natural Linewidth . . . . .	7
2.1.4. Thermal Linewidth . . . . .	8
2.1.5. Clock State . . . . .	9
2.2. Cooling of Atoms to ultra cold Temperatures . . . . .	10
2.2.1. DOPPLER-Free Spectroscopy . . . . .	11
2.2.2. Laser Cooling . . . . .	12
2.2.3. Sub-DOPPLER-Cooling . . . . .	15
2.3. Magnetic Trapping . . . . .	16
2.3.1. Neutral Atoms in Magnetic Fields . . . . .	16
2.3.2. Quadrupole Trap . . . . .	17
2.3.3. IOFFE-PRITCHARD Trap . . . . .	18
2.3.4. Magnetic Trapping with Wires and Atomchips . . . . .	18
2.3.5. Loss Mechanisms . . . . .	19
<b>3. Experimental Setup</b>	<b>22</b>
3.1. Laser Setup . . . . .	23
3.1.1. Laser Configurations . . . . .	23
3.1.2. Locking Schemes for our Lasers . . . . .	25
3.1.3. Laser Units . . . . .	27
3.2. Optical setup . . . . .	29
3.2.1. Imaging Setup . . . . .	30
3.3. MOT Chamber . . . . .	33
3.3.1. Dispenser . . . . .	34

3.4. Atom Transport . . . . .	35
3.4.1. Magnetic Conveyor Belt . . . . .	36
3.5. Cryogenic Setup . . . . .	39
3.5.1. Cryostat . . . . .	40
3.5.2. Heat Shielding . . . . .	42
3.5.3. Wiring in Cryogenic Environment . . . . .	43
3.6. Antennas . . . . .	46
3.6.1. RF Setup . . . . .	46
3.6.2. Microwave Antenna . . . . .	48
3.7. Superconducting Atomchip . . . . .	48
3.7.1. Chip Contacting . . . . .	50
3.8. Experiment Control and Monitoring . . . . .	51
3.8.1. ADWIN Controller . . . . .	51
3.8.2. Experimental Controller . . . . .	52
3.8.3. Monitoring . . . . .	53
<b>4. Towards Hybrid Quantum System</b>	<b>55</b>
4.1. Atomchip loading . . . . .	55
4.2. Ultra Cold Atoms in a Superconducting Environment . . . . .	57
4.2.1. Trapping Parameters . . . . .	57
4.2.2. Towards a Degenerated Quantum gas . . . . .	60
4.3. Superconducting Microwave resonators . . . . .	63
4.3.1. Probe Stick . . . . .	63
4.3.2. Resonators . . . . .	64
<b>5. Novel Superconducting Chip Traps</b>	<b>67</b>
5.1. Current Distribution Modelling . . . . .	67
5.2. Trap Distance Programming . . . . .	69
5.3. Zero Transport Current Traps . . . . .	72
<b>6. Atomic Recombination</b>	<b>73</b>
6.1. Transport currents . . . . .	74
6.1.1. Aspect Ratio . . . . .	74
6.1.2. Calculation . . . . .	75
6.1.3. Horizontal Section . . . . .	76
6.1.4. Vertical Section . . . . .	76
6.1.5. Coil to Current Source Transducer . . . . .	77
6.2. Magnetic Transport Calculator . . . . .	80
6.2.1. Temporal Behavior of transport . . . . .	83
6.2.2. Resulting Currents . . . . .	86

6.3. Attempted Recombination Scheme . . . . .	88
<b>7. Outlook</b>	<b>90</b>
7.1. Hybrid Quantum System . . . . .	90
7.2. Superconducting Atomchip Prospects . . . . .	91
7.3. Atomic Recombination . . . . .	92
<b>Appendix</b>	<b>94</b>
A. Magnetic Transport Calculator . . . . .	94
A.1. main.cpp . . . . .	95
A.2. header.h . . . . .	104
A.3. poly.cpp . . . . .	107
B. $^{87}\text{Rb}$ Zeeman Sublevels . . . . .	110
C. Young Atomic Opticians Conference Poster . . . . .	114
<b>List of Figures</b>	<b>115</b>
<b>List of Tables</b>	<b>117</b>
<b>List of Symbols</b>	<b>118</b>
<b>References</b>	<b>122</b>

# 1. Introduction

Combining two fields of Physics or phenomena often lead to major discoveries. This is a well known tradition throughout the history of Physics. The idea of hybrid quantum systems emerged naturally from the recent advancements in quantum optics and computing. This idea of combining two different quantum systems follows that tradition, with the goal of potentially harnessing the advantages of both sub systems.

Based on the initial proposal for this experiment [1], the **Quantum-Interconnect** (QuIc) experiment aims to combine the unique properties and advantages of superconducting resonators and ultra cold atoms. A superconducting atomchip is the heart of this setup. The ultimate goal is to show strong coupling between the  $^{87}\text{Rb}$  hyperfine clock transition in a BOSE-EINSTEIN condensate and a superconducting microwave resonator. The advantage of this would be the long coherence times of ultra cold atoms combined with the fast coupling rates of microwave photons in superconductors, leading to possible applications in quantum information as memory or interface.

In this thesis, the basic Physics this experiment builds on, its prospects, novel techniques discovered [2–4] and the setup of this experiment, are discussed.

## 1.1. Ultra Cold Atoms

Since the creation of the first degenerate quantum gas [5], a huge field investigating and utilizing ultra cold atoms, has evolved. Through BOSE-EINSTEIN condensates and degenerate FERMI gases, physicists have gained access to investigate the wave properties of matter in macroscopic many body systems. The experimental techniques ultra cold atom experiments have developed so far, can also be used to simulate other quantum mechanical systems, e.g solids in optical lattices, artificial gauge fields, quantum electronics, etc..

Since the invention of atomchips [6], they have evolved to a well established experiment platform, which allows physicists to precisely trap and control clouds of ultra cold atoms. Naturally, it makes sense to continue developing atomchips further and use e.g new materials such as superconductors.

## 1.2. Superconductors

Superconductors have fascinating properties and are far more complex than a conductors with zero resistance. They are an intense research field and their applications span from single photon detectors to coils creating very strong magnetic fields, as used in particle accelerators like LHC or magnetic resonance tomography. The well known way to describe superconductivity is the BARDEEN COOPER SCHRIEFFER (BCS) theory [7]. It is based on long range electron interaction via phonons, which are called COOPER pairs, which are bosonic quasi particles.

In the field of quantum information, superconductivity is also commonly employed e.g. in the form of JOSEPHSON junctions. These are two layers of superconductors with a thin insulator in between. They are the basic building blocks for more complex structures like superconducting quantum interference devices (SQUID) and superconducting quantum circuits (SQC). These exhibit very strong coupling through the big electric dipole moments involved and scaling to an actual computer is feasible. However, they have the disadvantage of short coherence times and therefore can only realize short lived Q-bits.

## 1.3. Hybrid Quantum Systems

Many interesting physics can be investigated by letting two different quantum systems strongly interact. If this is done in a clever way, one can fabricate a system where each subsystems' advantages are exploited and the respective disadvantage of the other system is countered. Furthermore, to employ quantum technologies in some sort of quantum internet, it will be necessary to interconnect different quantum systems [8]. In such a network, quantum information also needs to be stored. To build such a quantum memory with long coherence times, hybrid systems are a promising approach [9].

In the pursuit of building a quantum computer, which came a long way since [10] and [11], superconducting quantum circuits seem to be very promising [12]. One day they could for example, factorize large integer numbers very efficiently with means of the SHOR algorithm [13]. However, as discussed earlier, short coherence times would make it difficult to save intermediate calculation steps. Introducing another quantum system with long coherence times, would bridge the missing quantum memory for such superconducting circuits [14, 15]. One example, with an exceptional long lifetime would be a spin ensemble of nitrogen vacancies in a diamond, coupled to a resonator [16]. Ultra cold neutral atoms have an even longer coherence time and and quantum

information can be transferred to and read from them by microwave transitions [17]. Magnetically trapped ultra cold atoms on an atomchip are especially an interesting experiment platform as already explained in section 1.1. Therefore, atoms are also interesting for hybrid quantum systems. Considering this, a hybrid quantum system based on an ensemble of ultra cold atoms and a superconducting microwave resonator on an atomchip, as suggested in [1, 18], is very promising.



## 2. Theoretical Background

In this chapter, some physical concepts relevant for this thesis are reviewed. First, the level structure of  $^{87}\text{Rb}$  is reviewed. Based on this, the basic principles of laser cooling are explained. The last section explains how neutral atoms are magnetically trapped in various trap geometries.

### 2.1. Rubidium

In cold atoms experiments,  $^{87}\text{Rb}$  is the most widely used species. Due to its simple one valence electron structure and physical properties, Rubidium is well suited for quantum optical experiments and laser cooling. Furthermore, the wavelength of the D<sub>2</sub> line (about 780 nm) is easy to produce, since lasers diodes and optical elements are easily available for this Wavelength. Rubidium can be released well controlled into an experiment chamber via a dispenser (see section 3.3.1). DOPPLER-free spectroscopy resolving the hyperfine structure is relatively easy to build (see section 2.2.1), since Rubidium vapour cells can operate at room temperature. For this experiment,  $^{87}\text{Rb}$ 's clock state (see section 2.1.5) in the ground state  $5^2\text{S}_{1/2}$  between  $F = 1, m_F = -1$  and  $F = 2, m_F = 2$  is important for of the proposed hybrid quantum system.

Rubidium has a stable and quasi stable isotope  $^{85}\text{Rb}$  and  $^{87}\text{Rb}$ , whereas  $^{87}\text{Rb}$  has a  $\beta^- + ^{87}\text{Sr}$  decay with an half-life of  $4.92 \times 10^{10}$  yr [19], with a natural abundance of 27.83%  $^{87}\text{Rb}$ . The D2 lines of both isotopes ( $^{87}\text{Rb}$  780.241 209 686(13) nm,  $^{85}\text{Rb}$  780.241 368 271(27) nm) are just separated by  $\approx 78.1$  MHz [20][21]. However the hyperfine splitting into  $F = 2, F = 3$  for  $^{85}\text{Rb}$  with 3.05 GHz and  $F = 1, F = 2$  for  $^{87}\text{Rb}$  with 6.83 GHz, allows to resolve all four D2 lines of  $^{85}\text{Rb}$  and  $^{87}\text{Rb}$ . In fig. 3.3, the two DOPPLER valley of the  $F = 2$  transition of the  $^{87}\text{Rb}$  D2 line is shown.

#### 2.1.1. $^{87}\text{Rb}$ Hyperfine Structure

Through technical advancement, spectroscopes became more sensitive over the years. With higher resolutions, it was observed that spectral lines shift and split into finer lines, therefore called fine structure. Apart of relativistic corrections and the DARWIN

## 2. Theoretical Background

---

for S-orbitals term due to the HEISENBERG uncertainty, the fine structure includes a splitting into sub-levels due to coupling of the orbital angular momentum  $\mathbf{L}$  with the electron spin  $\mathbf{S}$  to the total electron angular momentum  $\mathbf{J}$ .

The protons and neutrons in an atomic nucleus, also have a spin. Therefore a resulting total nuclear spin  $\mathbf{I}$  interacts with  $\mathbf{J}$  and couples to the total angular momentum

$$\mathbf{F} = \mathbf{J} + \mathbf{I}. \quad (2.1)$$

Since,  $\mathbf{I}$  is magnitudes smaller than  $\mathbf{J}$  the energy splitting by is very small and therefore called hyperfine structure. The eigenvalues of  $\hat{\mathbf{F}}$  are expressed via

$$\langle \hat{\mathbf{F}} \rangle = \hbar \sqrt{F(F+1)} \quad (2.2)$$

and the possible values are in the range

$$|J - I| \leq F \leq J + I. \quad (2.3)$$

Considering now also the effects of the hyperfine structure the manifold of the  $^{87}\text{Rb}$  D1 and D2 line looks as seen in fig. 2.1.

## 2. Theoretical Background

---

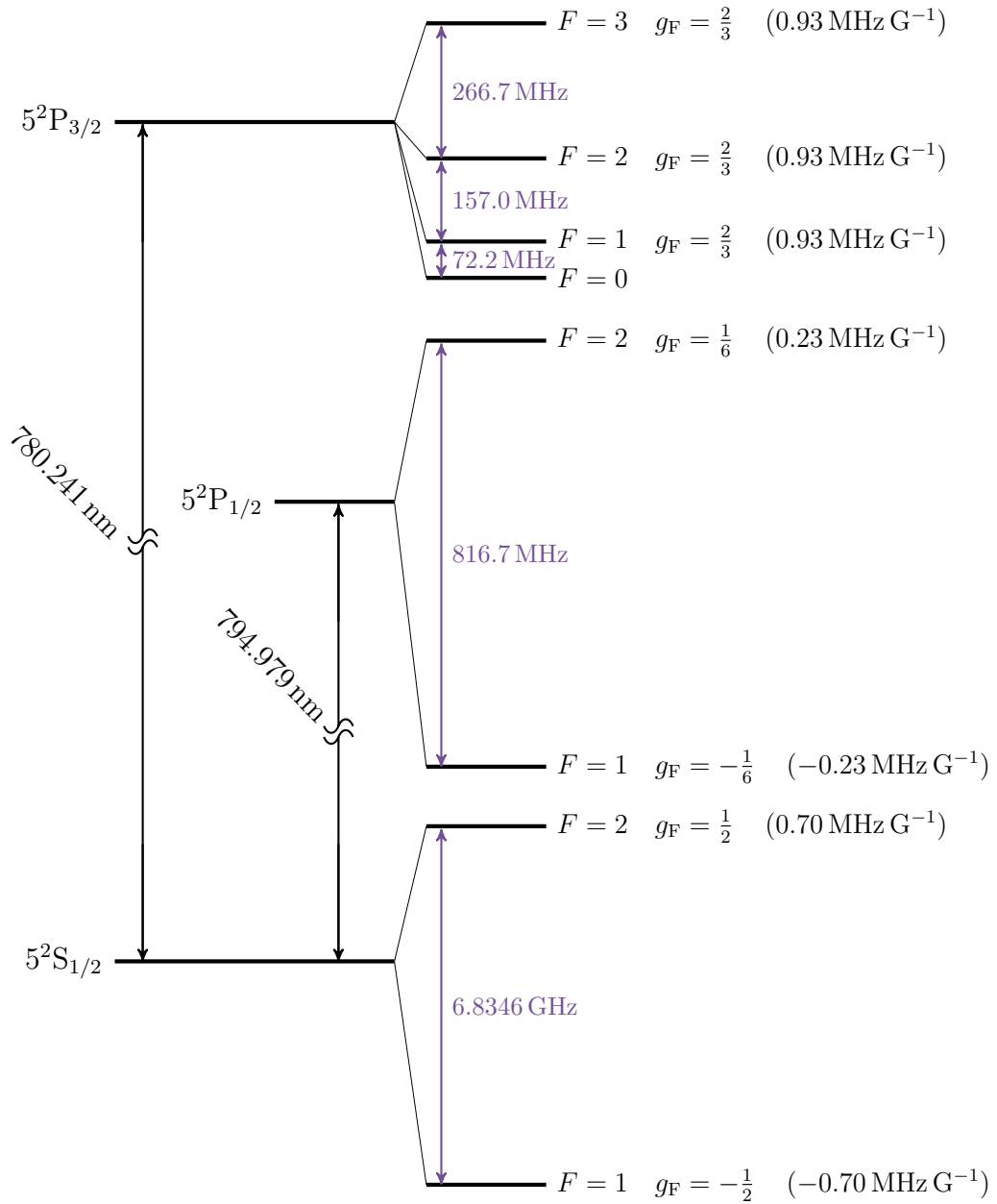


**Figure 2.1.:**  $^{87}\text{Rb}$  hyperfine structure of the D1 and D2 line with their respective  $g_F$  factors and linear ZEEMAN splitting coefficients. The excited states are 10 times magnified in relation to the ground state.

### 2.1.2. ZEEMAN Shift

In a  $^{87}\text{Rb}$  atom, exposed to an external magnetic field the valence electron's magnetic moment as well as the nucleus' magnetic moment interact with the external field  $H$ . The interaction term called ZEEMAN Hamiltonian can be, according to [22] written, in first order as

$$\hat{H} = -(\boldsymbol{\mu}_L + \boldsymbol{\mu}_S + \boldsymbol{\mu}_I) \mathbf{B}, \quad (2.4)$$

where  $\boldsymbol{\mu}_L$ ,  $\boldsymbol{\mu}_S$ ,  $\boldsymbol{\mu}_I$  are the magnetic moments of the electron angular momentum, electron spin, and nucleus spin. As shown in appendix B this Hamiltonian leads to a splitting with an energy gap of

$$\Delta E = g_F m_F \mu_B B_z. \quad (2.5)$$

This shows that the ZEEMAN splitting is in good approximation linear with  $g_F$  for small magnetic fields, which is called anomalous ZEEMAN shift. At strong magnetic fields this does not hold and the magnetic splitting is called PASCHEN-BACK-effect, which disrupts the coupling between  $S$  and  $L$ . In between, the exact energy shift due to external magnetic fields is more complex. However, for the ground state is given by the BREIT-RABI formula, from [20, 23],

$$E_{I \pm \frac{1}{2}, m_F} = -\frac{\Delta E_{\text{hfs}}}{2(2I+1)} + g_I m_F \mu_B B_z \pm \frac{\Delta E_{\text{hfs}}}{2} \sqrt{1 + \frac{4m_F (g_J - g_I) \mu_B B_z}{(2I+1) \Delta E_{\text{hfs}}} + \left( \frac{(g_J - g_I) \mu_B B_z}{\Delta E_{\text{hfs}}} \right)^2}, \quad (2.6)$$

where  $\Delta E_{\text{hfs}}$  is the hyperfine splitting without external fields. In fig. 2.2 it is plotted for the  $^{87}\text{Rb}$   $5^2\text{S}_{1/2}$  ground state. This clearly shows that we can work with the anomalous ZEEMAN splitting, which is sufficient to understand and simulate magnetic trapping.

### 2.1.3. Natural Linewidth

Due to HEISENBERG's uncertainty principle

$$\frac{\hbar}{2} \leq \hat{x} \cdot \hat{p}, \quad (2.7)$$

quantum mechanical transition are not infinitely narrow. Therefore, when the energy of a quantum mechanical system is exactly known, it would be static. With this, electron excitations can decay spontaneously. Describing excited electrons as an harmonic oscillator, one finds the oscillation amplitude has an exponential decay. Because of this, the radiated EM-field is not monochromatic. The spectrum can be calculated by

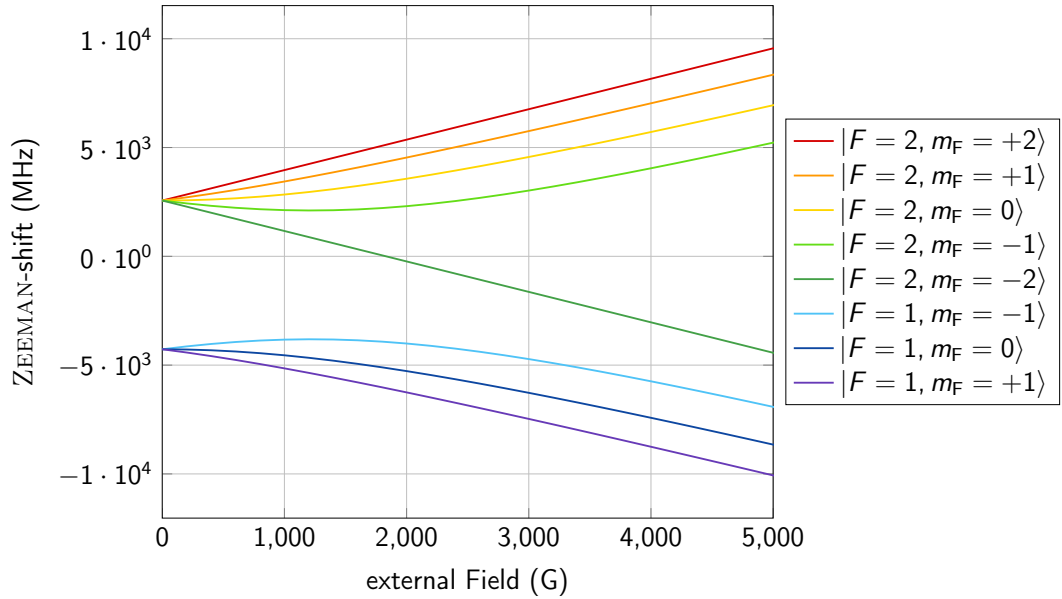


**Figure 2.2.:** ZEEMAN splitting of the  $^{87}\text{Rb}$  ground state  $5^2\text{S}_{1/2}$ . For small fields it can be approximated by the linear function eq. (2.5). At strong magnetic fields the PASCHEN-BACK-effect takes over which stems from higher orders in the initial Hamiltonian eq. (2.4).

applying FOURIER-transformation to the amplitude. The complex amplitude squared yields the intensity distribution, which is a LORENTZIAN-profile. The FWHM of this is defined as the natural linewidth. The energy uncertainty is then

$$\Gamma = \frac{e^2\omega_0^2}{2\pi\epsilon_0 m_e c^3} \frac{2J+1}{2J'+1} f, \quad (2.8)$$

which is also the Einstein coefficient for spontaneous decay or the inverse of a states lifetime. For  $^{87}\text{Rb}$  D line transitions the natural linewidth is  $\delta\nu \approx 6.065$  MHz.

#### 2.1.4. Thermal Linewidth

Since scanning a laser frequency  $\nu_L$  will not only excite the transition with the frequency  $\nu_t$ , but also through their thermal motion by,

$$\nu'_t = \nu_t \left(1 + \frac{v}{c}\right), \quad (2.9)$$

DOPPLER shifted atoms. In kinetic gas theory, for an ideal gas with particle mass  $m$  at a temperature  $T$ , each velocity component is normal distributed and the variance is

given by

$$\sigma = \sqrt{\frac{k_{\text{B}}T}{m}}. \quad (2.10)$$

From this the average velocity distribution of an ideal gas can be derived to

$$p(v) = \left(\frac{m}{2\pi k_{\text{B}}T}\right) 4\pi v^2 e^{-\frac{mv^2}{2k_{\text{B}}T}}, \quad (2.11)$$

which is known as the MAXWELL-BOLTZMANN distribution.

Taking the full width half maximum (FWHM) of eq. (2.11) and inserting it into eq. (2.9) one gets the thermal linewidth,

$$\Delta\nu = \nu_t \sqrt{\frac{8k_{\text{B}}T \ln(2)}{mc^2}}, \quad (2.12)$$

which describes the so called DOPPLER-valleys broadening any transition.

Thermal broadening can be homogeneous, when all transitions are equally broadened or inhomogeneous. In the experiment, it is usually a mixture of both, which explains the normally skewed GAUSS-Distribution shape of DOPPLER-valleys, as seen in fig. 3.3. The  $^{87}\text{Rb}$  D2 line, which is important for this experiment, has a thermal linewidth of  $\Delta\nu = 510$  MHz.

### 2.1.5. Clock State

To obtain a clock state, which is magnetically insensitive, one would normally use  $|m_{\text{F}} = 0\rangle \rightarrow |m'_{\text{F}} = 0\rangle$  transitions. This makes only sense when optically trapping atoms. In our case we need to use states which are sensitive to magnetic fields, to keep them magnetically trapped.

To still generate a clock state with magnetically trapped atoms, we can use the convenient  $^{87}\text{Rb}$  hyper fine structure sublevels, described by eq. (2.6). For a small external field of around  $B_0 \approx 3.23$  G, the two ZEEMAN sublevels  $5^2\text{S}_{1/2} |F = 1, m_{\text{F}} = -1\rangle$  and  $5^2\text{S}_{1/2} |F = 2, m_{\text{F}} = 1\rangle$  experience the same first order ZEEMAN shift, while the second order ZEEMAN shift with approximately is minimized [24]. Therefore, this transition is magnetically insensitive at this small field while  $m_{\text{F}} \neq 0$ . Furthermore, for both states the product  $g_{\text{F}} \cdot m_{\text{F}} > 0$ , which is necessary to be trapped in a magnetic minimum. This clock state has been investigated by [25] and showed a promising very long coherence time. However, the trapping strength would still vary by  $|g_{\text{F}}| = \frac{1}{2} \leftrightarrow \frac{2}{3}$ , introducing a breathing of the cloud.

## 2. Theoretical Background

---

In our experiment we intend to use this clock transition on the chip trap (section 2.3.4) for the strong coupling. To get the exact splitting of the clock state, we have to use the BREIT-RABI formula eq. (2.6) which shows that the clock transition only exists for small fields in the order of few Gauss.

This transition has  $\Delta F = +1$  and  $\Delta m_F = +2$  is according to the selection rule  $\Delta m_F = -1, 0, +1$  forbidden. However, exciting to a virtual level with a MW of 6.384 GHz and further exciting with a small RF signal to the  $m_F = 1$  state, makes it experimentally possible to drive this clock transition as seen in fig. 2.3.

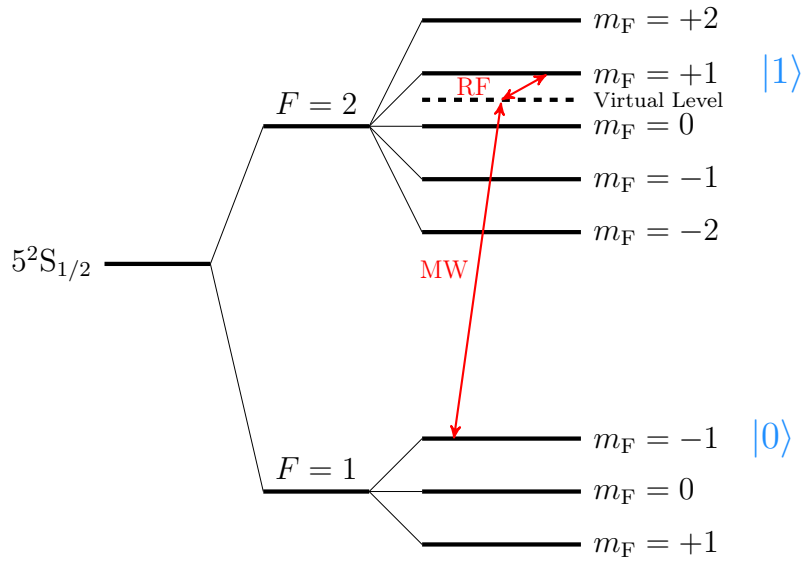


**Figure 2.3.:** Clock state in the  $^{87}\text{Rb}$  ground state manifold.

## 2.2. Cooling of Atoms to ultra cold Temperatures

In order to see quantum effects and conduct quantum optical experiments in a dilute gas, such as condensing it into a BEC, it is necessary to cool down to ultra cold temperatures close to 0 K and get rid of the bulk of the kinetic energy eq. (2.13). To cool atoms to such low temperatures laser light is utilized to exert a force on the atoms. Such a force is caused either by radiation pressure or intensity gradient, where the first is used for laser cooling and the latter causes a dipole force as used e.g. in dipole traps.

Since the first utilization of lasers to cool neutral atoms [26], this technique found countless applications in cold atom experiments and Quantum sensors [27], with constant development and progress [28]. In this experiment, laser cooling is the first

step in the experimental cycle and lays the basis for any proceeding operation. This section gives an overview of the necessary techniques and physical concepts to cool atoms with lasers.

### 2.2.1. DOPPLER-Free Spectroscopy

To frequency stabilize a laser, which is necessary to drive a specific optical electron transition for laser cooling, optical pumping etc., one needs to resolve the hyperfine structure as seen in fig. 2.1. However, as described in section 2.1.4 the thermal energy broadens any transition to the thermal linewidth. For an ideal gas at around  $T = 300$  K, this is according to eq. (2.13) in the range meV,

$$\bar{E} = \frac{3}{2}k_{\text{B}}T \approx 39 \text{ meV}, \quad (2.13)$$

which corresponds to hundreds of MHz. This exceeds by far the energy gaps of the rubidium hyperfine structure. Therefore, it is clear the DOPPLER-effect will be dominant in a spectroscopy at room temperature.

To still be able to resolve the hyperfine states, DOPPLER free spectroscopy (DFS) (also saturation absorption spectroscopy called) is required. In fig. 2.4, a simple optical setup for such a spectroscopy is depicted.

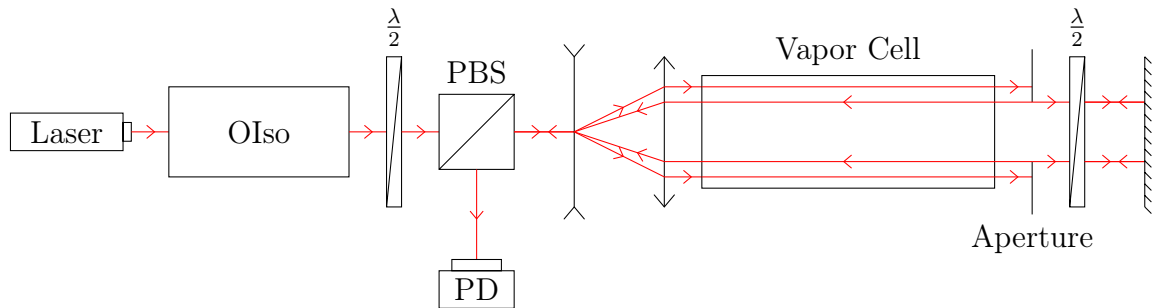


**Figure 2.4.:** Effective optical setup for a DOPPLER free spectroscopy.

In this setup, the optical isolator (OIso) first ensures no light is back reflected into the laser diode, which could destroy it. Next, the first  $\frac{\lambda}{2}$ -plate ensures that most light passes straight through the polarizing beam splitter (PBS) and not directly into the photo diode. Then, the pump beam will excite the atoms at its initial pass through the vapour cell and then reflects back at the mirror, before the actual probe beam passes through the vapour cell. The second  $\frac{\lambda}{2}$ -plate rotates the polarity so that the probe beam is directed into the photo diode (PD) by the PBS. Additionally, the telescope in



front of the vapour cell enlarges the laser beam almost to the diameter of the vapour cell to maximize the spectroscopy signal.

Off resonance, saturated absorption spectroscopy first excites the atoms, which are resonant through DOPPLER shift with the pump beam. The probe beam (back reflection) then excites the atoms which are DOPPLER shifted in the other direction. This leads to two distinct velocity groups of excited atoms, as seen in fig. 2.5 for  $\nu_L$  below fig. 2.5a and above fig. 2.5b  $\nu_t$ . At resonance, the probe beam and pump beam can only excite atoms with a velocity of  $v_z = 0$  in beam direction, as shown in fig. 2.5d. Since, these are considerably less atoms than in the off resonance case the intensity at the PD is higher. Thus leading to a dip in the spectroscopy with theoretically just the width of the natural linewidth (see section 2.1.3).

As described, above the thermal energy of the atoms is magnitudes higher than the transitions. Therefore, normally within one DOPPLER valley several transitions will be situated. Now, if two transitions share a common ground state a, crossover (CO) peak will emerge. As seen in fig. 2.5c, at some point during the scan  $\nu_L$  will be in the middle of  $\nu_{t_1}$  and  $\nu_{t_2}$ . At this frequency, the pump beam can excite  $\nu_{t_1}$  through red shift and  $\nu_{t_2}$  through blue shift at the same time. This, holds vice versa for the probe beam as well. Therefore, possible excitations for the probe beam are already saturated which leads to an increased transmission, note able by an even stronger dip in the spectroscopy [29].

### 2.2.2. Laser Cooling

For neutral atoms, such as Rubidium, laser cooling is done in a magneto optical trap (MOT). Such consist of a quadrupole trap formed by two coils magnetically trapping the atoms with a restoring force and cooling laser beams for a position dependent force. In a 3D MOT as used in this work, lasers from all 6 directions in Cartesian coordinates, as seen in fig. 2.6, are necessary to cool the atoms.

The trapped atoms move with a velocity  $\mathbf{v}$  due to their kinetic Energy around in space. Therefore, the 6 cooling beams with a wave vector  $|\mathbf{k}|$  and frequency  $\nu_L$  are DOPPLER shifted to them. With this, the atoms see an effective laser frequency of

$$\nu_e = \nu_L - |\mathbf{k}| |\mathbf{v}| \cos(\theta) = \nu_L \left(1 - \frac{v}{c} \cos(\theta)\right), \quad (2.14)$$

with  $\theta$  being the incident angle between atom and laser beam.

If the atoms move towards the beam ( $\frac{\pi}{2} < \theta \leq \pi$ ), the laser frequency increases for them, while with  $0 \leq \theta \leq \frac{\pi}{2}$  it shifts down. When the laser is now red detuned by  $\delta$ , atoms moving towards it can become resonant at  $\nu_e = \nu_L - \delta = \nu_0$ . Since they are

## 2. Theoretical Background

---

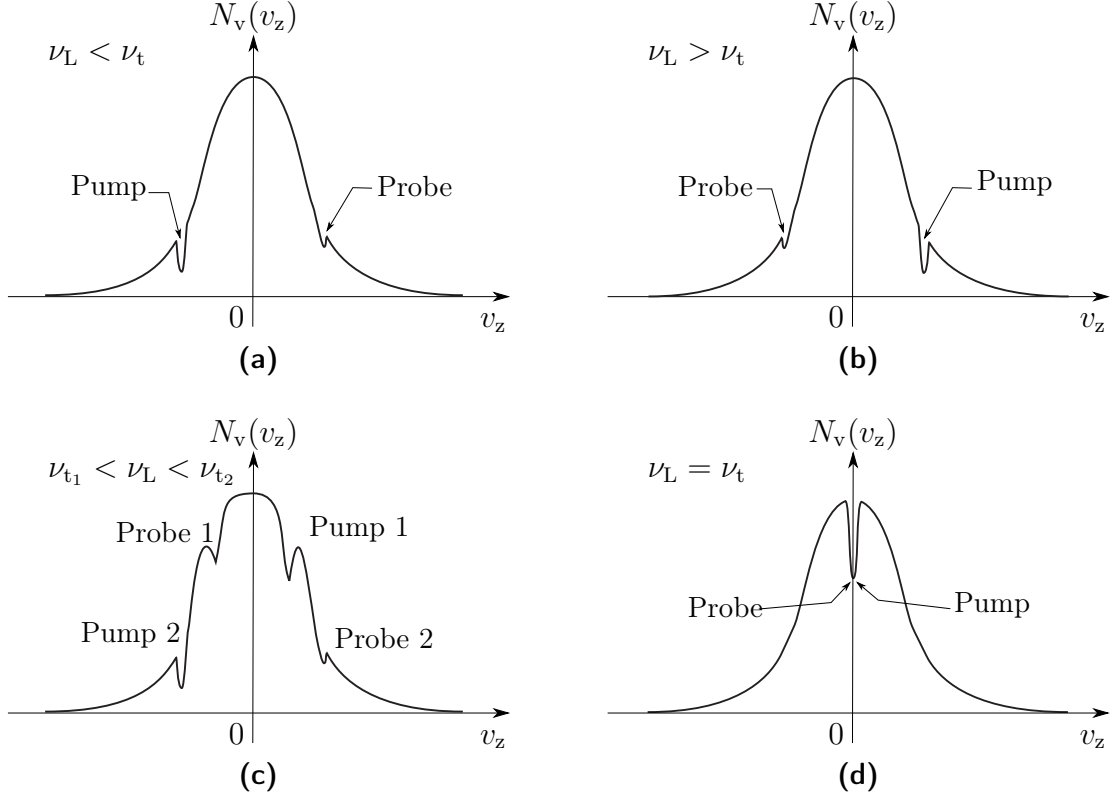


**Figure 2.5.:** Principle of DFS, showing which velocity groups of the velocity distribution  $N_v(v_z)$  of atoms, are excited by the probe and pump beam, for a laser frequency (a) lower or (b) higher than the transition frequency. (c) shows when there are several transitions within one DOPPLER-valley and  $\nu_L$  is between two transitions  $\nu_{t_1}$  and  $\nu_{t_2}$ . In this case, cross over peaks will form. When the spectroscopy hits the transition exactly as in (d), only one dip with the natural linewidth remains.

resonant now they can absorb photons, which gives them a push back. Then, through spontaneous emission, the photon gets emitted in a random direction. Thus, leaving a net momentum in direction of the cooling beam [30]. Since there are cooling beams coming from all 6 directions the atoms experience a damping force

$$\mathbf{F}_{\text{cool}} = \frac{\hbar \mathbf{k} \cdot \Gamma}{2} \frac{\tilde{I}}{1 + \tilde{I} + \frac{4\Delta^2}{\Gamma}}, \quad (2.15)$$

where  $\tilde{I}$  is the by the saturation intensity normed laser intensity and the DOPPLER shifted laser detuning

$$\Delta = \nu_L - \nu_t - \mathbf{k} \cdot \mathbf{v}. \quad (2.16)$$

It follows that the atom is damped as if it would move in a viscous medium. The velocity range which can be captured in this process is determined by the natural

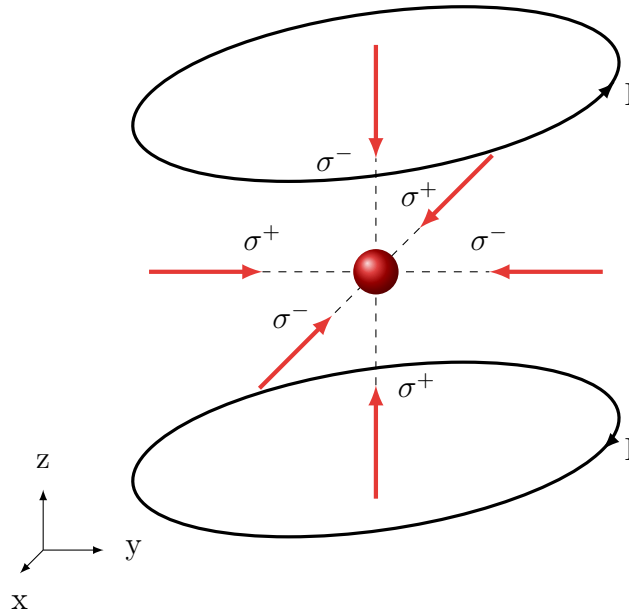


**Figure 2.6.:** Basic MOT scheme.

linewidth  $\Gamma$  of the excited state to

$$\Delta v \sim \frac{\Gamma}{k}, \quad (2.17)$$

where  $k$  is the wave number of the laser beam [31].

After spontaneously emitting a photon, the emitted photon might be absorbed by another atom which is then randomly kicked. In consequence of this and SHOT noise in the cooling light, the atoms also experience a heating, which competes with the damping force. This limits the temperature reachable with laser cooling. For an ideal detuning of  $\delta = \frac{\Gamma}{2}$ , the dampening and heating is in an equilibrium and the DOPPLER-limit is minimized to

$$T_D = \frac{\hbar\Gamma}{2k_B}. \quad (2.18)$$

For  $^{87}\text{Rb}$  with a  $\Gamma \approx 18.05$  MHz  $T_D$  calculates to about  $152 \mu\text{K}$ .

**Magneto Optical Trap** In [32] it is shown, that only through radiation pressure atoms cannot be stably be trapped. Therefore, a restoring force needs to be added to the cooling beams creating. This is done with a magnetic field creating a magneto optical trap. The magnetic field is a quadrupole field created by the AH coil pair seen in fig. 2.6. Equation (2.21) shows, that neutral atoms experience a potential in an external magnetic field, due to the ZEEMAN shift. As shown in section 2.3.1 with

a positive product  $g_F \cdot m_F$  the atoms seek a magnetic minimum. Thus, creating a constant force pushing into the center of the MOT.

To keep atoms tightly trapped, it is necessary to maximise  $m_F$  in the  $|F = 2\rangle$  state. Through the  $\sigma^-$  polarized light in the positive directions atoms will get lost to  $m_F < 0$  states. Furthermore, through spontaneous emission atoms can also decay into the  $|F = 1\rangle$  state in the ground state. A dedicated repumper laser, as described in section 3.1.3, brings them back up to the  $|F = 2\rangle$  state.

### 2.2.3. Sub-DOPPLER-Cooling

To beat the above mentioned DOPPLER-limit, we can use another cooling mechanism. Two  $\sigma^+$  and  $\sigma^-$  polarized cooling beams aligned to counter propagate, as shown in fig. 2.6, create a polarization gradient, which exerts a radiation pressure onto the atoms. In contrast a linear  $\perp$  linear polarization gradient setup leads to the so called SISYPHUS cooling effect.

To look at polarization gradient cooling closer, we can simplify our 3D MOT into 3 orthogonal 1D systems. Here, the two counter propagating beams create a rotating linear polarization, through the superposition of the  $\sigma^+$  and  $\sigma^-$  polarized beams. Atoms at rest in such a light field would mainly occupy  $m_F = 0$  sub-states. For a moving atom, the quantization axis will then be rotated by  $2\pi$  every wavelength  $\lambda$  of the cooling beam. In [31] it is shown, that the polarization gradient produces a population imbalance if we address a state with  $F \geq 1$ . This population( $\Pi$ ) imbalance is created by the STARK shift experienced by the effective linear polarization and is proportional to the velocity by,

$$\Pi_{m_F+1} - \Pi_{m_F-1} \sim -vk. \quad (2.19)$$

Therefore, atoms moving in positive x, y or z direction against the  $\sigma^+$  cooling beam will preferentially occupy the  $m_F = +1$  state. In this state they scatter  $\sigma^+$  light much more efficiently due to the different CLEBSCH-GORDON coefficients. This preferential scattering of the opposing laser beam leads to a radiation pressure. This anisotropic pressure effectively cools analogue to the one in section 2.2.2, but this time not relying on the DOPPLER effect. Therefore, it is not bound by the DOPPLER-limit and maximal for a detuning of  $-\sqrt{\frac{5}{4}}\Gamma$ . This limits the cooling to the recoil temperature

$$T_R = \frac{\hbar^2 k^2}{2k_B m}, \quad (2.20)$$

governed by the energy change through a scattered photon, where  $m$  denotes the atomic

mass of our species. For  $^{87}\text{Rb}$ , this would be around 350 nK. In practise, temperatures as low as 2  $\mu\text{K}$  can be reached.

## 2.3. Magnetic Trapping

To trap and transport neutral atoms in this experiment, magnetic fields are used. Another option to trap and transport neutral atoms is with far detuned laser light, so called optical dipole traps. First, the basic principle is explained and then different methods used in this setup to create magnetic minima are discussed.

### 2.3.1. Neutral Atoms in Magnetic Fields

Unless ions, neutral atoms feel a electromagnetic force, since they are as the name implies neutral. However as described in section 2.1.2, their hyperfine states split when an external Magnetic field is applied. The energetic splitting in first order,

$$\Delta E = g_{\text{F}} m_{\text{F}} \mu_{\text{B}} B_z. \quad (2.21)$$

Therefore, atoms seek depending on the product  $m_{\text{F}} \cdot g_{\text{F}}$  a magnetic minimum for positive ones and maximum, for negative products. Since, a magnetic maximum, due to [33], is not possible to create in a static magnetic field, atoms must be prepared into a state with a positive product of  $m_{\text{F}} \cdot g_{\text{F}}$ . This reduction in energy through occupying a low field seeking state keeps pushing the atoms towards a magnetic minimum.

In the  $^{87}\text{Rb}$  ground sate manifold,  $|F = 2, m_{\text{F}} = 2\rangle$  is the strongest low field seeker. In the other hyperfine level of the ground state,  $|F = 1, m_{\text{F}} = -1\rangle$  is the strongest trapped state, due to the different sign of  $g_{\text{F}}$ . To ensure strong trapping during the transport and the rest of the experimental cycle after laser cooling an optical pump pulse is applied to put all atoms into the  $m_{\text{F}} \cdot g_{\text{F}}$  state.

Due to gravity acting upon the atoms any magnetic trap is effectively modified by an additional vertical magnetic field gradient,

$$\frac{\partial B}{\partial z} = \frac{m \cdot g}{m_{\text{F}} g_{\text{F}} \mu_{\text{B}}}, \quad (2.22)$$

where  $m$  is the atom's mass and  $g$  the gravitational acceleration. For  $\text{Rb}^{87}$  in the ground state with  $|F = 2, m_{\text{F}} = 2\rangle$ , this calculates to a gradient of 15.57  $\text{G cm}^{-1}$ .

### 2.3.2. Quadrupole Trap

According to the BIOT-SAVART law the magnetic field along the symmetry axis for a coil is given by

$$B(z) = \frac{\mu_0 N I}{2} \cdot \frac{R^2}{\left(R^2 + \left(z + \frac{a}{2}\right)^2\right)^{\frac{3}{2}}}. \quad (2.23)$$

Here,  $N$  is the number of windings, while  $R$  is the radius of the coils. From this, the magnetic field for the setup described in fig. 2.6, along the symmetry axis  $z$  with two currents  $I$  flowing in opposite direction is deduced to

$$B(z) = \frac{\mu_0 N I R^2}{2} \left( \frac{1}{\left(R^2 + \left(z + \frac{a}{2}\right)^2\right)^{\frac{3}{2}}} - \frac{1}{\left(R^2 + \left(z - \frac{a}{2}\right)^2\right)^{\frac{3}{2}}} \right). \quad (2.24)$$

Where,  $a$  denotes the distance between the coils. When  $a = R$  the gradient at  $x = 0$  is maximal, while the second and third derivatives vanish. This corresponds to a spherical linear field equal zero at this point as seen in fig. 2.7b. This specific configuration is then called anti-HELMHOLTZ (AH) configuration.

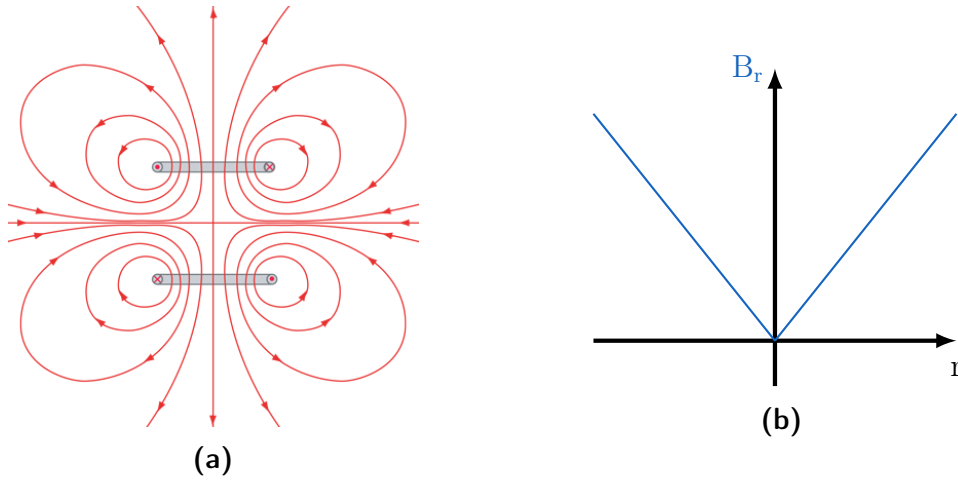


**Figure 2.7.:** (a) Schematic vector plot of magnetic Quadrupole field of a coil pair in AH configuration. The current loops are the grey bars with opposite currents flowing indicated. In this configuration,  $|\mathbf{B}| = 0$  and therefore  $\frac{\partial B_r}{\partial r} = \text{constant}$  close to the center. (b) shows the linear behaviour of the magnetic field, around the center of an AH configuration coil pair, in radial direction.

### 2.3.3. IOFFE-PRITCHARD Trap

A coil pair in AH configuration creating a quadrupole trap has a field of zero at its centre. As described in section 2.3.5, this causes spin flips close to the zero point, which let then atoms escape. During the MOT phase and transport, this is not so crucial since the atoms are relatively warm with several hundred  $\mu\text{K}$ . However, before loading onto the chip, they need to be cooled and loaded into a elongated trap. Once they are evaporative cooled, the MAJORANA-losses would be too strong. Therefore, they need to be loaded into another type of trap [34]. An IOFFE-PRITCHARD trap or also quadrupole-IOFFE-configuration (quIc) called trap, as mainly referred here is ideal. It is created by simply adding an inhomogeneous field through a perpendicular to the AH coil situated coil. This additional field transforms through superposition of the magnetic fields a quadrupole trap with a linear potential fig. 2.7b into a harmonic trapping potential. The transversal direction is tightly trapped, whereas in longitudinal direction the atoms are only loosely bound. This lets the trap resemble a cigar in shape. The important property of such a trap is that it has a non zero magnetic minimum at the center. Thus, the atoms experience a ZEEMAN splitting in the entire trap and MAJORANA-losses are significantly reduced. This property of a quIc trap is important to create a BOSE-EINSTEIN-condensate as described in [35].

### 2.3.4. Magnetic Trapping with Wires and Atomchips

To get even tighter traps, i.e. higher trapping frequencies than in a quIc trap, one needs to switch to a wire in combination with a bias field. This can be done with simple wires in free space [36]. Improving this can be done by utilizing the well established industry for lithography in semiconductor industries. This allows to fabricate such wires on some substrate. These so called atomchips are a versatile experimental platform, which can bare various nano-fabricated structures and therefore allow for countless types of experiments [6, 37, 38].

The magnetic field of such a wire or printed circuit board track on an atomchip is described by BIOT-SAVART's law. Since the atomic cloud is normally far away compared to the wire width ( $w \ll d$ , where  $d$  is the distance to the chip) and the cloud is small compared to the central part of the chip wire. We can approximate the magnetic field of it by an indefinitely thin and long wire to

$$B(r) = \frac{\mu_0 I}{2\pi r}. \quad (2.25)$$

Applying a bias field, as shown in fig. 2.8, counter propagating the wire field on top of the chip creates a magnetic minimum where the x-component and the bias field

## 2. Theoretical Background

---

$\mathbf{B}_{\text{bias}}$  cancel each other. Due to the bend leads to the central part of the wire, the magnetic minimum is non-zero, like in a qulc trap, which is important to prevent MAJORANA-losses. The resulting magnetic field creates a tight harmonic potential

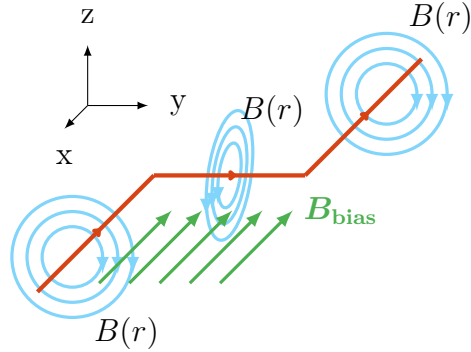


**Figure 2.8.:** Trapping atoms with wires.

into transverse direction and a shallow one in longitudinal direction. Thus, effectively giving a quasi 1D system analogue to section 2.3.3.

Through the good control of the atoms and quasi 1D trap, atomchips have lead to many discoveries in the last years [39–42].

### 2.3.5. Loss Mechanisms

While magnetically trapped, neutral atoms can still leave the trap through various loss channels, leading to a finite lifetime of trapped atoms.

#### MAJORANA-losses

After laser cooling, trapped atoms still have a residual velocity. This lets them experience an ever-changing magnetic field in the atom frame. This rate of change of the magnetic field  $\frac{v}{B}$  has to be slower than the LARMOR frequency  $\omega_L = \frac{m_F g_F \mu_B B}{\hbar}$ , otherwise the spin can flip to untrapped or anti-trapped states. An estimate for the loss rate is done in [34], yielding

$$\Gamma_{\text{Majorana}} \propto \frac{\hbar}{ml^2}, \quad (2.26)$$

where  $l$  is the radial half width half maximum cloud size in a quadruple trap. For  $^{87}\text{Rb}$  with a mass of  $m = 87 \text{ u}$  and cloud sizes of about 1 mm, loss rates of  $\Gamma \sim 1 \times 10^{-3} \text{ s}^{-1}$  are typical in quadrupole traps. Through the quadratic dependence of the inverse



cloud size, it is clear, that this loss channel is dominant for very cold and dense clouds and therefore, small traps with a zero trap bottom. However, with a small offset field like 10 mG, this can be significantly reduced, since an constant quantization axis is then present (see section 2.3.3).

### Background gas collisions

Any collisions with the rest gas in the UHV environment also trigger losses. Since, the rest gas has not been cooled, their kinetic Energy is very high in comparison to that of the ultra cold  $^{87}\text{Rb}$  atoms. Therefore, this elastic scattering transfers enough momentum, to kick atoms out of the trap. The loss rate is given by

$$\Gamma_{\text{background}} \propto \sum_i n_i \langle \sigma_i \cdot v_i \rangle, \quad (2.27)$$

where  $i$  is the sum over all relevant gas species,  $\sigma_i$  denotes the loss cross section of the molecules or atoms with the velocity  $v_i$ . The brackets symbolise an average over the thermal BOLTZMANN distribution and  $n_i$  are the particle densities. The velocities of the  $^{87}\text{Rb}$  atoms are neglected, which is a valid assumption for a laser cooled gas. Typical loss rates for thermal background gas with a pressure of  $10^{-9}$  mbar and laser cooled  $^{87}\text{Rb}$  is around  $\Gamma_{\text{background}} \approx 0.05 \text{ s}^{-1}$  [43].

### Collision losses

Between the trapped atoms collisions occur as well. While two body collisions can only be elastic in an  $|F = 2, m_F = 2\rangle$  spin polarized gas due to the selections rules, three body collisions can be inelastic. In such collisions the third atom takes away the binding energy necessary to form  $\text{Rb}_2$  molecules. The loss rate

$$\Gamma_{3 \text{ body}} = Ln^3, \quad (2.28)$$

is proportional to the ensemble density  $n$  cubed, since three bodies are involved, while is  $L$  the three body loss rate coefficient.  $^{87}\text{Rb}$  has a  $L \approx 4 \times 10^{-30} \text{ cm}^6 \text{ s}^{-1}$  [44]. This loss channel is only relevant at very low temperature and at high densities, when the atoms lost as molecules carry less kinetic energy as the atom staying in the trap, thus heating up the cloud [45]. For BECs this is the dominant loss mechanism.

### Noise Losses

In an atomchip or coils current noise is can cause, depending on the frequency, also losses. At low frequencies in the range of the trapping frequency current fluctuation heat the atoms, while higher frequencies  $> 100$  kHz induce spin flips to untrapped states. Such noise is either produced by fundamental physics or through technical imperfections, which can be reduced by filtering.

Fundamental current noise originates from the discrete value of the electron charge and its thermal agitation, which makes it difficult to mitigate it. The first named SHOT noise, is only relevant for very small currents, whereas the latter, called JOHNSON-NYQUIST noise, stems from thermal fluctuations. It is therefore, for Superconductors and very low temperatures, negligible [46]. The thermal motion of the electrons cause magnetic field fluctuations, which can also induce spin flips. With FERMI's golden rule, the spin flip rate is calculated in [47] to

$$\Gamma_{\text{Johnson Nyquist}} = \left(\frac{8}{3}\right)^3 \frac{\tau_0}{\bar{n}_{\text{th}} + 1} \left(\frac{\omega_L}{c}\right)^3 \frac{d^4}{3\delta_L}, \quad (2.29)$$

where  $\bar{n}_{\text{th}}$  is the average thermal occupation, which is at low temperatures well approximated by  $\bar{n}_{\text{th}} = \frac{k_{\text{B}}T}{\hbar\omega_L}$  and  $\tau_0$  is the life time in free space. Equation (2.29) is only valid in this form, when the skin depth at the LARMOR frequency,

$$\delta_L = \sqrt{\frac{2}{\omega_L \mu_0 \sigma(T)}}, \quad (2.30)$$

is much smaller than the atom to chip distance  $d$  and the conductor width. However this noise form is extremely reduced in this setup, due to the superconducting atoms chip and coils, leading to significantly increased lifetimes [48, 49].

### 3. Experimental Setup

In this chapter, a general overview of the setup is given. Thorough description of most parts is given already in [50]. Some specific, in the course of this thesis added, parts of the setup are also described in greater detail, since they are not mentioned in the other theses on the QuIc experiment.

The entire experiment is situated on and around an optical table<sup>1</sup> from Thorlabs. The table houses all the Vacuum systems, the magnetic conveyor belt and our 4 lasers with all their optics. While the Cryostat is suspended from the ceiling to mechanically decouple it, all power supplies batteries RF sources etc. are under or above the table. An overview of the core, vacuum related parts can be seen in fig. 3.1.

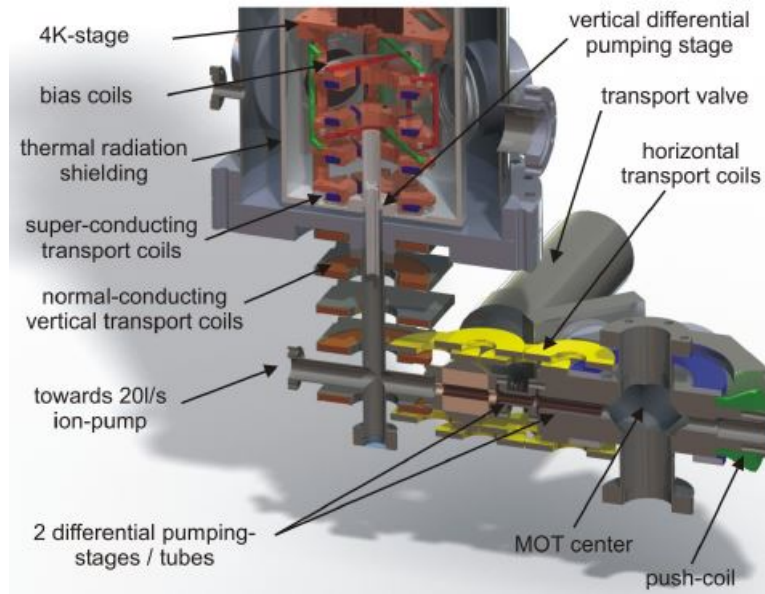


Figure 3.1.: Overview of the experiment.

<sup>1</sup>PTR52510 - Ultra Plus Series Optical Table - 3000 mmx1250 mmx310 mm

## 3.1. Laser Setup

In order to cool, manipulate and image our  $^{87}\text{Rb}$  atoms, different lasers are required for the D2 line. Furthermore, the setup comprises a powerful laser to conveniently quench superconducting structures on the atomchip. First, the different laser types and locking schemes used are reviewed, then our lasers and their functions are explained.

### 3.1.1. Laser Configurations

The most common type of laser are semiconductor lasers, which is basically a diode (i.e. P-N junction) wedged between two other semiconductors with a higher band gap. This is called hetero junction. It is more efficient than a simple diode since charge carriers are trapped between the outer layers and emitted photons can't be absorbed in the outer layers, due to the higher band gap. They are cheap, easy to handle and available in a huge range of frequencies. Usually, these laser diodes don't have a particular good linewidth and output power per se. In general, the linewidth of a laser is fundamentally limited through quantum mechanical effects such as spontaneous emission and the uncertainty principle as well optical noise. This is expressed in the SCHAWLOW-TOWNES formula,

$$\Delta\nu = \frac{2\pi h\nu \Delta\nu_{\text{res}}^2}{P_{\text{laser}}}, \quad (3.1)$$

where  $P_{\text{laser}}$  is the power output of the laser,  $\nu_{\text{res}}$  the linewidth of the lasers optical resonator and  $\nu$  the laser frequency [51]. The minimal band width of a resonator can then, according to [52], be written as

$$\Delta\nu_{\text{res}} = \frac{c}{2L}. \quad (3.2)$$

With the light speed  $c$  and the resonator length of typical  $L \approx 300 \mu\text{m}$ , we get a minimal resonator band with of approximately 500 GHz. Plugging this number back into eq. (3.1) for our 780 nm and typical laser power of around 20 mW, ultimately, we get a line with of

$$\Delta\nu_{^{87}\text{Rb}_{\text{D2}}} \approx 20 \text{ MHz}. \quad (3.3)$$

This exceeds the natural linewidth  $\Gamma_{^{87}\text{Rb}} \approx 6.1 \text{ MHz}$  so the linewidth has to be enhanced, while the power has to be amplified as well.

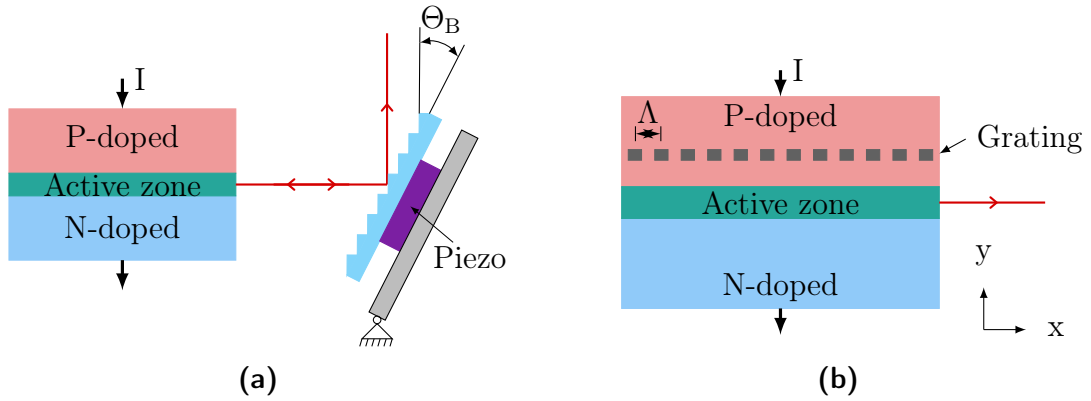


**Figure 3.2.:** Used semiconductor laser types: (a) shows a laser diode with an external cavity with a blazed grating in LITTROW configuration. The external cavity length is tune able by piezo. (b) is a sketch of a laser diode with distributed feedback through the grating structure in the semiconductor.

### External Cavity Diode Laser

A simple semiconductor diode laser as mentioned earlier, unfortunately, has a too broad linewidth to effectively use it in cold atom experiments. However, the linewidth can be improved. External cavity diode lasers (ECDL) add an blazed grating outside the diode, mounted pivot able on a piezo, as seen in fig. 3.2a. The grating equation, from [53], is given by

$$d(\sin \alpha \sin \beta) = m\lambda, \quad (3.4)$$

with incident angle  $\alpha$ , refracting angle  $\beta$ , grating constant  $d$  and diffraction order  $m$ . This simplifies with  $\alpha = \beta = \theta_B$ , the so called LITTROW configuration, to BRAGG's law eq. (3.5).

$$2d \sin \theta_B = m\lambda \quad (3.5)$$

In this configuration, the  $m = 0$  order is coupled out and used in the experiment, while the majority of light with  $m = 1$  gets back reflected into the laser diode to enhance the feedback. This forces the laser to run at this wavelength. Through the piezo the blazed grating is parallel shifted and therefore adapts the external cavity, thus the wavelength. This way the linewidth is reduced well below a MHz to about 339 kHz, while the wavelength can be tuned over several GHz by the Piezo.

### Distributed Feedback Laser

A more compact method to reduce the linewidth of a laser diode is to insert a periodic structure, acting as a diffraction grating as seen in fig. 3.2b. In a Distributed feedback

(DFB) laser, this built in grating provides wavelength selective feedback over the entire resonator. The grating can either be made by a spatial variation of the refracting index  $n$  by an amplitude  $n'$  (eq. (3.6)) or the gain  $g$  by an amplitude  $g'$  (eq. (3.7)) in the gain medium,

$$n(x) = \bar{n} + n' \cos\left(\frac{2\pi x}{\Lambda}\right), \quad (3.6)$$

$$n(x) = \bar{g} + g' \cos\left(\frac{2\pi x}{\Lambda}\right). \quad (3.7)$$

Here, the  $\bar{n}$  and  $\bar{g}$  denote the averaged values of the medium. The dimension of the grating  $\Lambda$  is in the order of the desired wavelength and given by the BRAGG condition eq. (3.8).

$$\Lambda = \frac{\lambda_0}{2n} \quad (3.8)$$

As described in [54, 55], this reduces a diodes linewidth to typically a few MHz. Which lets them perform much better than a plain laser diode, but worse than ECDLs.

#### Tapered Amplifier

To efficiently laser cool, a power of several hundred mW is required for the initial laser. The two laser types mentioned above are typically far from such powers with tens of mW. To coherently amplify our DFB or ECDL lasers, a tapered amplifier (TA) can be used. A TA is basically a laser diode with an triangular shaped gain medium, which has on the input facet a width of only a few  $\mu\text{m}$  and widens to a few hundred  $\mu\text{m}$  at the output facet. The seeding laser with a typical power of 10-50mW is coupled to the narrow part, which is comparable to a single mode fiber, acting as a spatial mode filter and then amplified in the widening section to up to several W.

#### 3.1.2. Locking Schemes for our Lasers

As described in section 2.2.1, it is necessary to frequency stabilize our lasers. To achieve this, the laser needs to be temperature stabilized. Here, this is done by PELTIER-elements controlled by an NTC thermistor, close to the laser diode, hooked to a PID regulator. With a good lab environment temperature stabilization of  $\approx 0.1\text{ K}$  and sufficient insulation of the laser box a temperature stability of around 1 mK can be achieved [56]. The temperature is naturally reacting relatively slow and has, through the thermal expansion of the active medium, a huge influence on the laser frequency. Therefore, it is only suited for coarse tuning the wavelength in the range of nm. Just like the temperature also the diode current needs to be controlled by a PID regulator.

### 3. Experimental Setup

The piezo high voltage changing the grating angle in ECDLs as well needs to be regulated. The diode current and grating angle by the piezo in ECDLs are either frequency modulated (FM) locked or frequency offset (FO) locked.

FM locks are modulating the laser frequency with a small frequency to produce an error signal with an APD. This APD measures the DOPPLER free absorption spectroscopy by laser light passing through a rubidium glass cell. Through this modulation, side bands with a frequency  $\omega_T \pm \omega_M$  emerge. When the modulation frequency  $\omega_M$  is big enough, only the first order side bands contribute to the optical field. In our case, we would use  $\omega_M = 21$  MHz (see also [57]). This type of spectroscopy is called DOPPLER free frequency modulation spectroscopy, which is very similar to the one described in section 2.2.1. It resolves the hyperfine structure of  $^{87}\text{Rb}$ , as seen in fig. 2.1. In this the so called crossover peaks are dominant and therefore used for locking on the through the side bands produced error signal.

FO locks use a FM locked master laser which is superimposed with the slave laser. This beam passes through a rubidium glass cell and the DOPPLER free absorption spectrum and is detected as well by an APD. It is then mixed with the signal from a VCO. This mixed signal then gets split into a delayed line and un-delayed line, where the delayed line is just a long BNC cable. By detecting the phase of these two lines, an error signal depending on the VCO frequency is generated, effectively creating a lock, which can be detuned from the master laser by the VCO voltage (see also [58]).

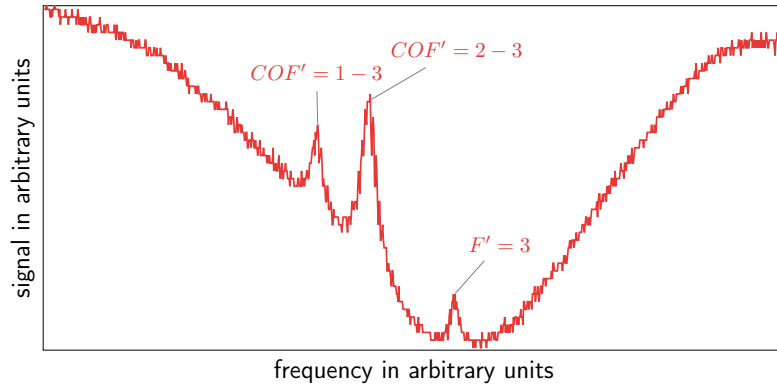


**Figure 3.3.:**  $^{87}\text{Rb}$  D2  $F = 2 \rightarrow F' = 1, 2, 3$  line. The dominant peaks are the two visible cross over peaks  $COF' = 1 - 3$ ,  $COF' = 2 - 3$  and  $F' = 3$ . The other transitions  $F' = 1$ ,  $F' = 2$  and the cross over  $COF' = 1 - 2$  are not visible. The signal of the spectroscopy is for various reasons not good enough to resolve these much smaller peaks. However, the crossover  $COF = 1 - 3$  which is used to lock the master laser is well discernible. Therefore, the locks as described above provide a stable error signal.

### 3.1.3. Laser Units

There are 4 lasers on the optical table and two further lasers in the adjacent lab, intended as backup. The idea is that in case of an unstable or failing laser, it could be easily and fast replaced, by fibering the backup lasers to our optical table. The main lasers are listed below.

- **Master laser:** A ECDL with the code name "Pierre-Luigi", an estimated linewidth of a few hundred kHz and a power of  $\approx 10$  mW. This laser is FM locked to the cross over transition  $F = 2 \rightarrow COF' = 1 - 3$  (see fig. 3.4), since this crossover has a large error signal slope and is therefore quite stable, which is the most important property for the master laser, the TA100 is referenced to it.
- **TA100<sup>1</sup>** laser with a 1 W tapered amplifier chip, whose seeding ECDL is FO locked to the master laser. This setup provides a low bandwidth, high power laser, which is tunable over a range of approximately 100 MHz, which is necessary to set the detunings needed for cooling, imaging and pumping the atoms to the  $|F = 2, m_F = 2\rangle$  state, as indicated by the pink arrows in fig. 3.4. The TA is typically operated with a diode current of about 1750 – 1900mA at a temperature around 18.5 °C, yielding an effective output power of approximately 650 mW.
- **Re-pumper laser:** This is a DFB laser with a power of 14 mW, locked to the  $F = 1 \rightarrow COF' = 1 - 2$  transition (see fig. 3.4) with a FM lock. It has the single use to re-pump atoms during the cooling process, by bringing them back to the  $F = 2$  manifold. It operates with a current of mA at approximately 20 mW
- **Backup lasers:** A FM locked ECDL and DFB laser, which could be used as backup if one of the above lasers fails or for alternative pumping schemes and imaging. Furthermore, since these lasers are operated in a separate room, where hardly anyone enters and their were built with empathize on stability [57], they are by far more stable then the currently used ones.
- **Quench laser:** This laser operating at 1064 nm with up to  $\approx 1$  W, is solely used for quenching parts of the superconducting film on the atomchip. The actual wavelength and linewidth does not matter for this application, but a relatively high power is required. Though the wavelength should be far detuned form relevant  $^{87}\text{Rb}$  transitions, to not disturb the atomic cloud. Therefore, a Mephisto<sup>2</sup> laser was implemented due to its readily availability and sufficient power.

---

<sup>1</sup>Toptica TA100, <https://www.toptica.com/>

<sup>2</sup>Coherent, <https://www.coherent.com/>



### 3. Experimental Setup

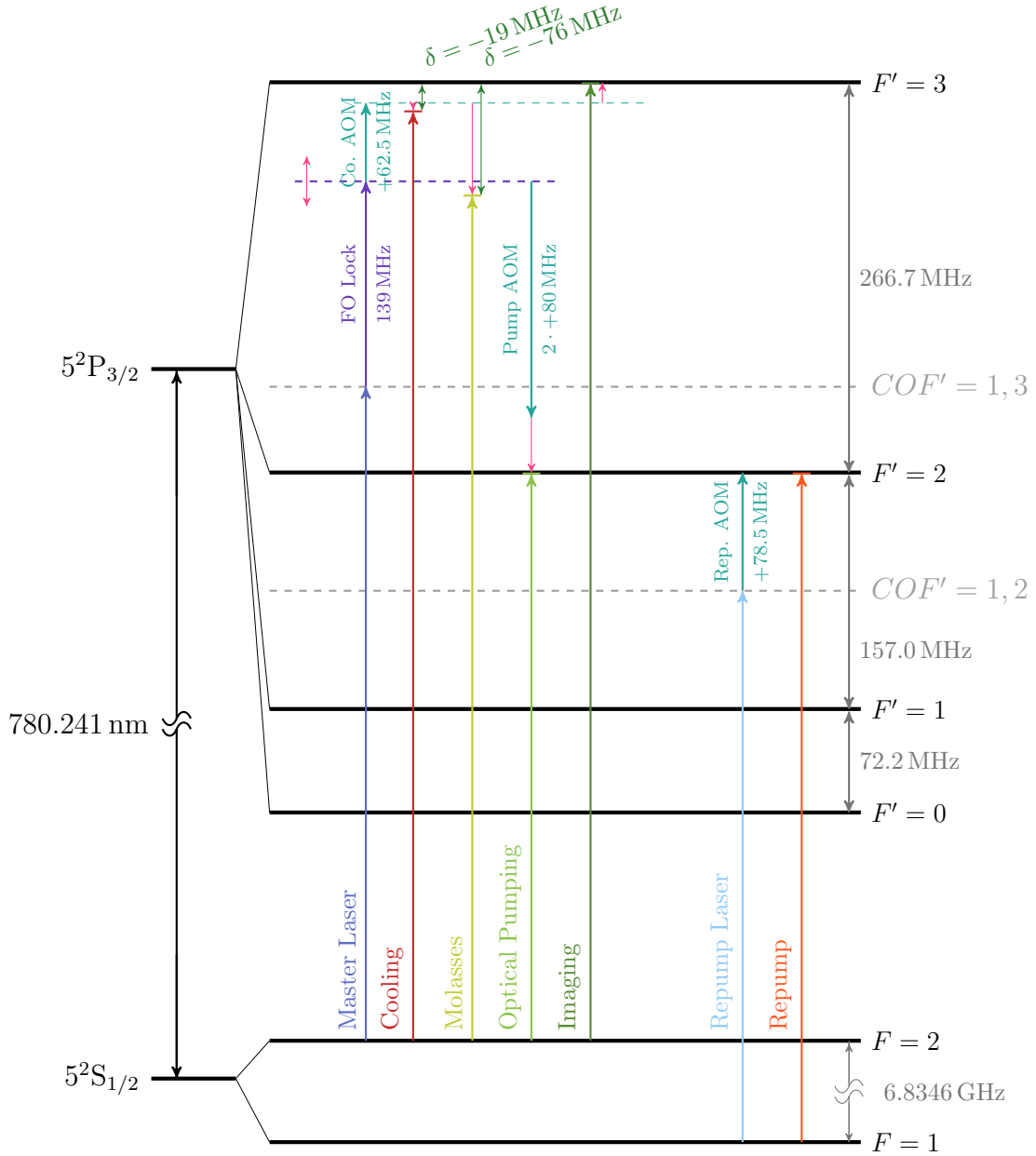


**Figure 3.4.:** Laser transitions used in the experiment on the  $^{87}\text{Rb}$  D2-line. The master laser is locked to the  $F = 1 - 3$  crossover peak. The TA seeding laser gets FO locked to it and thereby, shifted by 139 MHz. After being amplified by the tapered amplifier, it leaves the laser box. The cooling beam going into the MOT-chamber is shifted by an AOM +62.5 MHz. By changing the voltage of the VCO in the FO lock, the main beam frequency gets shifted. This way all the necessary shifts, indicated by thin pink arrows can be reached. The repumper laser is locked to the  $F = 1 - 2$  crossover peak and then shifted with an AOM by +78.5 MHz to the  $F = 1 \rightarrow F' = 2$  transition.

## 3.2. Optical setup

The optical setup in this experiment consists of the laser units as described above in section 3.1.3, optics to laser cool, a quench setup and an imaging system. Since most of the setup is pretty standard and already well described in [2, 59], only the new imaging setup will be explained in detail in section 3.2.1.

Starting from the stabilized main and repumper laser coming out of a wooden box to protect these units from environmental influences, their frequencies get shifted by AOMs and the FO lock, as seen in fig. 3.4. According to theory, to laser cool a detuning of  $\frac{\Gamma}{2}$  would be needed. With a natural linewidth of  $\Gamma = 36.1$  MHz for  $^{87}\text{Rb}$  [20], a detuning of  $\delta = 18.05$  MHz is necessary. Empirically, we found a detuning of  $\delta = -19$  MHz most suitable. Analogously, for the molasses phase we found a optimal detuning of  $\delta = -76$  MHz which is close to the theoretical value of  $-2\Gamma = 72.2$  MHz. For Imaging we found, empirically a detuning of  $\delta = -3$  MHz, where in theory it should be 21.9 MHz to reach the  $F' = 3$  transition.

The main laser is separated into 3 beams. The strongest beam, with up to 190 mW after splitting in all the required paths, is the cooling beam. It is mixed and parallel aligned with the repumper beam, before it is widened to approximately 4 cm in a telescope. This telescope serves also as a fixed and reproduce able point in the whole alignment, since it is built in a cage system, where alignment T-shirts can be inserted, to check the alignment. After the telescope, the beam is split 5 more times to equal intensities. Before they are aligned to overlapped in the center of the MOT chamber, they are polarized to  $\sigma^+$  or  $\sigma^-$  with  $\frac{\lambda}{4}$ - plates, to form the MOT in connection with the MOT coils as described in fig. 2.6.

The other two beams originally stemming from the main beam are for imaging and optical pumping. The optical pump beam is shifted by a double pass AOM down by 160 MHz and then the remaining 70 MHz by the FO lock to reach the  $F' = 2$  transition. Which is needed for a short pump pulse to bring the majority of atoms in to the  $^5S_{1/2} |F = 2, m_F = 2\rangle$  state, for maximal magnetic trapping. Last the imaging beam is divide into 3 beams and fibered to the 3 imaging axes.

The Quench setup is separated from the other optics in this experiment. This setup is rather simple, since there is no need to frequency stabilize it because is just used to locally break the COOPER pairs in the superconducting film on the atomchip. It consists of a laser unit<sup>1</sup>, an automated shutter, a lens to focus the laser and 4 mirrors guiding the beam to the atomchip via a window at the bottom of the vertical transport tube. Furthermore, a PBS can be flipped into the path to guide, from the chip back

---

<sup>1</sup>Innolight Mephisto 1000 NE,  $\lambda = 1064$  nm

reflected light, in a small CCD camera for aligning. This helps to guide the quench beam through the long pipe of approximately 14 cm and the vertical SC transport coils. An approximately 2 ms laser pulse with an intensity of around 900 mW is sufficient to break the superconductivity in the main part of the Z-wire. A more detailed description of this setup can be found in [59].

#### 3.2.1. Imaging Setup

To benchmark the MOT phase, a Pixelfly camera is set up to image the MOT and measure the atom count, temperature and lifetime.

For the actual experiment, there are two cameras installed in front of the cryostat, to image in x (traversal, main imaging) and y (longitudinal, IOFFE) direction. The imaging beam for those is fiber coupled from the ground level of the optical table to the elevated platform around the science chamber. They usually have a power of a few mW. Since, it was an unstable construction and needed constant re-alignment, when switching between different modes, the system was entirely redesigned.

To measure the distance of the atoms to the atomchip, the imaging beam has to hit the chip in an oblique angle, as described in [60]. An optical setup to change the incident angle in the main imaging direction, as seen in fig. 3.5, was devised, to do this more efficiently. Before, it was quite tedious to switch between normal and reflecting imaging, since the fiber out-coupler had to be completely realigned and the camera readjusted. With the new setup, it is simply a matter of removing a mirror on a magnetic mount to switch. This is possible by directly aligning the fiber out-coupler to reflective mode and inserting a mirror to reflect up to a mirror above the out-coupler as seen in fig. 3.5. This last mirror can be aligned to hit the atom cloud horizontally and not reflect on the atomchip.

### 3. Experimental Setup

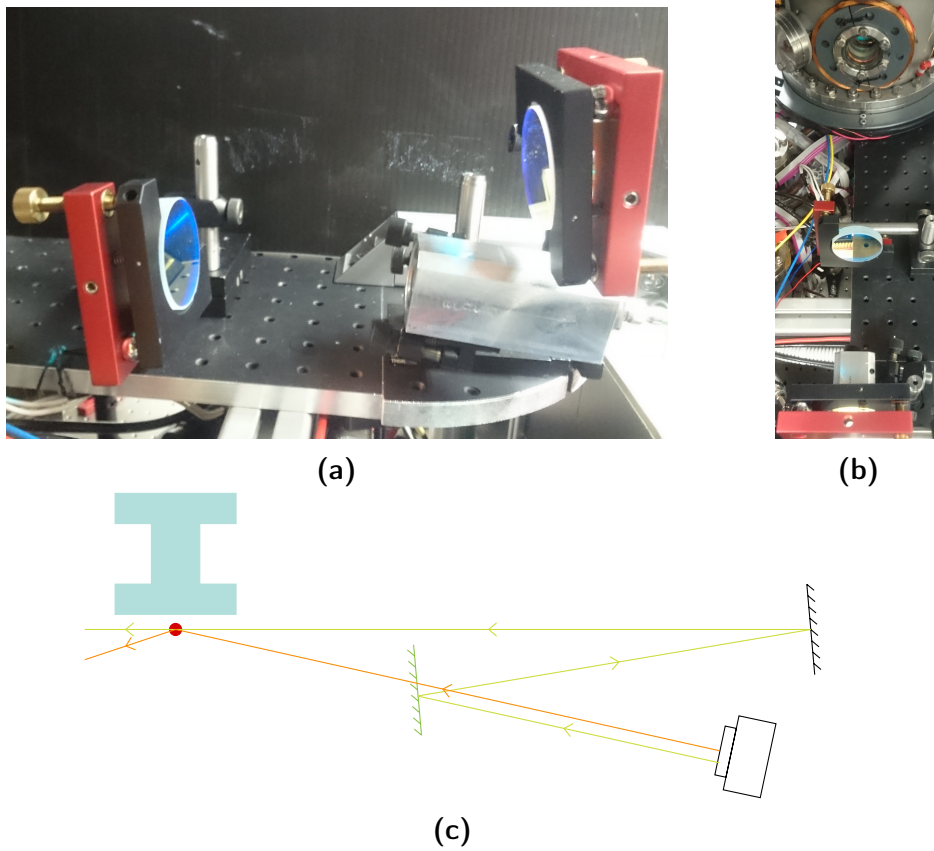


**Figure 3.5.:** Reflective imaging setup for the main imaging direction. The aluminium fiber out-coupler, as seen in (a), is aligned to hit the atomchip at an oblique angle. This allows for cloud to chip distance measurements in the reflective mode. Through inserting the green mirror in (c), on a removable magnetic mount, which is seen on the left in (a), the image beam is reflected to the mirror at the top right. This mirror is aligned to horizontally hit the window in the cryostat, as seen in (b), for normal absorption imaging. (c) shows a sketch of the beam path for reflective imaging (orange) and normal absorption imaging (green). The cloud of ultra cold atoms is indicated by a red dot underneath the blueish quartz chip mount.

After passing through the cryostat, a lens<sup>1</sup> on a translation stage<sup>2</sup> powered by a brushless motor controller<sup>3</sup> collects the un-adsorbed light from the imaging beam. The translation stage is necessary to fine tune the focus and refocus the atomic cloud during longer time of flights (TOF). The trajectory is not a straight path down, due to residual magnetic fields. As seen in fig. 3.6, a mirror bends the optical path to the side due to space constrictions. On a rail, another lens sets the magnification of atom cloud to

<sup>1</sup>Thorlabs AC508 150 B

<sup>2</sup>Thorlabs MTS25/M-Z8 Translation Stage

<sup>3</sup>Thorlabs KDC101 Brushless Motor Controller

### 3. Experimental Setup

about 2.3. Another, through a magnetic mount removable lens, can be added to reduce to magnification to around 1.3. This low magnification mode is used for alignment and optimizing the loading process into the chip trap.

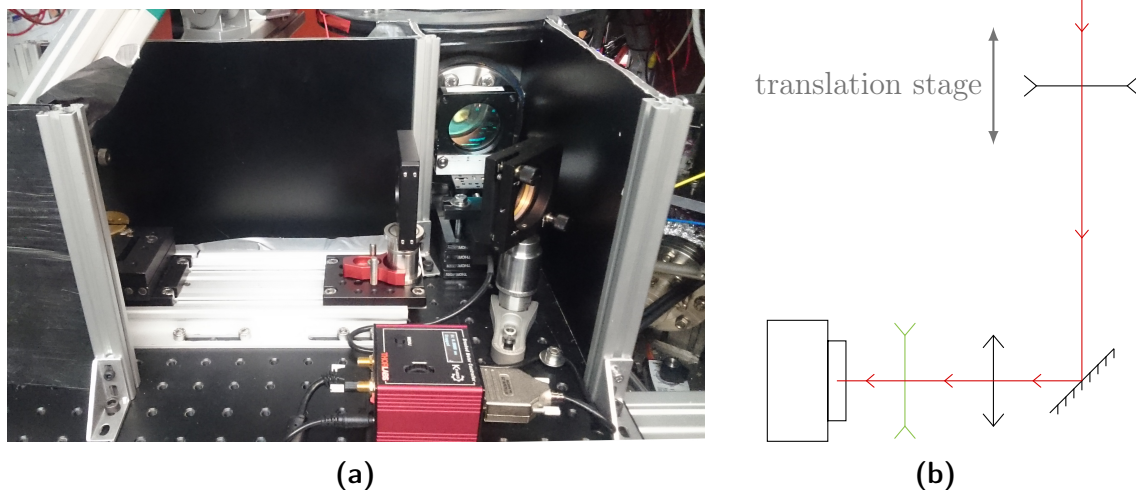


**Figure 3.6.:** Main imaging setup at the back of the cryostat, with a translation stage to fine tune the focus, indicated with grey arrows in (b). The tunable lens in the upper right corner of and controller in the center bottom of (a). Furthermore, a magnetic detachable lens, behind the Item bar to the left in (a), can reduce the magnification for e.g. debugging. In (b) this removable lens is depicted green. Around the entire setup a black cardboard box was devised, to shield it against stray light and therefore reduce the background noise in the pictures.

The resulting reflective imaging picture of the chip, can be seen in fig. 3.7. This is basically a skewed view onto the chip from below, displaying the chip wire and contact pads with their aluminium bonds to the top and bottom. One can imaging how the atoms in a chip trap, can be seen 2 times, below and above the chip wire in the center.

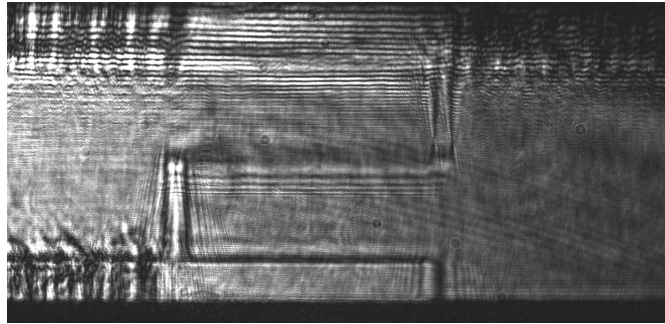


**Figure 3.7.:** Atomchip imaged in reflective mode, to align the setup. The horizontal line with two leads in the middle is the chip wire. At the top and bottom the contact pads with their aluminium bonds are seen.

### 3.3. MOT Chamber

The experimental cycle begins with the MOT-Phase where the 6 cooling beams, cool the magnetically trapped atoms, as described in section 2.2.2. It is built up by a flat stainless steel octagon with openings on each face of it, as seen in fig. 3.8.

In transport direction, it holds the push coil and live view MOT cam (see fig. 3.9) on one side and connects to the magnetic conveyor belt. The direction orthogonal to it, is the optical access for the optical pump beam, where via an attached cross, the pressure gauge as well as a  $50 \text{ L s}^{-1}$  ion pump<sup>1</sup> are connected. On the opposite side the MOT camera is situated, taking absorption images from the imaging beam (see section 3.2.1).

The other 6 windows are used for the 4 horizontal and two vertical cooling beams. The windows for optical access are 5 cm big, to have a rather big volume in which the cooling beams overlap, increasing the number of trapped atoms. To one of the other openings a cross is attached, connecting to a valve, where a turbo molecular pump can be attached in case the vacuum needs to be re-established, e.g. the dispenser, which is connected to the lower end of the mentioned cross, is exchanged or someone forgets to close the gate valve and switches off the cryostat.

---

<sup>1</sup>Varian Star Cell<sup>®</sup>, [www.varianinc.com](http://www.varianinc.com)

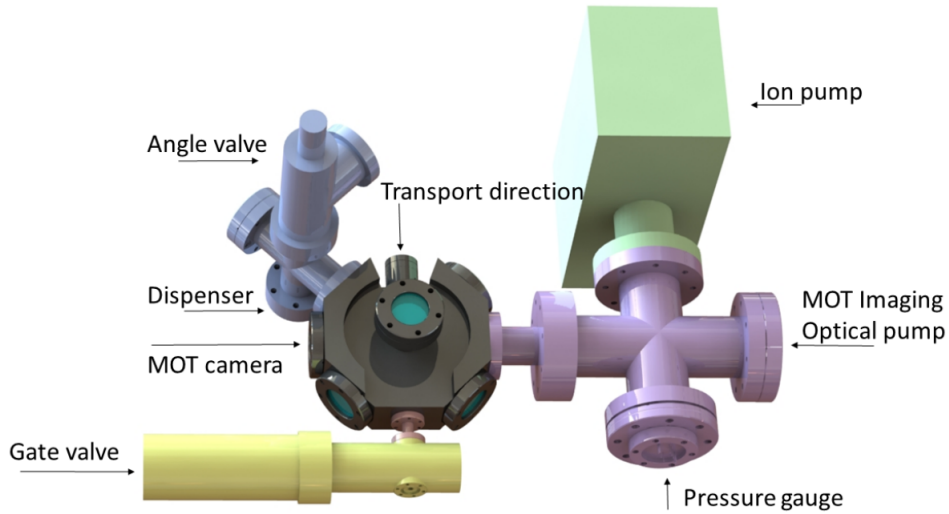


**Figure 3.8.:** Overview of the MOT chamber and things attached to it. The blue cross is connected to a valve which is used when a new UHV in the MOT chamber, needs to be created, by attaching a turbo molecular pump to it. The lower connector of it houses the dispenser as seen in fig. 3.10. The huge purple cross attached to the right gives optical access for imaging and pumping, while having also a  $50 \text{ L s}^{-1}$  ion-pump and ion pressure gauge attached to it. To the bottom the pinkish differential pumping stage and yellow valve connecting to the magnetic conveyor belt are connected.

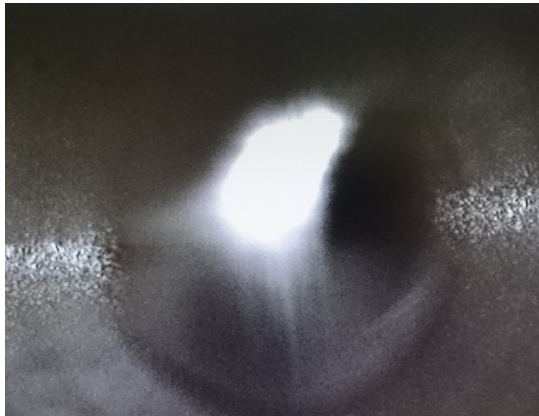


**Figure 3.9.:** Screenshot of the live MOT cam during laser cooling. The bright spot is the fluorescence of the  $^{87}\text{Rb}$  atoms scattering the cooling laser beams.

#### 3.3.1. Dispenser

Although other possibilities have been studied initially in the history of this experiment (see section 3.4), a conventional MOT with a Rubidium vapour source in form of an



### 3. Experimental Setup

---

alkali metal dispenser from SAES Getters<sup>1</sup> is used, as it turned out to be the most viable. The dispenser releases natural Rubidium (27.83%  $^{87}\text{Rb}$ ) through reducing  $\text{Rb}_2\text{CrO}_4$  with zircon and aluminium upon heating. The six dispenser stripes used are heated by applying a DC current of  $\approx 4\text{ A}$ . With this setting they provide sufficient amount of Rubidium, after about an hour of operation, while having a very long life expectancy.

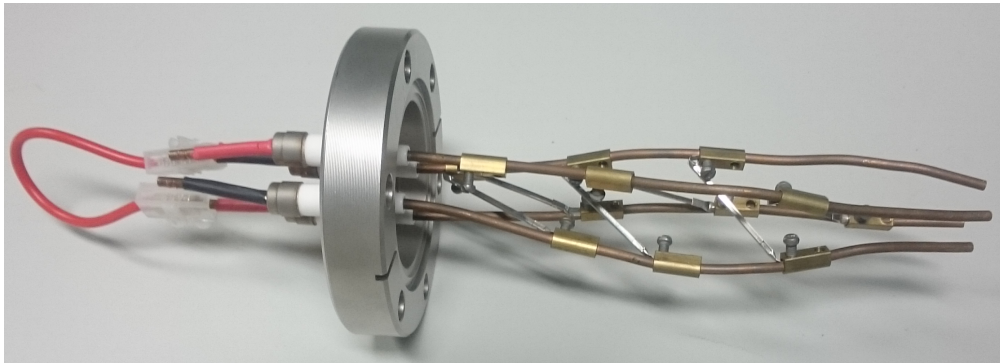


**Figure 3.10.:** Vacuum Conflat<sup>2</sup>(CF) flange with the current feed troughs and copper rods supporting the two in series switched pairs of wires, each holding three rubidium dispensers in parallel.

## 3.4. Atom Transport

The big experimental challenge in this setup is the transport of atoms from the MOT-chamber into the cryostat. This is necessary since laser cooling (see section 2.2.2) and a dispenser as  $^{87}\text{Rb}$  source (see section 3.3.1), would cause problems in the cryostat. Alternatives for a compacter design of this experiment have been studied. Evaporation of atoms with the means of an electron beam [61] and transporting with moving coils [60] or a dipole trap [62], were either insufficient in providing enough atoms for the MOT or impractical. Experimentally, the best method turned out to be a magnetic conveyor belt scheme, as seen in fig. 3.11 and first described in [63]. In order to utilize this method, it was necessary to adapt it in a way, to transport also in vertical direction, since loading the atoms horizontally into the cryostat is impractical and the combination of a horizontal and vertical part reduces stray light in the cryostat. This unique setup is described in [4, 62, 64, 65].

---

<sup>1</sup>RB/NF/14/25/FT10+10;[www.saesgetters.com](http://www.saesgetters.com)

<sup>2</sup>UHV standard for connections according to ISO 3669:2017, with stain less steel blades cutting into copper gaskets



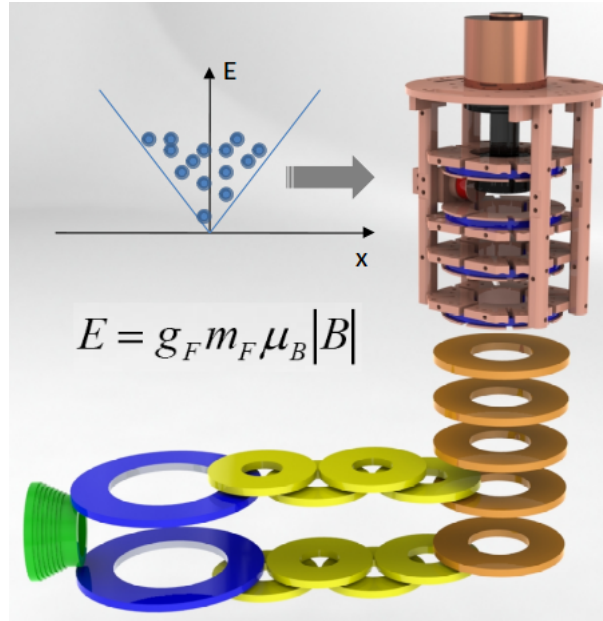


**Figure 3.11.:** Overview of the Magnetic conveyor belt. The blue coil are the MOT coils, from there the green PUSH coils pushes the atoms into the right direction. The yellow coils are NC transporting horizontally (H1-H4). While the orange are the NC coils of the vertical part (V1-V5). The two lowest ones V1 and V2 are at the same time the final two coils from the horizontal part. The blue SC coils (V6-V9) are mounted to the copper 4K stage inside the cryostat.

### 3.4.1. Magnetic Conveyor Belt

The conveyor belt consist of 16 NC and 4 SC coils. It is divided into a horizontal part of 210.4 mm and a vertical part of 215 mm length. In the vertical section, the coils up to V5 are NC. All 16 NC transport coils are supplied by only 5 high power Delta<sup>1</sup> current sources, since there are never more than 4 coils active at the same time and the power supplies are rather expensive. A layer of switch boxes, connecting each current source in the correct polarity to one of each current source appointed coils, is added. A detailed explanation of this, can be found in section 6.1.5. The SC coils V6 to V9 within the cryostat are supplied by a group built current source<sup>2</sup>. In the corner, the atoms are trapped between V1 and V2 in a simple quadrupole configuration. From there, the vertical part starts where the atoms are travelling trough the coils' centers upwards. Whenever they cross through a coil the polarity of that coil changes.

Precisely controlling these coils in a safe manner, to transport  $\approx 1.5 \times 10^9$  atoms

<sup>1</sup>Delta-Elektronika, see also [www.delta-elektronika.nl](http://www.delta-elektronika.nl)

<sup>2</sup>Heidelberg current source see [50]

### 3. Experimental Setup

---

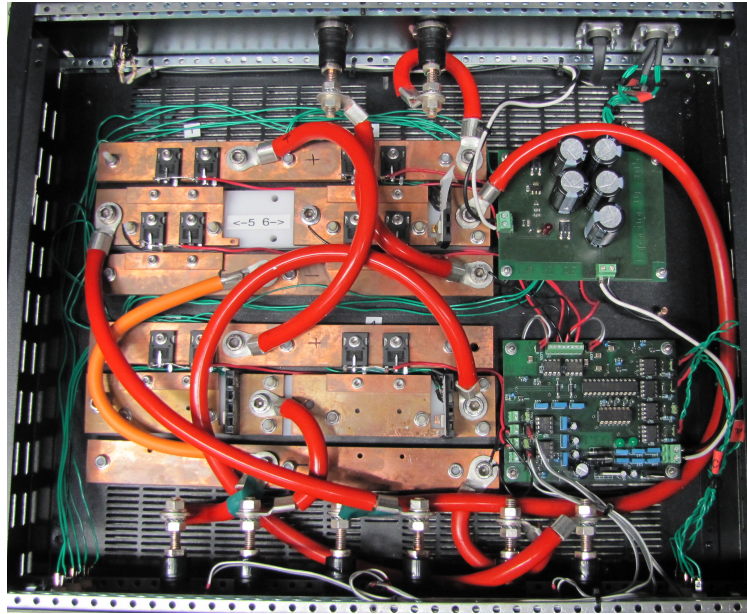


**Figure 3.12.:** Inside of one of the switch boxes: On the right is the electronic demultiplexing the digital inputs to various internal states. While on the left is the high power part, where the MOS-FETs between the copper planes are switched to route the input at the top to one of the various output connectors at the bottom.

with minimal losses over a distance of more than 40 cm, is a formidable experimental challenge. Even more, when attempting to do it consecutively, to recombine packages of cold atoms, as described in chapter 6. A more technical description of the transport setup and more information on the coil's properties can also be found in [50].

The entire transport section is connected to the MOT chamber via a differential pumping stage, which is basically just a 31 mm long tube with a small diameter of 7 mm. During operation, it became clear that this is actually unnecessary and is the main limiting factor in transport efficiency. This is shown by the massive atom count drop in horizontal direction at around 60 mm, as seen in fig. 3.13a. After this, a gate valve<sup>1</sup> separates the MOT chamber from the cryostat. Unfortunately, due to concerns that a valve<sup>2</sup> that could be inserted right underneath the cryostat, which is not available in non-magnetic steel, the current configuration with a valve made of non magnetic steel was realized. This is crucial for the reconfigurability time. Whenever the cryostat is opened, despite a cool down time of roughly six hours, it takes about two weeks until the pressure in the transport line is low enough again to have full transport efficiency. Since, it is naturally difficult to reach UHV in a long and thin tube,

---

<sup>1</sup>VAT 48124-CE01 <http://www.vatvalve.com>

<sup>2</sup>e.g. VAT series 010 with "insert" option

### 3. Experimental Setup

---

despite the  $20 \text{ L s}^{-1}$  ion pump connected to the corner of the transport line. Below the corner, there is also a window for optical access to the chip from below, utilized for the quench setup (see section 3.2).

Aside from the difficult task to manage this many coils, the physics behind the magnetic conveyor belt is rather simple. It consists of overlapping coil pairs (MOT<sup>1</sup>, H1-H4) for the horizontal part, a Push coil guiding the atoms in the right direction in the beginning and a stack of coils (V1-V9) for the vertical transport. All these coils, as seen in fig. 3.11, form a continuous arrangement of coil pairs in AH configuration. With the right current sequence applied to it, the magnetic minimum of a quadrupole trap will continuously shift along the transport direction holding atoms, as described in section 2.3.2.

Unfortunately, this approach comes with a loss of atoms during the transport, because during the finite transport time, loss mechanisms as described in section 2.3.5 will take their toll. This contribution to the atom loss is relatively small, as the main loss is due to the differential pumping stage as mentioned above. Therefore, it would make sense to remove that small diameter pipe, since it reduces the transport efficiency to approximately 50% and the actual use of it is questionable.

An additional advantage of the magnetic conveyor belt is to further reduce stray light in the science chamber, due to the corner between horizontal and vertical part. However, the main advantage is that it allows the setup to run multiple MOT cycles in one experiment cycle, as described in chapter 6.

---

<sup>1</sup>In the context of coils MOT denotes the coil pair used in the magneto optical trap, which is also employed during the transport

### 3. Experimental Setup

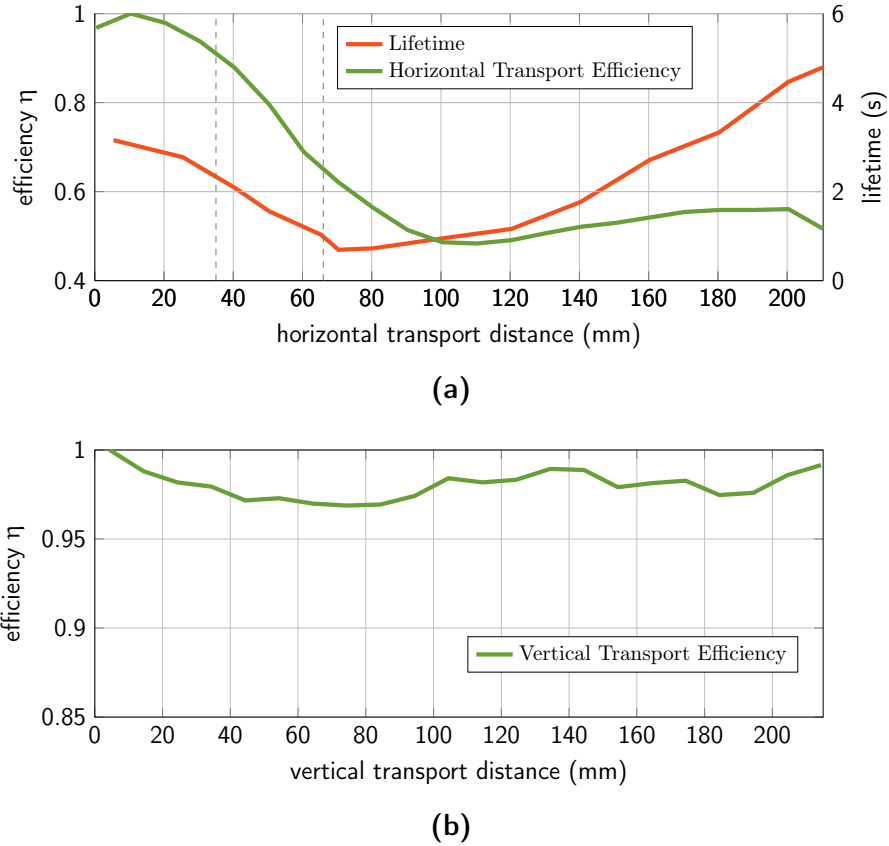


**Figure 3.13.:** (a) shows the loss of atoms during horizontal transport. The grey dashed lines indicates the pipe with a small diameter (differential pumping stage). It lets th atom count drop to about 50 % decreases the lifetime, which actually even gradually increases after passing the small pipe. (b) shows the vertical transport efficiency, which is 100 % and almost constant.

### 3.5. Cryogenic Setup

The experiment chamber is the heart of the entire experiment. The actual experiments take place here, underneath the atomchip, where ultimately the atoms are trapped by the superconducting atomchip. For this, nine coils, the chip and four temperature sensor need to be wired up, out of the cryostat, through appropriate feed-throughs. A reasonable ultra high vacuum needs to be created by various pumps. MW and RF antennas are required to address the atoms and, of course, Optical access is necessary in two directions, to simultaneously image the cloud shape and distance to the chip. This section describes how all these aspects are addressed in his setup, to enable superconducting atomchip experiments with it.

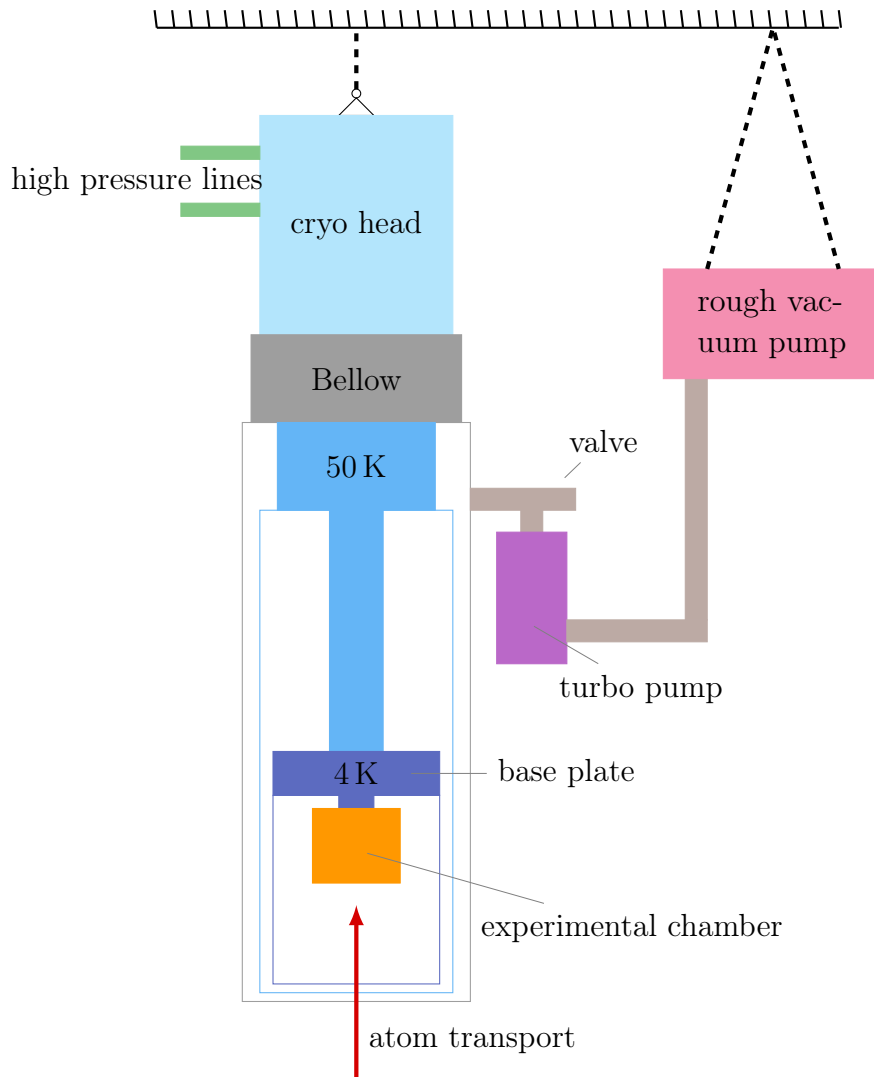


**Figure 3.14.:** Overview sketch of the cryogenic setup: The cryostat with UHV inside is the grey rectangle, where as the two blue rectangles are the 50 K and 4 K shields. It is cooled by the light blue cryo head with its high pressure lines to the compressor in the attic. The UHV is generated by two pumps to the right of the cryostat.

#### 3.5.1. Cryostat

In order to reach low enough temperatures <sup>1</sup> to get the niobium film on the atomchip superconducting, a cryostat is necessary. There are various cryostats available which can do so. Between a wet Helium filled cryostat and a closed cooling cycle cryostat, the obvious choice is the latter, since it requires low maintenance and it is much easier

<sup>1</sup> $T_C \approx 9.2 \text{ K}$  [66]

### 3. Experimental Setup

---

to run continuously. The drawback of such closed cycle cryo is the operation inherent strong vibrations, which would prohibit any ultra cold atoms experiment. However, boiling Helium in a wet cryostat also produces vibrations, which makes mechanical decoupling in any case necessary. Therefore, this setup uses a GIFFORD-MCMAHON cryostat<sup>1</sup>. It is suspended from the ceiling and thermally coupled to the cold finger in the vacuum chamber via a helium filled chamber sealed with a bellow, to allow movement of the table and decouple vibrations of the cryo head. The helium compressor in the attic, with a power of 7.7 kW, provides pressure pulses of approximately 22 bar, which cool down the cold head depicted in fig. 3.15.



**Figure 3.15.:** The cryo head is on top of the cryostat and cools the experimental chamber via a cold finger. It is suspended from the ceiling and mechanically decoupled through a helium filled bellow, as seen in fig. 3.14.

#### Vacuum Pumps

To create UHV in the cryostat, a turbo molecular pump<sup>2</sup> is used. To operate, it needs a pump producing a rough vacuum of approximately  $10^{-6}$  mbar. The turbo molecular pump is directly attached to the cryostat, as seen in fig. 3.16b. To support its weight

---

<sup>1</sup>ARS DE210S cold finger with GMX20-B vibration isolation interface, Advanced Research Systems Inc., Macungie, Pennsylvania, USA

<sup>2</sup>Pfeiffer Vacuum, TMU071P Turbo molecular pump with a TC600 control unit



### 3. Experimental Setup

---

an aluminium base plate was designed to connect it to the Item structure holding the cryostat. The pre-pump<sup>1</sup>, which connects to the outlet of the turbo pump is suspended by wires from the Item construction below the ceiling, as seen in fig. 3.16a, while the connecting tube, is vibration damped by three Item bars from the ceiling. This is crucial to mechanically decouple the pump's heavy vibrations from the experiment. With this setup, it is possible to let the pump run continuous until  $10^{-10}$  mbar is reached in the cryostat and conveyor belt, even while doing experiments. Towards the end of pumping, the cryostat is switched on and through the cryo pumping effect, the pressure decreases significantly further. However, this can not be measured since it is not possible to place an ion-gauge pressure sensor within the 4 K shield.

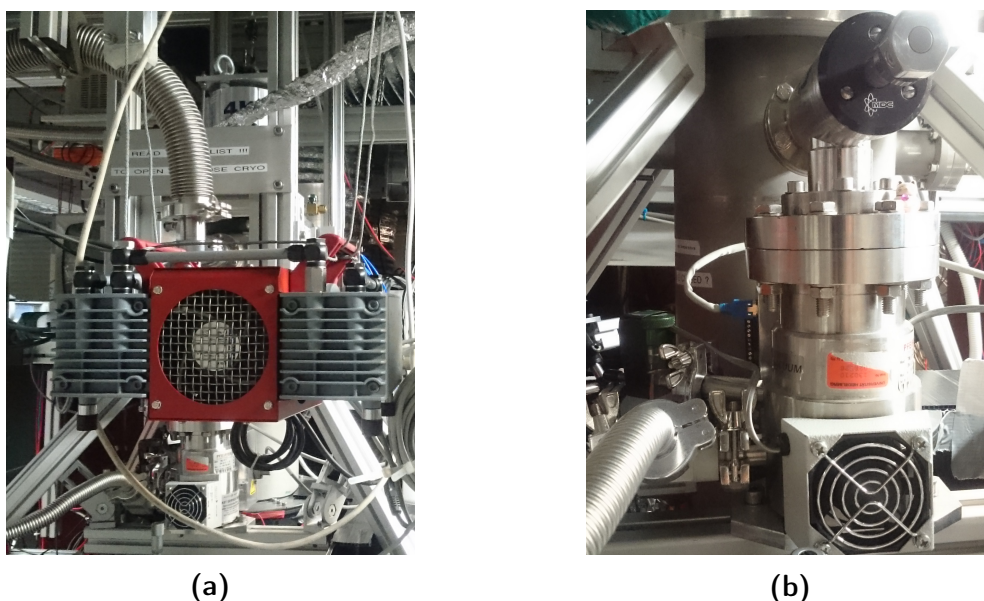


**Figure 3.16.:** (a) shows the rough vacuum pump suspended from the ceiling, as depicted in fig. 3.14. The vacuum tube connecting it to the outlet of the turbo molecular pump is mounted several times with a dampening material to the Item construction below the ceiling, to prevent vibrations transmitted to the cryostat. (b) is the turbo molecular pump, mounted directly to the valve at the cryostat, as seen in fig. 3.14.

#### 3.5.2. Heat Shielding

To reach such low temperatures below  $T_c$  of niobium, the science chamber attached to the cold finger needs to be properly thermally insulated. The UHV provides good protection against heating through convection, but at these temperatures thermal radiation plays a huge role. Therefore, two layers, to shield against thermal radiation,

---

<sup>1</sup>Pfeiffer Vacuum, MVP055 rotary pump; <https://www.pfeiffer-vacuum.com/>

### 3. Experimental Setup

---

are installed. The first one is a mylar wrapped aluminium cylinder with a small hole in the bottom to let through the atoms, attached to the 50 K stage of the cold finger. It also features 4 anti reflection coated windows. The 4 K shield is quite similar with the exception, that it is 3D printed out of PLA and features one lens instead of the anti reflection window in the main imaging direction. Apart from the mylar wrapping reducing heating through thermal radiation, these shields also act as a differential pumping stage, helping to decrease the pressure in the science chamber, where the strong cryo pumping takes place. Figure 3.17 shows the 4 K heat shield and the cold finger reaching up to the 50 K stage, as indicated in fig. 3.14.



**Figure 3.17.:** The 4 K heat shield, attached to the 4 K base plate (see fig. 3.14) shields the experimental chamber from thermal radiation. The upper part of the base plate is wrapped in mylar and aluminium tape to prevent any exposed, less reflective copper parts.

#### 3.5.3. Wiring in Cryogenic Environment

Countless wires are running from a central breakout box into the cryostat to supply all the superconducting coils and measure temperatures. In order to ensure that the temperature gradient is small enough to have a minimal energy input (heat leakage) into the cryostat, the wires needs to be long enough and properly anchored.



#### Normal Conducting Wires

First, a bunch of copper wires inside a bundle of shielded data cables is fed from the break-out-box to three military grade connectors on the feed troughs at the top of the cryostat. From these feed-throughs the copper wires are wound tightly around the cold head of the cryostat. Approximately 4 m of NC wire are used here for each channel. Here simple magnet wire is used due the consideration below.

The empirical WIEDEMANN-FRANZ law [67],

$$\kappa\rho = L_0T. \tag{3.9}$$

states that the product of thermal conductivity  $\kappa$  and electric resistivity  $\rho$  are proportional to the temperature, with the proportionality factor  $L_0$  named after LUDVIG LORENTZ. It is valid for high  $T > T_D$  and low temperatures (i.e a few K). It can be explained with the phenomenological DRUDE-model [68]. In [69] it is argued that based on eq. (3.9), the heat leak  $Q$  per current  $I$  is approximately independent of the temperature and material,

$$\frac{Q}{I} \approx \sqrt{L_0}. \tag{3.10}$$

Therefore, a wire going into a cryostat should not be made out of a particular pure and good metal, since better conductors are in general also good heat conductors. For simplicity, normal magnet wire is used.

#### YBCO stripes

Inside the 50 K stage of the cryogenic setup, the magnet wires are soldered to YBCO high temperature superconducting stripes. This has the advantage of significantly reducing JOHNSON-NYQUIST noise. These stripes are glued with GeVarnish to the Kapton insulated cold finger as seen at the top of fig. 3.18.

#### Niobium wires

As depicted in fig. 3.18 at end of the long cold finger, reaching from the 50 K stage down to the 4 K base plate, the YBCO high temperature superconductors end. Here, niobium titan wires are soldered to them, since from here on downwards it is cold enough for them to be superconducting. Nonetheless, they need to be shielded from thermal radiation with mylar and thermally anchored, as seen in fig. 3.17. This is crucial to reduce any heat flow from out side the cryostat into the experiment chamber. Thermal anchoring is done by tightly wrapping them around copper bobbins screwed

### 3. Experimental Setup

---

onto the 4 K base plate. In fig. 3.18, three of these thermal anchors are seen in the center, wrapped in teflon to mechanically secure the windings.



**Figure 3.18.:** Niobium titan wires painted with pink nail polish, to fix insulation. They are soldered to the YBCO HTSC bands and then routed, in tight contact to the base plate (see fig. 3.14), to the bobbins, where they are tightly wrapped around several times, for good heat anchoring.

During the operation of the experiment, occasionally shorts happened in the wiring inside the cryostat. On one occasion, even melting a wire as seen in fig. 3.19. This was due to the insulation of the magnetic wires being damaged, from countless times moving, unsoldering and re-soldering them. This would require to redo the entire wiring of the niobium wires, since a method to find the uninsulated parts and repair them would have been very time consuming and if simply repairing it, one could never be sure when it might break at an other place again. Instead of completely replacing them, which would have been rather expensive and time consuming as well, since each coil would need to be built new and the Niobium titan wire is rather expensive, an easy method to repair the wires by properly insulating them was found. As a cheap and effective insulation material nail polish was utilized. With this method each wire, from a coil to the respective solder joint, was painted, as seen in fig. 3.18. To easily visually check for a full coverage of each wire, a rather bright color was chosen. After that, just the bobbins of the heat anchors were wound again and the wires were routed in a way to ensure maximal contact with the base plate, for good thermal connection. Concerns that nail polish might not withstand the thermal cycling of switching on

and off the cryostat, were quickly found to be unsubstantiated and that nail polish is somehow suited for cryogenic environments.

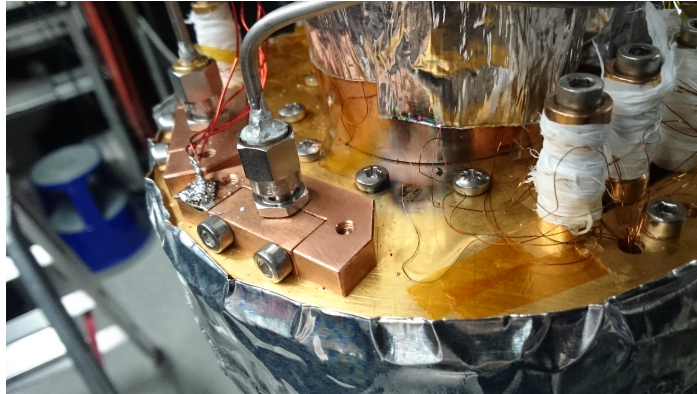


**Figure 3.19.:** Short cut with melted niobium titan wire as it occurred in the cryostat, due to poor thermal anchoring and broken insulation.

## 3.6. Antennas

To address hyperfine transitions and ZEEMAN sub-levels, two RF antennas and one MW antenna have been installed in the science chamber. Mounting them was not straight forward, since a clear line of sight for imaging must not be obstructed, while they should be as close to the chip as possible. Analogue to the NC and SC wires, also the coaxial cable need to be thermally anchored. This is done at the 50 K and 4 K stage, where the cables are fed through the base plates. However, a common problem in high frequency applications in cryogenic environment is that while the outer conductor, which is grounded and well thermally anchored, the inner one is insulated by the dielectric. Therefore, it might happen that the inner conductor is much warmer and leaks heat into the system. This can be solved by placing attenuators into the transmission line, since they have a connection between the inner and outer conductor. In our setup a  $-3$  dB attenuator and a DC block is mounted inside the 50 K shield. The DC block would actually make thermal anchoring even worse. However, we did not notice any heating in the science chamber through the coaxial cables.

### 3.6.1. RF Setup

The RF setup is used to drive transitions with in ZEEMAN-split hyperfine states. This is necessary, to spin flip atoms and make them transparent to the trap for forced evaporative cooling of the atomic cloud.



**Figure 3.20.:** Detailed view of the experimental chamber, which is the orange rectangle in fig. 3.14. The atomchip is suspended from the cold finger and the MW and RF antennas are in close proximity to it. The PCB with ring structures is the MW antenna with a resonance frequency of 6.83 GHz, to address the clock state. The RF antenna is a coil with 20 windings around the chip mounting. Its two connections going up can be seen in the forefront. A second back up RF antenna is on top of the V8 coil, which is, due to its greater distance to the chip less effective.

For Evaporative cooling, one needs to start with a high frequency and decrease it down close to the trap bottom. To achieve this, several linear ramps are used. We start with the first RF source<sup>1</sup>, which does the first coarse ramp from 30 MHz below 20 MHz, then three additional RF sources<sup>2</sup> do finer ramps approaching the trap bottom (see section 4.2.1). Since, there is only one RF antenna, we use in the cryostat, one needs to multiplex the several RF sources to one coaxial cable into the cryostat. This is done by a cascade of RF switches<sup>3</sup>. These switches have two input and one output, routing either a RF source or the next switch to the output. With this method, 3 RF switches and 6 digital inputs are sufficient to connect all four RF sources to one output, as seen in fig. 3.21. From there the signal goes through an attenuator<sup>4</sup> to reduce noise. Then, it is amplified<sup>5</sup> and fed into the cryostat. In the cryostat, there are no further attenuators. In the end the signal is coupled into the primary RF antenna, wound around the chip mounting, as seen in fig. 3.20. This, ensures maximal proximity to the

---

<sup>1</sup>SRS DS345 30 MHz Function Generator

<sup>2</sup>Agilent 320A 20 MHz Arbitrary Waveform Generator

<sup>3</sup>Mini-Circuits ZX 50 DR230-S+ DC-3 GHz SPDT RF Switch

<sup>4</sup>Mini-Circuits HAT-30+ 30 dB Attenuator

<sup>5</sup>Mini-Circuits 50 kHz - 150 MHz, 25 dB Amplifier



chip while not obstructing the line of sight for imaging.

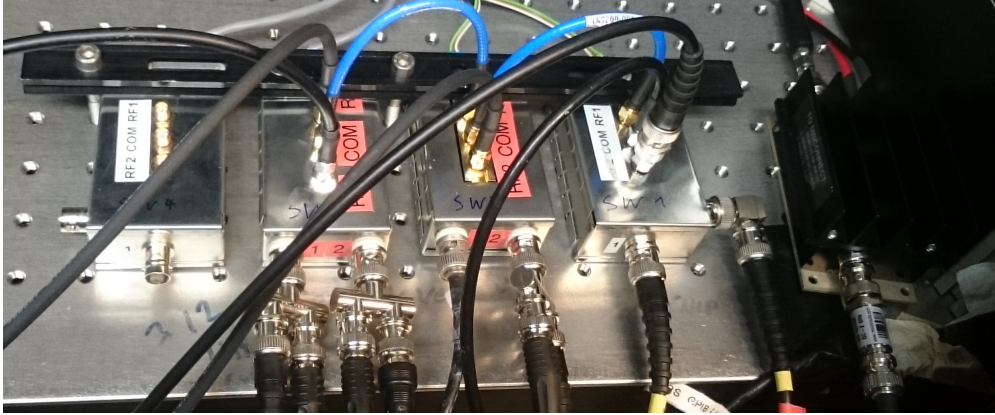


**Figure 3.21.:** RF switch cascade setup: The first two switches from the right connect to the previous switch and a RF source, while the last switch connects to two RF sources. The final output is attenuated by 30 dB to reduce noise and then amplified again by 25 dB in the black amplifier, seen to the right. The fourth switch on the left is not connected and serves as a backup.

#### 3.6.2. Microwave Antenna

The PCB with ring structures seen in fig. 3.20, is our MW antenna with a resonance frequency of 6.83 GHz. It is used to address the  $|F = 1\rangle \leftrightarrow |F = 2\rangle$  transition in the ground state, which will be our clock state. It was designed and tested in a mock up of the science chamber and tuned to the resonance frequency, as good as possible, by adding scraps of aluminium tape to the back. However, at 4 K a shift of the resonance frequency is expected and further tuning will need to be done. For actually hitting the transition, one would just slightly scan the magnetic field around the field necessary for the clock state (see section 2.1.5), to shift the ZEEMAN levels by the second order ZEEMAN shift.

### 3.7. Superconducting Atomchip

The heart of the experiment is the superconducting atomchip. All the other efforts are ultimately made to trap ultra cold atoms on it. The actual chip design may vary and a variety of designs were already built by AIT<sup>1</sup> for us. Some of them are described in

---

<sup>1</sup>Austrian Institute of Technology, <https://www.ait.ac.at/en/>

### 3. Experimental Setup

---

[2]. However, we almost exclusively used simple designs with a plain Z-wire, on which I want to focus here.

These chips consist of a sapphire substrate with a several hundred nm niobium layer on them. Via a mask arbitrary 2D shapes can be created. In a simple design as mentioned above, this would be a Z-shaped wire with contact pads at the sides, as seen in fig. 3.22a. The entire chip is then glued with G-Varnish onto the chip mount made out of quartz. This quartz piece is then clamped with 4 clamps and 8 screws to the cold finger of the cryostat. Between the cold finger and the chip mount, a layer of vacuum grease is applied for better thermal contact. This reduces magnetic active materials to a minimum in the chip's vicinity and ensures good cooling of the chip. Unfortunately, while being UHV proof, G-Varnish is not ideal for low temperatures, as it is not a particular good thermal conductor and tends to change with thermal cycling. This can be seen in fig. 3.22b, where a homogeneous and transparent layer of G-Varnish, harbours voids, which are insulating the chip from the mount.

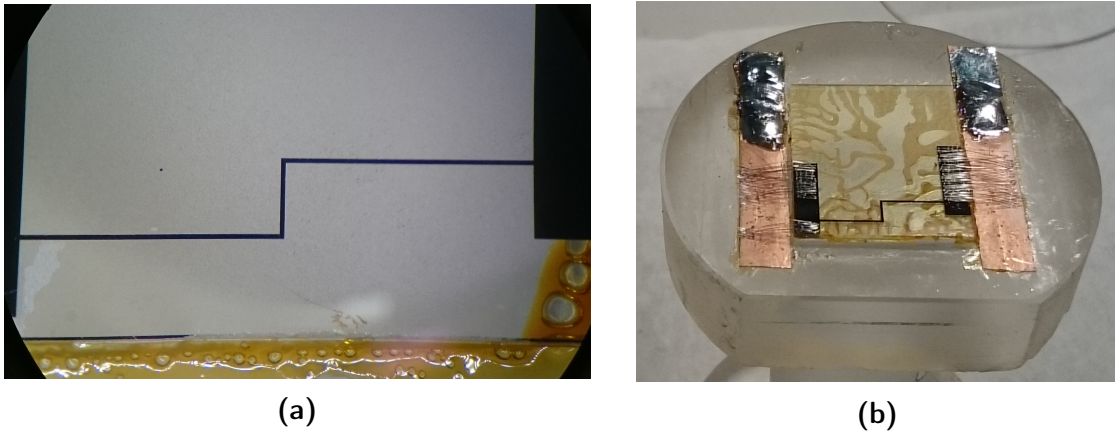


**Figure 3.22.:** (a) shows a close-up view of the superconducting atomchip Z-wire. The yellow residue is GeVarnish, which is used to glue the sapphire substrate chip onto the quartz mounting. (b) depicts the quartz mounting with a Z-wire chip glued onto it. To the left and right two YBCO strips are glued as well with GeVarnish. To those the many aluminium bonds are connected. On these stripes, the Nb-Ti wires can then be soldered. This is necessary, since the niobium oxide layer on the chip is not solder able (see section 3.7.1).

In section 2.3.4, it is explained how our neutral  $^{87}\text{Rb}$  atoms are trapped on such a wire in combination with a bias field. To build a hybrid quantum system, future chips also need to harbour a microwave resonator, with the resonance frequency of our clock transition, situated in close proximity to the trapping wire. Resonators built with the same technique as our current chips, have already been built for testing and are described in section 4.3.2.

### 3.7.1. Chip Contacting

Our superconducting atomchips are made of niobium, which unfortunately, immediately oxidises once exposed to air. This oxide layer is not solderable, while the wires used, consist of many filaments in a copper matrix, which makes them solder able, while they are still fully superconducting. Therefore, other means of contacting the superconducting niobium titan wires to the chip are necessary.

Attempting to use niobium hooks pressing onto the contact pads and other attempts did not work. The currently used method is aluminium bonds. It utilizes the fact that contacting bonds, as used in integrated circuit fabrication, are done by pressing a very thin aluminium or gold wire at a high temperature onto a surface. This basically welds the contacting wire and the contact pad together. In our case, this is enough to break through the oxide layer and generate contact to the chip. While the other end of the bond wire is contacted to a YBCO stripe, glued next to the chip. On this copper coated YBCO stripe the niobium titan wire can then be soldered.

This method however, has a couple of drawbacks. Enormous amounts of such bonds are needed to support with the ,at 4 K still normal conducting, aluminium wires our large chip currents of up to 2 A, without great heating. This can be seen in fig. 3.23. On each side, up to 50 bonds are present. This is also to get some redundancy since while bonding and during operation bonds might break loose through mechanical stress or thermal cycling. Eventually, not enough bonds are present any more to support our typical chip currents and superconductivity is seemingly lost. Which is explained by the fact that each bond creates heat just like a small resistor. When the heat load is bigger than the cryostat cooling power, the temperature rises locally and prevents superconductivity in the contact pads. Furthermore, the bonds may only be placed aside of the central transverse wire, where the atoms are trapped, to not obstruct the line of sight for imaging, evident by the empty patches on the contact pads in fig. 3.23. Lastly the aluminium bonds being normal conducting, are also a source of thermal JOHNSON-NYQUIST noise, in close proximity to the chip.

An alternative solution would be using an indium-roses alloy solder( $\text{Bi}_{50}\text{Pb}_{28}\text{Sn}_{22}$ ) as investigated by [70, 71]. With this material the bonds and YBCO stripes would be obsolete and the niobium titan wires could be soldered directly onto the chip, solving most the problems stated above.

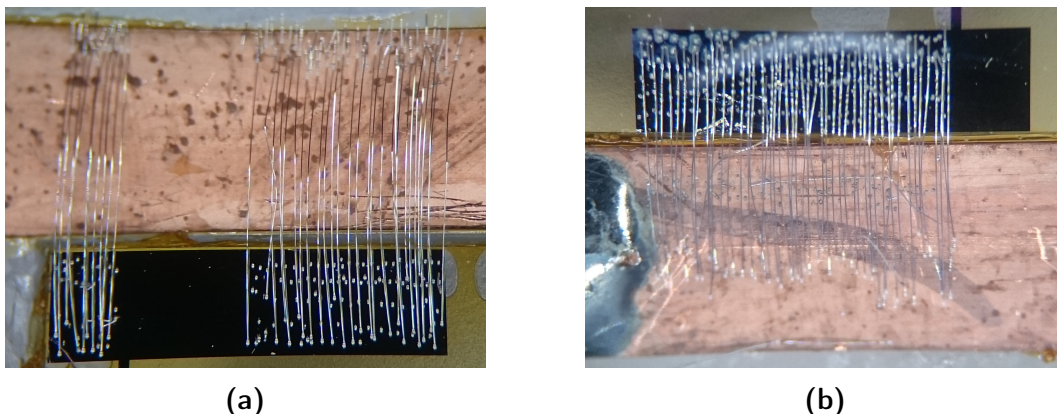


**Figure 3.23.:** Aluminium bonds on the niobium oxide layer: (a) shows the contact-pad towards  $x+$  direction. The gap in the Al bonds ensures a free line of sight, to image the atoms when they are closely trapped to the chip surface. (b) shows the contact-pad towards the  $x-$  direction.

## 3.8. Experiment Control and Monitoring

As evident from the previous chapters, this setup is rather complex for a table top experiment. To precisely time control the many coils, switches, lasers, shutters, etc. in experimental cycles varying from around 15s to up to a few hundred seconds. Furthermore, while operating the experiment, monitoring the cycle and important parameters is vital for taking data. The high currents used for the MOT and magnetic transport and the operation of UHV at cryogenic temperatures is also a security concern and therefore, needs monitoring and fail safe systems. The following sections, provide a short overview of these systems and underline the importance of proper data logging, when running an experiment.

### 3.8.1. ADWIN Controller

To control the experiment, the real time processor ADwin<sup>1</sup> is used, to control all the devices in the lab. To program the experimental cycle and load it to the ADWIN PC, some software is needed. As most experiments in this group, an elaborate Matlab program developed in this group, was used. It works by dividing the experimental cycle for each of our 64 digital and 32 analog channels in 15 sequences. Each sequence length can be set and one can let the channel either be constant or do a ramp for analog channels or decide to flip the state for digital ones.

---

<sup>1</sup>Jäger ADwin, <https://www.adwin.de/>



### 3. Experimental Setup

MOT																exp1	exp2															
Detuning [MHz]	0	C	0	R	-25.5	C	-25.5	C	-25.5	R	-87.7	C	-87.7	R	-36	C	-36	R	0	C	0	R	-3.5	C	0	R	0	C	0	C	0	C
1	calibrate	5	5	9990.11	0.02	2.5	5	0.9	0	2.01	50	10	466.58	10	0	0	0	0	0	0	0	0	0	0	0	0	0	0	0	0	0	0
2	unused	0	C	0	C	0	C	0	C	0	C	0	C	0	C	0	C	0	C	0	C	0	C	0	C	0	C	0	C	0	C	
3	calibrate	1	0	0	0	0	0	0	0	0	0	0	0	0	0	0	0	0	0	0	0	0	0	0	0	0	0	0	0	0	0	0
MOT comp [nA]	0	C	0	R	5	C	5	R	5	C	450	R	450	C	0	R	0	C	0	C	0	C	0	C	0	C	0	C	0	C		
5	calibrate	5	5	9990.11	0.02	2.5	5	0.9	1	2.01	50	10	466.58	100	1	0	0	0	0	0	0	0	0	0	0	0	0	0	0	0	0	0
6	unused	0	C	0	C	0	C	0	C	0	C	0	C	0	C	0	C	0	C	0	C	0	C	0	C	0	C	0	C	0	C	
7	calibrate	1	0	0	0	0	0	0	0	0	0	0	0	0	0	0	0	0	0	0	0	0	0	0	0	0	0	0	0	0	0	0
8	unused	0	C	0	C	0	C	0	C	0	C	0	C	0	C	0	C	0	C	0	C	0	C	0	C	0	C	0	C	0	C	
9	calibrate	1	0	0	0	0	0	0	0	0	0	0	0	0	0	0	0	0	0	0	0	0	0	0	0	0	0	0	0	0	0	0
Co AOM [V]	0	C	0	R	0.7	R	0.7	C	0.7	C	0.7	R	0.7	C	0.7	R	0.7	C	0.7	C	0.7	R	0.4	C	0.4	R	0.8	C	0.4	C		
10	calibrate	5	5	9937.98	2.02	50	0	1.1	7.2	0.01	0.2	0	0.1	50	10	466.58	1	0	0	0	0	0	0	0	0	0	0	0	0	0	0	0
11	unused	0	C	0	C	0	C	0	C	0	C	0	C	0	C	0	C	0	C	0	C	0	C	0	C	0	C	0	C	0	C	
12	calibrate	5	5	9937.98	2.02	50	0	1.1	7.2	0.01	0.2	0	0.1	1370	10	466.58	0	0	0	0	0	0	0	0	0	0	0	0	0	0	0	0
13	unused	0	C	0	C	0	C	0	C	0	C	0	C	0	C	0	C	0	C	0	C	0	C	0	C	0	C	0	C	0	C	
14	calibrate	1	0	0	0	0	0	0	0	0	0	0	0	0	0	0	0	0	0	0	0	0	0	0	0	0	0	0	0	0	0	0
TRANS V6a	0	C	0	C	0	C	0	C	0	C	0	C	0	C	0	C	0	C	0	C	0	C	0	C	0	C	0	C	0	C	0	C
15	calibrate	1	0	0	0	0	0	0	0	0	0	0	0	0	0	0	0	0	0	0	0	0	0	0	0	0	0	0	0	0	0	0
16	unused	0	C	0	C	0	C	0	C	0	C	0	C	0	C	0	C	0	C	0	C	0	C	0	C	0	C	0	C	0	C	
17	calibrate	1	0	0	0	0	0	0	0	0	0	0	0	0	0	0	0	0	0	0	0	0	0	0	0	0	0	0	0	0	0	0
TRANS V6b	0	C	0	C	0	C	0	C	0	C	0	C	0	C	0	C	0	C	0	C	0	C	0	C	0	C	0	C	0	C	0	C
18	calibrate	1	0	0	0	0	0	0	0	0	0	0	0	0	0	0	0	0	0	0	0	0	0	0	0	0	0	0	0	0	0	0
19	unused	0	C	0	C	0	C	0	C	0	C	0	C	0	C	0	C	0	C	0	C	0	C	0	C	0	C	0	C	0	C	
20	calibrate	1	0	0	0	0	0	0	0	0	0	0	0	0	0	0	0	0	0	0	0	0	0	0	0	0	0	0	0	0	0	0

Figure 3.24.: Screenshot of Matlab ADwin program, while loaded the analog 1 panel for the MOT cycle.

However, this program is quite old, buggy and not easy adaptable to future applications. As seen in fig. 3.24, each channel is limited to 16 operations, which is a big constrain for such a complicated experiment and long cycles. Especially to implement atomic recombination as described in chapter 6.

### 3.8.2. Experimental Controller

As mentioned above the old Matlab control software for our ADwin PC is not suited to change the transport scheme as described in chapter 6. Therefore, to implement these current sequences, a new control software was needed. We utilized the Experimental Controller, which was developed by QI LIANG for the Lithium experiment in this group [72]. This, in C++ with Qt written, controller has many more options than the old Matlab program. More importantly, it enables to freely change the transport currents, by feeding in files which will then be interpolated to get the necessary voltages for each time step. Figure 3.25 shows a screenshot of the controller with the typical MOT and transport sequence.

The controllers main innovative concept, compared to the old Matlab implementation, is that the experimental cycle is divided into sections and sequences. Each section is made up of several sequences which can be a constant, pre-defined functions such as linear ramps or interpolated data files. The section can then, be rearranged and various experimental cycles can quickly be generated by putting different sections together. Before the experiment is run, by loading the parameters, the experiment cycle is fully

### 3. Experimental Setup

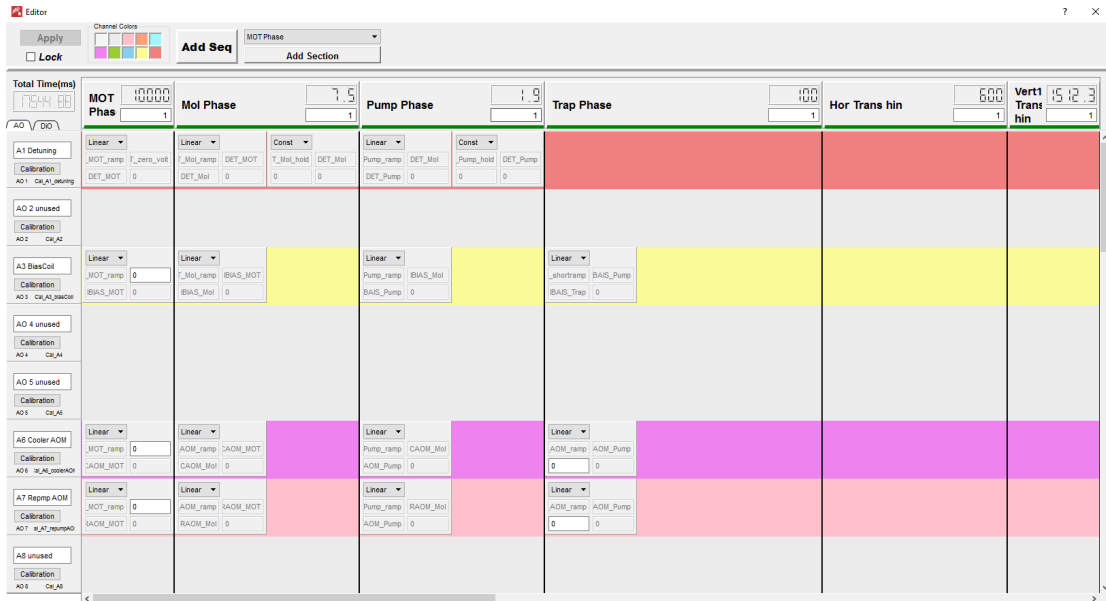


**Figure 3.25.:** Experimental Controller screenshot of a typical MOT and transport sequence.

calculated. Since, the calculation is in contrast to the Matlab program, fully done on the PC running the Experimental Controller, the real time computer ADWIN has more CPU capacity and can run with finer time deviations. To illustrate the complexity of our control voltage sequences just needed for transport, which are then uploaded to ADWIN, an exemplary sequence is depicted in fig. 3.26.

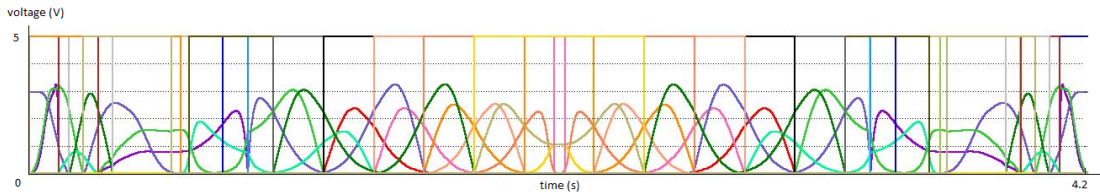


**Figure 3.26.:** Control voltages for a full round-trip transport, as it is used to benchmark the transport. For readability labels are omitted.

#### 3.8.3. Monitoring

The complex setup as described in this chapter, is due to its many interacting, mostly self built, sub systems subject to external influences and is error-prone. Therefore, to do measurements with the experiment, monitoring and logging as many parameters as possible is crucial, to be able to efficiently debug in case of a problem. Furthermore,

### 3. Experimental Setup

---

for valid measurements and especially comparison between such, constant conditions for the experiment are important.

In our setup, various efforts are made to monitor the experiment, but considering the complexity of the setup, these efforts should be certainly increased. So far the currents for most of the coils are monitored by National Instruments hardware and LabVIEW<sup>®</sup> VIs. Pressure and temperature in the cryostat are also monitored and logged by VIs and an alarm is triggered, when the temperature or pressure rise above set values. This monitoring system is described in more detail in [50]. Expanding it to more observables as e.g. laser stray light intensities, EM noise or environmental parameters as humidity, background light and temperature, would simplify debugging and interpreting measurements.

## 4. Towards Hybrid Quantum System

As mentioned in chapter 1, a setup with a superconducting atomchip coupling a cloud of ultra cold atoms to a microwave resonator is a promising prospect. The recent advancements of the setup described in chapter 3, brought this project much closer to realize such a hybrid quantum system. The requirements calculated in [1] to achieve strong coupling between a  $^{87}\text{Rb}$  BEC and a microwave photon, as used in a SQC, are relatively optimistic. They aim to achieve a coupling of 40 Hz with an BEC containing  $10 \times 10^6$  atoms, at a distance of  $1 \mu\text{m}$  from a co-planar wave guide  $\frac{\lambda}{2}$  resonator. This chapter describes the current status towards such a hybrid quantum system on a superconducting atomchip.

### 4.1. Atomchip loading

As a first step, the cold atoms have to be loaded onto the chip, after initially cooling in the MOT, magnetic transport and loading into the qulc trap. Although evaporative cooling and condensation could be also done in the qulc trap, it is vital to load the atoms into the chip trap. The closer proximity to the chip and higher trapping frequencies are crucial to attempt strong coupling. Despite the trap geometry being identical, their quadrupole fields are rotated by  $45^\circ$ . Therefore, loading the cold atoms from one into the other trap is not trivial.

It is done by a so called swing-by maneuver. This is necessary, to switch to the rotated field configuration. Figure 4.1 shows the magnetic bias fields as well as the qulc and chip currents during the chip loading. Just using simple linear ramps for the trap currents to change from qulc to chip trap is not sufficient and all atoms would be lost. A vertical bias field to push the atoms away from the chip is applied during the beginning of the sequence, while the chip trap bias field HBIM is first ramped up in the opposite direction and then down to the value creating a trap above the chip. This leads to the characteristic swing by trajectory of the atoms, seen in fig. 4.2a. During that duration, the cloud moves about 2 mm upwards, closer to the chip and

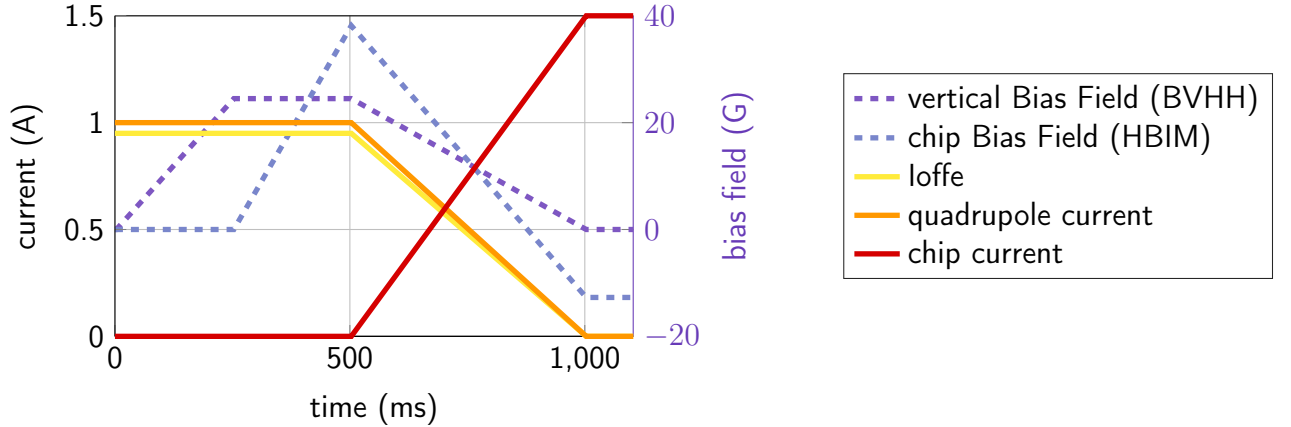


**Figure 4.1.:** Linear current ramps applied to the trapping coils/wires to transfer from the quIC trap to the chip trap. At the same time a vertical and transversal bias field are applied to smoothly transfer the atoms into the  $45^\circ$  rotated quadrupole field of the chip trap.

its density increases significantly, as seen in (fig. 4.2b). Currently, we manage to load approximately  $2 \times 10^6$  atoms at  $20 \mu\text{K}$  into the chip trap, whereas the limiting factor is the magnetic transport, as mentioned earlier in section 3.4.1. In [4] the scheme is explained in greater detail.

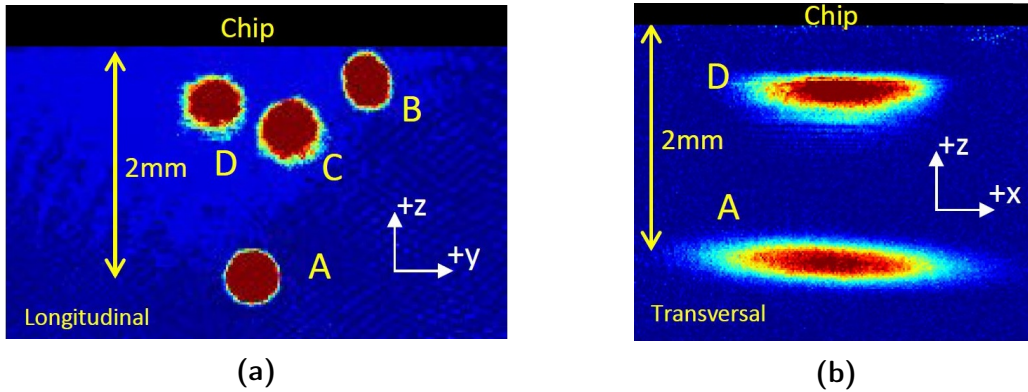


**Figure 4.2.:** Swing by maneuver from (a) longitudinal direction (Ioffe cam) and (b) transversal direction (main imaging camera): The points A to D represent the trajectory of the atom cloud during the atomchip loading. (figure taken from [4])

In terms of distance, we can observe chip to cloud distances of minimal  $50 \mu\text{m}$  by reducing the vertical bias field or increasing the chip bias field. Unfortunately, a smaller cloud to chip distance significantly reduces the lifetime, since technical noise picked up through the chip supply induces spin flips (section 2.3.5). Avoiding that noise, could probably improve this restriction drastically.

## 4.2. Ultra Cold Atoms in a Superconducting Environment

The next step is to further cool the ensemble of cold atoms, to eventually condensate it into a BEC. This is done by forced evaporative cooling. The first and up to now, only BEC on a superconducting atomchip was realized by [73]. Apparently creating a BEC in a cryogenic environment is, despite the advantages, not that easy.

### 4.2.1. Trapping Parameters

Before attempting evaporative cooling with the setup from section 3.6.1, the atom cloud has to contain a sufficient amount of laser cooled atoms with a long enough lifetime. A long lifetime is ensured by low enough background pressure (see section 2.3.5) and a non-zero trap bottom (see section 2.3.4) to reduce spin flip losses as described in section 2.3.5. We achieved lifetimes of up to 200 s and estimate the pressure within the 4 K shield to be considerable below  $10^{-10}$  mbar. For a final atom count in the quIC trap,  $5 \times 10^8$  atoms were achieved, whereas this number is mostly limited by the transport, why improvements such as described in chapter 6 and section 3.4 would be vital. This provided two important parameters, the trapping frequency and the trap bottom, need be known in order to design a RF-knife for evaporative cooling.

#### Trapping Frequency

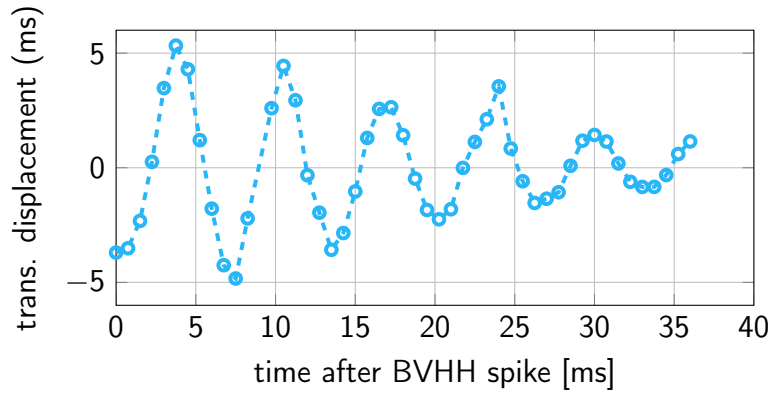
The trapping frequency is basically defines, how tight the atoms are trapped, determining how often atoms oscillate within the harmonic potential of the trap. Therefore, governing the rethermalization speed of the ensemble. For evaporative cooling this is a crucial property limiting speed of the RF-knife.

It can be measured by simply perpetuating (shaking) the ensemble and looking at its damped oscillation period, relaxing back to the equilibrium position. This is done by abruptly changing a current of one of the trapping coils or wires by a small amount.

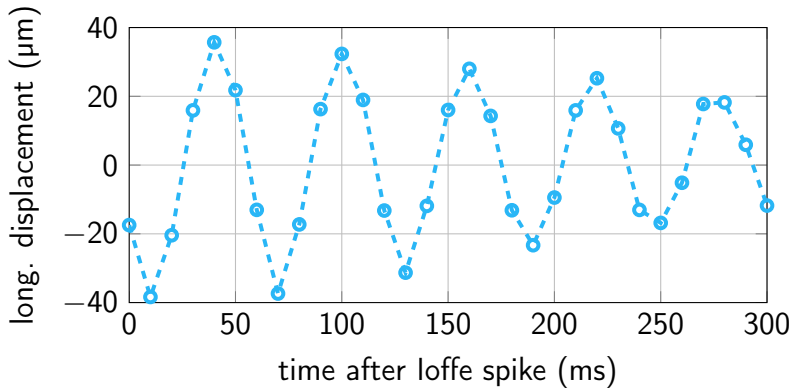
Depending on which current gets perpetuated, the trap is moved in an other way, thus leading to oscillations in the different directions longitudinal or traversal. Due to symmetry, there is only one traversal direction, where the confinement naturally is much tighter then in longitudinal direction, resulting in a quasi 1D system. Table 4.1 shows which current perturbation leads to which trapping frequency.

perturbed magnetic field	trap	direction
vert. bias (BVHH), hor. bias (HBIM)	quIc	trans.
Ioffe, hor. bias (HBIO)	quIc	long.
vert. bias (BVHH), hor. bias (HBIM)	chip	trans.
hor. bias (HBIO)	chip	long.

**Table 4.1.:** Magnetic fields to perturb, to measure different trapping frequency. Naturally, for the transverse direction, since the traps are quasi 1D, it does not make a difference if perturbed vertically or horizontally. Analog for longitudinal perturbation Ioffe and the horizontal bias are both suited to measure the longitudinal quIc trapping frequency, where HBIO, HBIM and BVHH are the corresponding names of the coils.



(a)



(b)

**Figure 4.3.:** Trapping frequencies plots: (a) shows the transversal oscillation in the quIc trap after a perturbation by the vertical bias field. (b) depicts the longitudinal oscillation of the quIc trap triggered by a small current spike in the Ioffe coil.

The described method effectively shakes the entire trap. Then, by imaging with increasing waiting time, until an in-situ picture is taken, lets one see the evolution of the cloud position, as seen in fig. 4.3 and fig. 4.4. From this plot showing a damped oscillation, via a FFT, one can extract the trapping frequency.

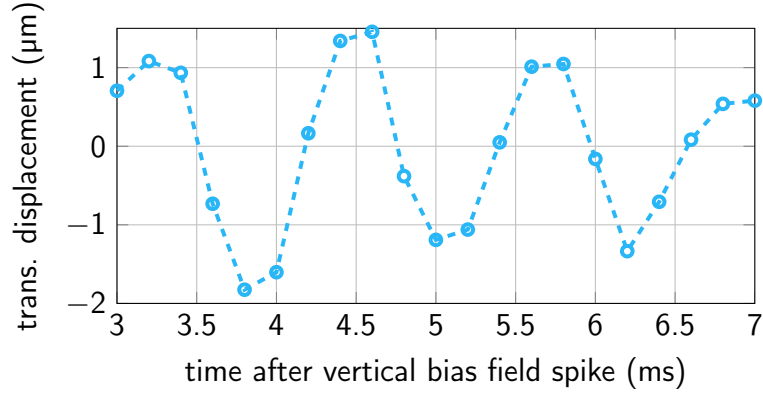


**Figure 4.4.:** Transversal oscillation in the chip trap, triggered by a short vertical bias field perturbation.

We achieved trapping frequencies of  $\approx 16$  Hz longitudinal and  $\approx 160$  Hz traversal for the qulc trap with an  $I_{\text{series}}$  current of around 550 mA. Analogous, the chip trap has similar small  $\approx 20$  Hz longitudinal trapping frequencies, whereas the traversal direction trapping frequency is significantly higher  $\approx 730$  Hz, as seen from fig. 4.4. Due to the higher chip current of  $I_{\text{chip}} \approx 2$  A and close proximity to the chip, the magnetic gradients are much stronger than in the qulc trap.

### Trap Bottom

The other important parameter to know, is the trap bottom. This frequency determines how deep the trap is, which corresponds to when all atoms that are leaked out, when a constant RF-signal at a certain frequency creates a hole in the trap for 30s. As seen in fig. 4.5, the RF-signal keeps reducing the atom count with decreasing frequency, until it hits the trap bottom. There, all atoms are gone. Then the atom count starts rising again, since they are not addressed any more.



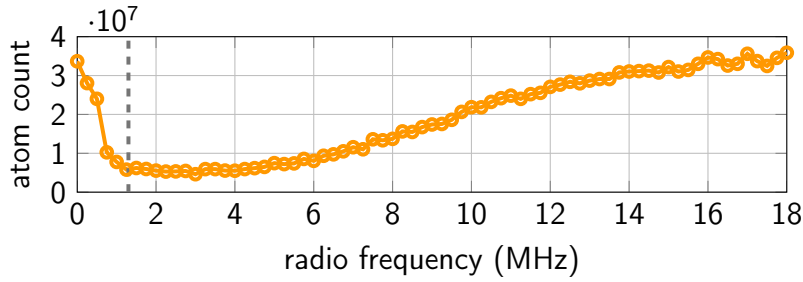


**Figure 4.5.:** Trap bottom spectroscopy of the quic trap: By applying a RF-signal for 30 s at a certain frequency, a hole is poked into the trap at a certain height. By scanning the RF frequency down until all atoms are gone, the trap bottom is found. The gray line indicates the trap bottom at 1.3 MHz.

### 4.2.2. Towards a Degenerated Quantum gas

Macroscopically at "high" temperatures, our atom cloud can be described classically, as a non-interacting thermal gas inside a harmonic potential. At very low temperatures a dilute gas will eventually show quantum degeneracy, where the gas is not behaving according to the BOLTZMANN distribution any more.

#### BOSE-EINSTEIN Condensation

$^{87}\text{Rb}$  has a nuclear spin of  $I = 3/2$ . Therefore, it has an integer total spin  $F$ , which makes  $^{87}\text{Rb}$  a boson. Bosonic gases be condensed into a BOSE-EINSTEIN condensate. The occupation numbers for a non-interacting a bosonic gas is given by the BOSE-EINSTEIN distribution [74–76], which is written as,

$$\langle n \rangle_{\text{BE}} = \frac{1}{e^{\beta(\epsilon - \mu)} - 1}, \quad (4.1)$$

where  $\beta = \frac{1}{k_{\text{B}}T}$ ,  $\epsilon$  is the single particle energy and  $\mu$  denotes the chemical potential.

For a BOSE gas at low temperatures, we can neglect the zero point energy and the chemical potential  $\mu$  approaches zeros. When  $N$  equals the  $N_{\text{ex}}$  the number of excited atoms, atoms will start to populate the ground state. Through this we can calculate a criteria for condensation. The total particle number  $N$  is calculated by an integral over the energy. Calculating it [77], one gets

$$n\lambda_{\text{th}}^3 = \zeta\left(\frac{3}{2}\right) = 2.612, \quad (4.2)$$

where  $n$  denotes the density of atoms and  $\zeta(z)$  is the RIEMANN zeta function.  $\lambda_{\text{dB}}$

denotes the thermal DE BROGLIE wavelength [78], for  $^{87}\text{Rb}$ , written as,

$$\lambda_{\text{th}} = \sqrt{\frac{2\pi\hbar^2}{mk_{\text{B}}T}} = 1.86 \times 10^{-10} \text{ K}^{1/2} \text{ m} \frac{1}{T^{1/2}}. \quad (4.3)$$

$\lambda_{\text{th}}$  is the mean DE BROGLIE wavelength  $\lambda_{\text{dB}} = \frac{h}{p}$  of an atomic gas at temperature  $T$ .

The product  $n \cdot \lambda_{\text{th}}^3$  is actually the phase space density (PSD)  $D$ . With this, eq. (4.2) gives a criteria for the phase space density,

$$D \geq 2.612. \quad (4.4)$$

Although the calculation for eq. (4.2) is made for a free bosonic gas and not one in a harmonic potential, it is argued in [79], that these two cases are not fundamentally different. Therefore we can use it as an indicator for our atoms in a harmonic trap. With the density for an harmonic potential  $n \sim \frac{N}{T^{3/2}}$  from [80] and eq. (4.3) inserted in eq. (4.2), we get

$$D \sim \frac{N}{T^3} \cdot 6.52 \times 10^{-30} \text{ K}^{3/2} \text{ m}^3 \geq 2.612. \quad (4.5)$$

### Phase Space Density Increase

Starting from a laser cooled cloud close to the recoil limit (see section 2.2.3) and knowing the relevant trap parameters we can start forced evaporative cooling, which is the last step generating a BEC. In our experiment, we start forced evaporative cooling already in the qulc trap, where the cloud has a temperature of about 500  $\mu\text{K}$ . We do a first RF ramp to pre-cool the cloud before we transfer into the chip trap, as described in section 4.1.

The speed of the RF-knife for the forced evaporative cooling, is governed by the collision rate in the cloud, since two body collisions will thermalize the ensemble back to equilibrium, after hot atoms are removed. The effect of increasing  $D$  for a RF-knife ramped closer to the trap bottom, can be seen in fig. 4.6.

Our best attempt to condense the cloud, was in the chip trap after pre-cooling in the qulc trap, utilizing 3 RF generators. With the RF ramps depicted in fig. 4.7, we could reach an PSD increase to  $1 \times 10^{-7}$ . Obviously these ramps have to be further optimized, to effectively cool the atoms without kicking out too many atoms (see section 7.1) and reach a  $D \geq 2.612$ . When looking at the temperature, our  $T \sim 4 \mu\text{K}$ , we are not too far away from typical  $T_{\text{C}} \sim 300 \text{ nK}$ .

Another scheme would be to stay in the qulc trap to condensate. It is further away

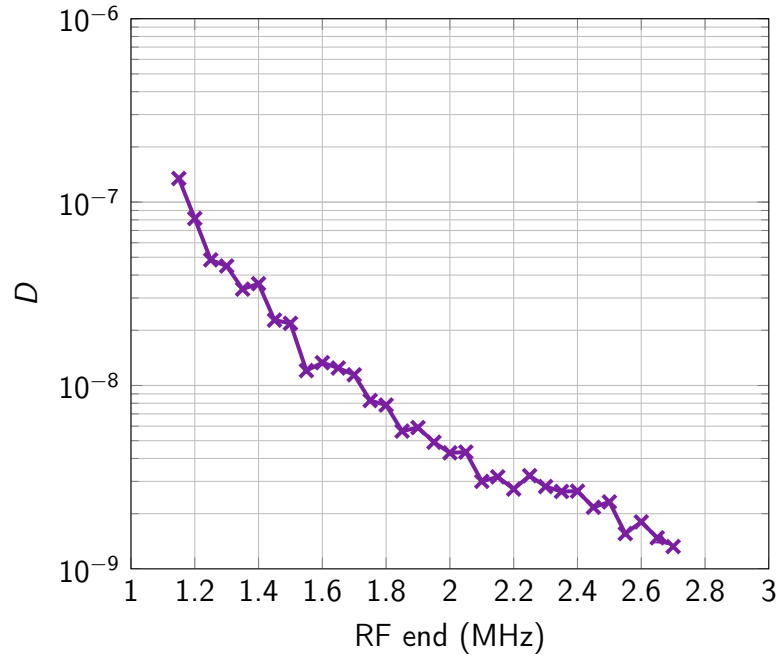


**Figure 4.6.:** Phase space density increase, when letting the RF-knife cut closer to the trap bottom of 1.3 MHz, as depicted in fig. 4.5.

from the chip and therefore less disturbed by noise on the chip. However, the trapping frequency is much less and therefore the collision rate significantly reduced, requiring a longer rethermalization time.

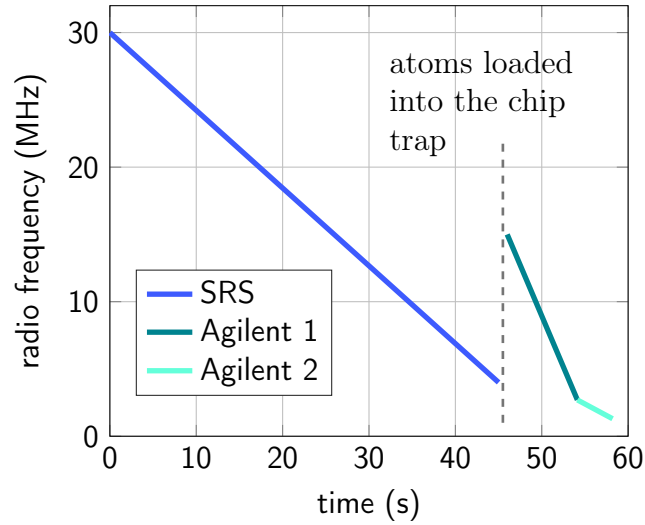


**Figure 4.7.:** RF ramps used for our RF-knife for forced evaporative cooling down to a PSD of  $1 \times 10^{-7}$ . First the cloud is pre-cooled, by a Stanford Research System RF generator, in the quIc trap and then two further ramps, by Agilent arbitrary wave form generators, were applied in the chip trap.

### 4.3. Superconducting Microwave resonators

Parallel to our efforts to generate a condensate, we started developing superconducting microwave resonators to gain experience designing and producing such. In a first step, we made a small series with varying parameters which will be tested in a bath cryostat. The idea is to build up the experience, to know how to design them with resonance frequencies very close to the required frequency of 6.83 GHz. At the same time, they need sufficient high Q-factors, for which the ambitious goal is  $10^6$ .

#### 4.3.1. Probe Stick

Since, unfortunately our bath cryostat broke, a new probe stick had to be designed and built. With which we are able to measure in one of the bath cryostats of the institute's low temperature group. The design is rather simple, but versatile enough to house various resonator designs for many different measurements.

It consists of a head build of a KF-flange 40 – 50mm adapter, with a cap housing all the connectors, as seen in fig. 4.8a. A stainless steel pipe with a diameter of 28.6mm and 118 cm length is welded inside the adapter. The pipe has a small wall thickness of 0.2 mm, to reduce the heat transferred into the cryostat. At the bottom is a plastic sample holder, as depicted in fig. 4.8b, to allow measurements by varying

magnetic fields, simulating the environment in the science chamber. In the pipe are the cables to connect to two temperature sensors with 4-point measurement and two coaxial cables to apply MW signals to the resonator, with SMA-connectors on the top and SMP-connectors towards the sample holder. The 16 connections via two Oxford connectors, allow, apart from the temperature measurement, also six connections for miscellaneous purposes. To test actual atomchips with high trapping currents, two more wires with a thick cross section, supplying the chip wire, could be installed.

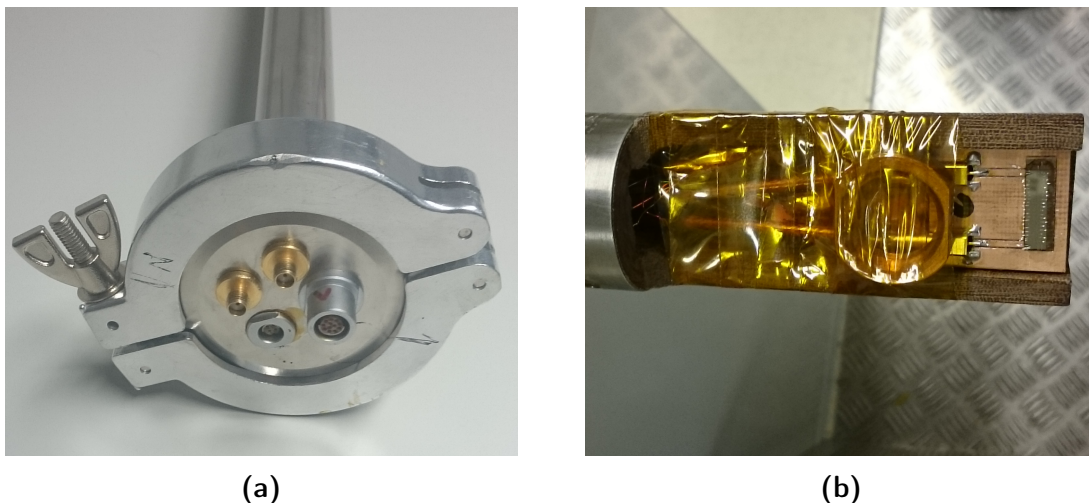


**Figure 4.8.:** (a) shows the top cap of the probe stick housing two Oxford connectors for temperature measurement and miscellaneous purposes. The two SMA coaxial connectors are there, to connect to a VNA and test the MW properties of our test chips. (b) depicts the sample holder at the lower tip of the probe stick, with a PCB holding a co-planar wave guide resonator connected with two SMP plugs.

### 4.3.2. Resonators

For our first series of test resonators, we have two different types. Lumped element resonators and co-planar wave guide (CPW) resonators. The latter is a simple transmission line, with two gaps acting as capacitors for capacitively coupling into the  $\frac{\lambda}{2}$  transmission line resonator. The other type is a classical LC-circuit, inductively or capacitively coupled to a feed line.

#### Co-Planar Wave Guide Resonator

This type of resonator is a simple transmission with  $\frac{\lambda}{2}$  length and a certain gap between the central conductor and the ground planes surrounding it. Two capacitors at the end

of the line, couple in and out of it. Figure 4.9a shows the corresponding schematic. The resonance frequency is simply defined by its length, taking into account the refracting index of the substrate material  $n$ . This is necessary since on such a transmission line with vacuum on top and sapphire below only "quasi-TEM" modes can propagate [81], leading to an effective wavelength

$$\lambda_{\text{eff}} = \frac{\lambda}{n_{\text{eff}}}, \quad (4.6)$$

where

$$n_{\text{eff}} = \frac{1 + n}{2} \quad (4.7)$$

is an effective refraction index. For our clock state with  $\frac{\lambda}{2} = 4.389$  mm and  $n_{\text{eff}} \approx 1.375$ , this calculates to a length of 3.192 mm. Figure 4.9b shows such a resonator glued onto a testing PCB with G-Varnish and aluminium bonds for contacting.

The field maximum is over the gaps between the inner conductor and ground plane, in the center of the resonator. The field also shows a strong gradient perpendicular to the chip surface. To use such a design on an atomchip, we would need to bring the atoms very close to the chip and probably bend the transmission line, since our current Z-wires on chips have a length of about 2 mm, which is about half the length of  $\frac{\lambda_{\text{eff}}}{2}$ . Furthermore, the ground plane surrounding the resonator would need to be reduced as much as possible, to allow the magnetic fields trapping the atoms to still permeate the chip. This would lead to a reduction of the quality factor  $Q$ , for which we have the high requirement of  $10^6$ .

### Lumped Element Resonator

The second type of resonator in our first designed test chips, is the lumped element resonator. As the name suggests it is made of discrete electrical components. So it consists of a dedicated capacitance  $C$  and inductance  $L$ , in series. They are capacitively coupled with  $C_{\text{in}}$  and  $C_{\text{out}}$  to two feed lines, as seen in fig. 4.10a. The option of two feed lines enables to measure the resonator in transmission and reflective mode, so the entire S-matrix can be measured. The resonance frequency calculates from the known formula

$$\nu_{\text{res}} = \frac{1}{2\pi\sqrt{LC}}. \quad (4.8)$$

The design as seen in fig. 4.10b is favourable for integrating onto an atomchip. Since the ground planes for the feed lines can be made rather small and the single loop acting as inductance  $L$  could be brought very close to the Z-wire. In addition, it has a small mode volume, allowing more homogeneous and stronger fields.

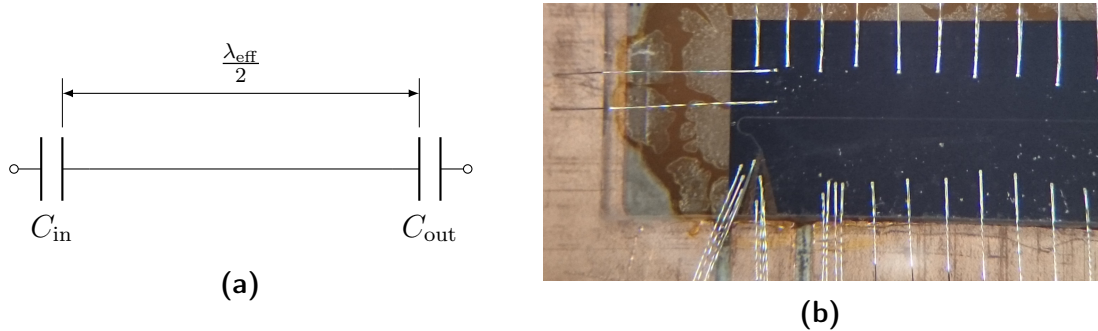


**Figure 4.9.:** (a) shows the simplified schematic of a transmission line resonator. Apart from the two coupling resonators, there are also not depicted inductances and capacities to the ground plane which we neglect. (b) depicts one of our test resonator chips already mounted on a PCB for testing on the probe stick. The actual transmission line starts from the contact pad of the circuit path at the bottom. It then makes a wiggle to the left, to have a greater range where to place the coupling capacitors and then goes straight to the right. The coupling capacitors are not visible with the naked eye. Aluminium bonds around the chip provide proper grounding of the ground plane.



**Figure 4.10.:** (a) is a simplified schematic of an lumped element resonator with two capacitors to couple to feed lines. (b) shows a lumped element resonator design, to test in our bath cryostat. To the lower left the contact pads for the central conductor and ground plane are seen. Right of the center is a current loop, creating the inductance  $L$ , while left to it between the two capacitively coupled feed lines is the capacitance  $C$ , which is made of an array of conductor paths arranged like interlocking fingers.

# 5. Novel Superconducting Chip Traps

As discussed in chapter 1, novel ideas which could be used as tool came up from the process of building and operating this experiment. By utilizing the superconducting properties of our atomchips, novel atom traps can be created. This chapter builds on the results of [2, 3] and shows how the atom cloud to chip distance can be programmed, utilizing our quench laser setup and the hysteresis behaviour of niobium. This programming allows to keep the chip trap parameters, chip current and Bias field, constant, while varying the atomchip to cloud distance. This effect even allows to form persistent current traps.

## 5.1. Current Distribution Modelling

Niobium is a type-I/II superconductor, which has apart from a pure MEISSNER phase, also a SHUBNIKOV phase, where a ABRIKOSOKOV lattice of vortices is formed [82]. This leads to a hysteresis behaviour, which leads via external fields or applied currents to a remanent magnetization. Microscopically, this is due to the pinning of the introduced vortices.

In contrast to the type-I superconductivity, which is explained by [7], there is no complete microscopic theory for type-II superconductors. Therefore, we can only describe our superconducting atomchip by the phenomenologically, macroscopic BEAN-critical-state model [83, 84]. This model is used to describe high temperature superconductivity with a vanishing  $H_{c1}$ .

The BEAN-critical-state model treats the vortices introduced through external fields and applied currents as macroscopic shielding currents. These currents clip the current density  $j$ , which depends on the magnetization, to the critical current density  $j_c$ , in the volume penetrated by vortices. For simplicity the dependency of the current density on the magnetization is neglected in this model, which is a good approximation for small external fields.



Our niobium film with a thickness of  $a = 1 \mu\text{m}$  and width  $w = 200 \mu\text{m}$ , easily satisfies the thin film condition  $w \gg a$ . Furthermore, in the chip trap, we apply a perpendicular bias field to the superconducting wire. Therefore, the BRANDT-model [85], which adapts the BEAN-model to superconducting strips in a perpendicular field, is used. Since, we are in the thin film regime we can approximate the density distribution in thin direction as constant. This leads to a current density, starting from the virgin state, of

$$j(y, I, I_c) = \begin{cases} \frac{2j_c}{\pi} \arctan \left( \left( \frac{(w/2)^2 - b^2}{b^2 - y^2} \right)^{\frac{1}{2}} \right) & |y| < b \\ j_c & b \leq |y| \leq \frac{w}{2} \end{cases} \quad (5.1)$$

for an applied current  $I$  at position  $y$  along the cross section. Here,

$$b = \frac{w}{2} \left( 1 - \left( \frac{I}{I_c} \right)^2 \right)^{\frac{1}{2}} \quad (5.2)$$

describes the area, where  $j(y)$  is governed by the MEISSNER-LONDON distribution and  $I_c = wdj_c$  is the critical current in our wire.

When previously a higher current  $I_{\max}$  was already applied, the hysteresis effect through the pinned vortices, leads to a different current distribution

$$j(y, I, I_{\max}, I_c) = j(y, I, I_c) - j(y, I_{\max} - I, 2I_c). \quad (5.3)$$

Figure 5.1 shows a current induced current distribution  $j(y, I, I_{\max})$  for an  $I_{\max}$  of nearly  $I_c$  being applied before. In the virgin state without a current history,  $j$  would clip to  $j_c$  for  $|y| < b$ . One can see that this effect changing the current distribution, lets effectively flow the current more in the center. As described in the next section, this can be utilized as a tool for superconducting atomchips.

Analogue the current distribution shows a hysteresis behaviour when external fields are applied,

$$j(y, H_{\text{ext}}, I_c) = \begin{cases} \frac{2j_c}{\pi} \arctan \left( \frac{w}{y} \left( \frac{(w/2)^2 - b^2}{b^2 - y^2} \right)^{\frac{1}{2}} \right) & |y| < b \\ \frac{j_c y}{|y|} & b \leq |y| \leq \frac{w}{2}, \end{cases} \quad (5.4)$$

with

$$b = \frac{w}{\cosh\left(\frac{H_{\text{ext}}}{H_c}\right)}. \quad (5.5)$$

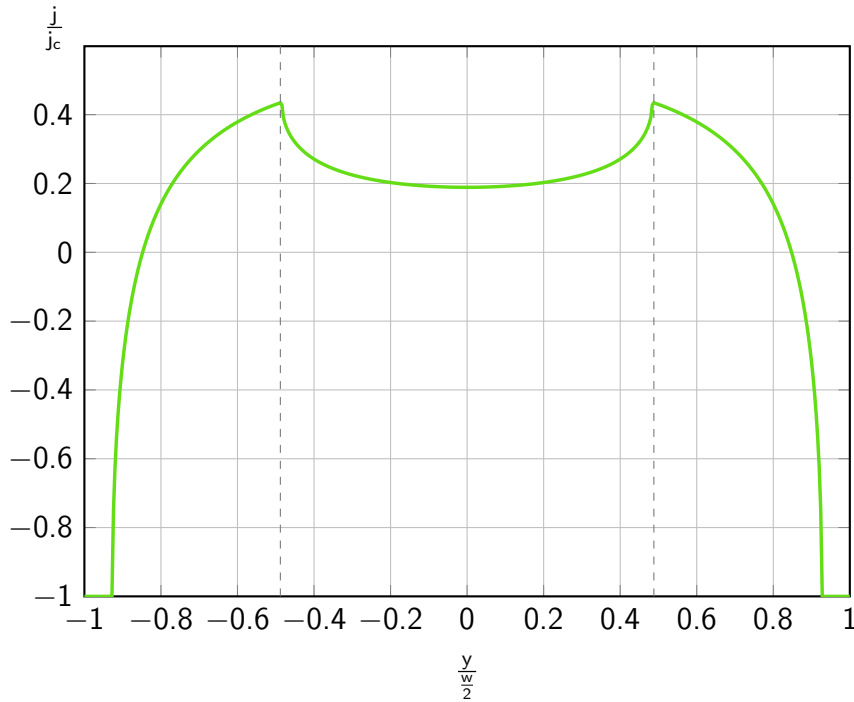


**Figure 5.1.:** Plot of the current distribution after previously applying  $I_{\max}$  being nearly  $I_c$ . The gray dashed line indicates the  $-b$  to  $b$  bound MEISSNER-LONDON distribution area.

Therefore, a current density with an external field history denotes to

$$j(y, H_{\text{ext}}, H_{\text{max}}, I_c) = j(y, H_{\text{ext}}, I_c) - j(y, H_{\text{max}} - H_{\text{ext}}, 2I_c). \quad (5.6)$$

## 5.2. Trap Distance Programming

The hysteresis effect described above for type-II superconductors, is observed either by applying a transport current leading to eq. (5.3) or applying external fields. With external fields an asymmetric current distribution forms according to eq. (5.6). Through applying series of external fields, novel traps can be formed through the persistent currents induces [86–90].

In contrast, current induced hysteretic current distributions are symmetric as seen in fig. 5.1. This makes this effect useful, to alter the current distribution in a superconducting atomchip by influencing the magnetic field of the chip wire and therefore controlling the cloud to chip distance. Figure 5.2 shows the experimental configuration.

The currents applied are seen in fig. 5.3. Before each  $I_{\max}$  current pulse was applied, the superconducting wire was quenched to its virgin state via our quench laser (see

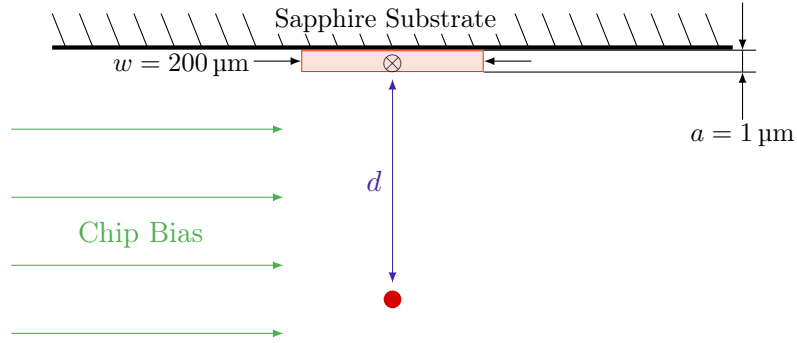


**Figure 5.2.:** Sketch of the chip on the sapphire chip mount, varying the atom cloud (red dot) to chip distance  $d$ , while keeping the chip bias field and chip current ( $\otimes$ ) constant.

section 3.1). The quench happens, while the atoms are still in the quic trap. Since the quench laser is far detuned  $\lambda = 1064 \text{ nm}$  to our rubidium transitions the laser passing through the atomic cloud is not a problem. The quench happens with a power of up to  $1 \text{ W}$  within a few milli seconds. We believe that the COOPER pairs are broken in the center of the chip and through an avalanche effect the entire Z-wire gets normal conducting. Once the laser is off, superconductivity is reached again within a few milliseconds. The process can be monitored by measuring the voltage over the chip for a small current applied. Through this, we can confirm a full quench without any measurable heating. The quench setup is explained in great detail in [59].

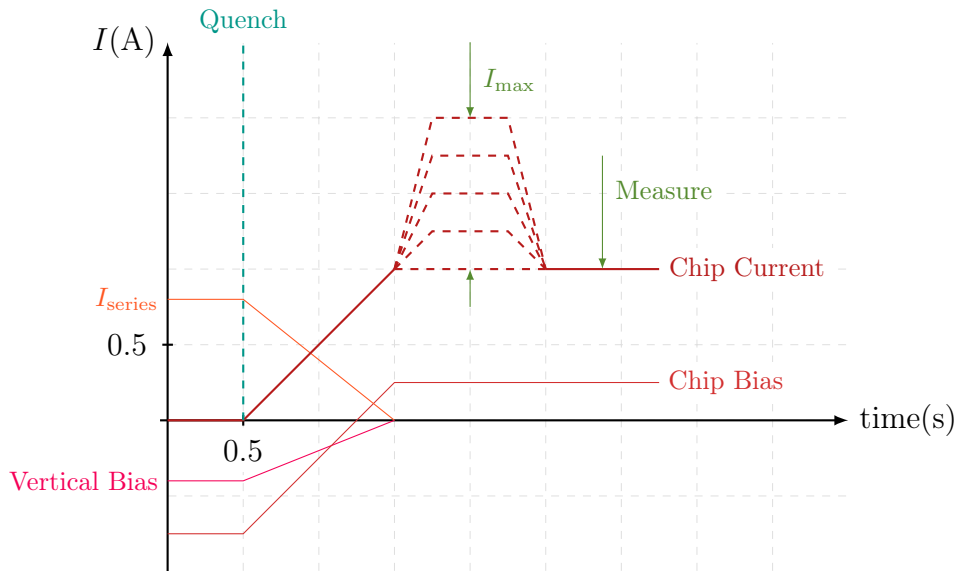


**Figure 5.3.:** Sketch of the current sequence used to measure the cloud distance to the chip, depending on the previously applied  $I_{\max}$ , after a quench of the superconducting film. For better readability, bias currents are not to scale.

Figure 5.4 shows a measurement with the current sequence from fig. 5.3, with varying  $I_{\max}$ , while a constant trapping current  $I = 1$  A and bias field of 10 G are applied. Each point has been measured 80 times, while 45 measurements had to be excluded, due to imaging errors. Although the deviation is quite big, the behaviour is well discernible. One clearly sees how the mean cloud distance  $d$  decreases with increased  $I_{\max}$ . This can be explained by the tailored current distribution, concentrating the current more in the center of the wire with increased  $I_{\max}$ . For large distances  $d \ll w$ , the atoms see the chip as a infinitely thin wire. But with the ratio  $\frac{d}{w}$  approaching one, this is not true any more and the atoms experience the magnetic field of a current in the middle of the wire and two equal counter propagating currents on the edges of the strip. In total, the trapping current is weaker and therefore, while keeping the bias field constant, the trap forms at a closer distance.

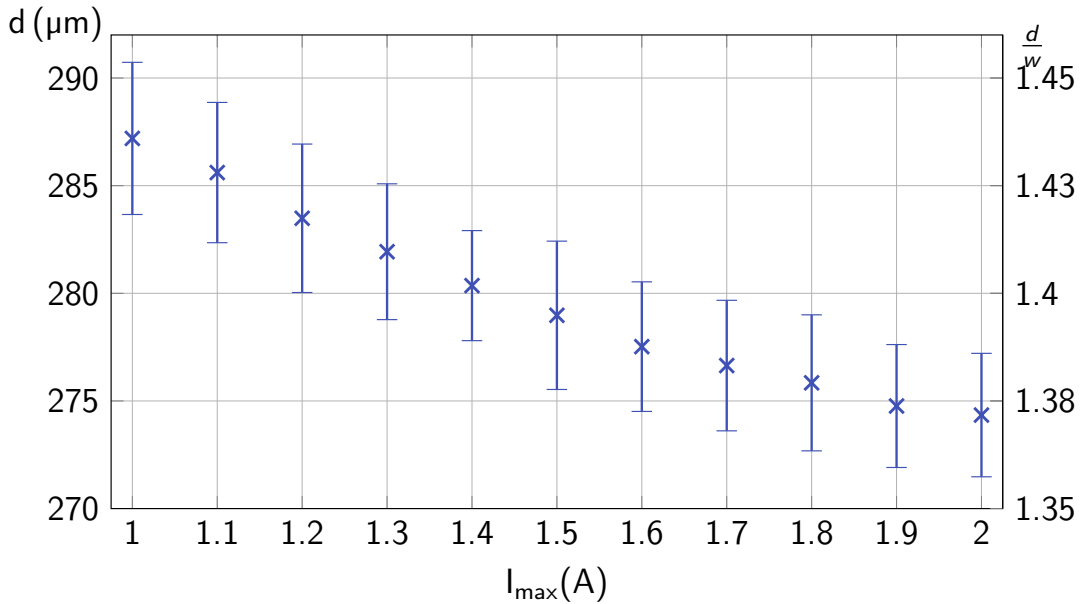


**Figure 5.4.:** Cloud distance to the chip with an applied  $I = 1$  A and bias field of 10 G, depending on the previously applied  $I_{\max}$ , after a quench of the superconducting film with width  $w = 200 \mu\text{m}$  (see fig. 5.3). For each plot point 80 samples were taken, while 45 individual measurements were neglected due to imaging errors.

Our setup is mostly constrained by the chip bounds and normal conducting wires in the  $T > 50$  K part of the cryostat. Although a niobium structure like our chip wire should have a fairly high  $I_c$ , we are limited to a maximum of about 3 A, where the chip either quenches due to the aluminium bonds or the normal conducting copper wires are at risk of melting. With a high  $I_c$  and sufficient low noise levels on the chip, this technique could be used to further lower the cloud distance  $d$  without altering the trap

current nor bias field. Further reducing  $d$  is one important task to increase coupling, working towards a hybrid quantum system as described in chapter 4.

### 5.3. Zero Transport Current Traps

A part from tailoring the current distribution to control the cloud distance  $d$ , we could also ramp the transport current down to zero after a an  $I_{\max}$  spike of close to  $I_c$  and load the atoms into a trap produced by the remanent magnetization. This technique could be employed to trap atoms on Z-wires without supplying it, thus reducing noise brought into the science chamber. The current distribution obtained in our chip with an  $I_{\max} = 1.9$  A is plotted in fig. 5.5.

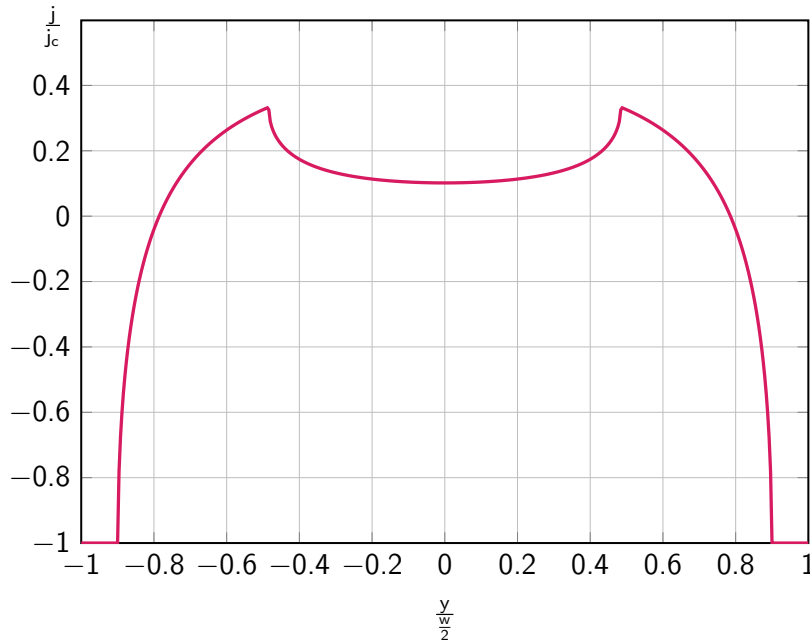


**Figure 5.5.:** Plot of the remanent current distribution at zero transport current, after previously applying  $I_{\max} = 1.9$  A. This persistent current could be used for novel, noise minimized traps.

Similarly, this can also be done with an external field and ideally a Z-wire without contact leads. This will, due to an asymmetric current distribution, create a trap shifted parallel to the central chip wire, along side with the current flowing in the direction creating a trap. This interesting scheme to trap atoms noise minimized, was investigated with our niobium chip in [91]. To avoid an asymmetric current distribution, a closed superconducting loop can be used, in which a persistent current is induced by an external magnetic field, as done in [92].

## 6. Atomic Recombination

Similar to the technique described in chapter 5, another idea to use the unique experiments setup is the possibility to recombine several atomic clouds, with the means of our magnetic conveyor belt, to create one larger ensemble.

As seen in fig. 3.13, the atom count in the cryostat is limited by the differential pressure stage, which could only be removed by a complete disassembly of the vacuum system. As a means of countering this problem, the approaches of further improving the MOT or initially trapping more atoms are futile since they get cut off at said bottleneck. In the wake of this, the idea of atomic recombination came up, which means running the MOT several times in one experimental cycle, transporting the atoms through the bottleneck as before and then combining these bunches to one bigger cloud of cold atoms. With the good lifetime of our atoms in the cryostat (see section 4.2.1) and a reduced MOT run time of e.g. 5 s, we anticipate an increase of atoms, in the final quadrupole trap between V8 and V9 inside the cryostat, by one order of magnitude.

Apart from improving the performance in this setup, this technique could also be used as a tool in all kind of cold atom experiments, to increase the number of atoms for statistic relevance of measurements and improve the ability for evaporative cooling. Furthermore, it would be a way to combine atoms of different species in one mixed cloud [93].

Since, the cryostat already required the magnetic conveyor belt with a corner, no physical changes are required to implement this atomic recombination scheme. However, the control software is unable to manage the currents in the way, needed for such a task. The Matlab control program was implemented a long time ago in a entirely non-flexible way. The initially simple idea required quite some technical effort, since the entire control software had to be replaced and therefore the entire experimental cycle and transport currents had to be recalculated and redesigned as well.

## 6.1. Transport currents

In order to transport atoms with minimal atom count loss and heating, the trap geometry should stay the same. The trap minimum has to experience a smooth trajectory and the field gradient has to be big enough to sufficiently trap the atoms without spilling them. This is achieved by a good alignment of the transport coils and a current sequence that generates a quadruple trap, with a set gradient in  $z$  direction of

$$\frac{\partial |\mathbf{B}|}{\partial z} = 130 \text{ G cm}^{-1}, \quad (6.1)$$

moving along the transport axis. This is formulated into conditions which are then plugged into a equation system, solved with Mathematica, yielding the current sequences necessary.

### 6.1.1. Aspect Ratio

To keep the trap geometry the same and avoid breathing modes etc. in the atomic cloud, the aspect ratio

$$A = \frac{\frac{\partial B_y}{\partial y}}{\frac{\partial B_x}{\partial x}}, \quad (6.2)$$

should stay constant. As seen from above  $A$  describes the symmetry of the magnetic field. In a quadrupole configuration,  $A$  is one due to the symmetry around the vertical axis, but during the transport, there are always at least 2 coil pairs active. When shifting from one coil pair to the next, the trap would elongate and shrink to a sphere again, resulting in a oscillating  $A$ , shaking the atoms. To solve this issue, at least 3 coil pairs are active, as discussed in [63].  $A$  is chosen empirically to  $A_{\text{trans}} \approx 1.715$ . This aspect ratio enables a transport with only unipolar currents in 3 coils at a time in our setup. To gap the difference between the simple quadruple trap in the MOT phase with  $A = 1$  and the transport phase with  $A_{\text{trans}} = 1.715$ , a smooth transition, as seen on the left side of fig. 6.1, is employed. This transition is arbitrary set to:

$$A(x) = \begin{cases} 1.25 + (-0.017 + x)(14.8 + x(865 + 50885x)) & 0 \leq x \leq 0.017 \\ 1.715 + (-878 + 6975(-0.017 + x))(-0.04 + x)^2 & 0.017 < x < 0.04 \\ A_{\text{trans}} & 0.04 \leq x. \end{cases} \quad (6.3)$$

At the end of the horizontal part again only 2 coil pairs are active H4 and V1, V2 realizing a simple quadruple trap, which is the starting point for vertical transport. Unfortunately, there is no additional coil as the PUSH coil at the beginning of the

transport, present, to realize a smooth change of  $A$ . Therefore, the constrain of a constant  $A$  is repealed at 170.9 mm, where H3 starts to ramp down. This results in a rapid change of  $A$  towards the end of the of the horizontal part, as seen in fig. 6.1. This oscillating transition back into a spherical trap at the end of the horizontal transport is certainly not ideal and should be avoided to reduce the stress on the transported cloud. Installing an additional coil, would allow a smooth transition into a spherical trap for the vertical part as well.

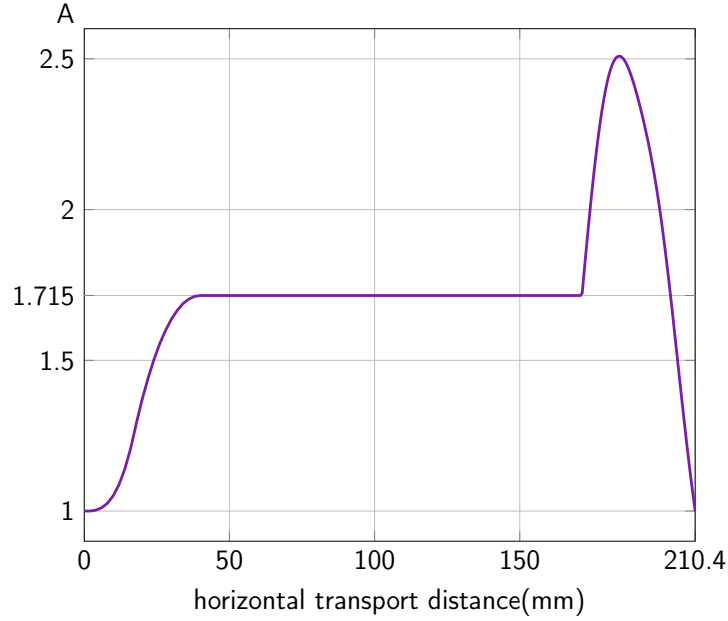


**Figure 6.1.:** During the horizontal transport, the aspect ratio  $A$  changes, from one of a spherical trap in AH configuration to the set value 1.715, by eq. (6.3). This allows a smoother transport with a more stable trap. Towards the end of the horizontal part the trap geometry changes again, since at the end it is an AH configuration as well. Due to a lack of a further coil like the Push coil in the beginning of the horizontal part, to counteract a rapid change of  $A$ , this transition happens in a rapid, uncontrolled way.

### 6.1.2. Calculation

The new calculation for the current sequence was done in [94]. In this thesis to simulate the coils, each is divided in  $N$  single, circular current loops spaced in a regular grid mimicking the actual windings of each coil, where  $N$  is the respective winding number.



The magnetic field for each loop is then calculated by the analytic expression from [95].

$$B_x = \frac{\mu_0 I x z}{2\pi\alpha^2\beta\rho^2} [(a^2 + r^2) E(k^2) - \alpha^2 K(k^2)] \quad (6.4)$$

$$B_y = \frac{\mu_0 I y z}{2\pi\alpha^2\beta\rho^2} [(a^2 + r^2) E(k^2) - \alpha^2 K(k^2)] \quad (6.5)$$

$$B_z = \frac{\mu_0 I}{2\pi\alpha^2\beta} [(a^2 - r^2) E(k^2) + \alpha^2 K(k^2)], \quad (6.6)$$

with

$$\begin{aligned} \alpha^2 &= a^2 + r^2 - 2a\rho & \beta^2 &= a^2 + r^2 + 2a\rho \\ \rho^2 &= x^2 + y^2 & r = z^2 &= \rho^2 & k^2 &= 1 - \frac{\alpha^2}{\beta^2} \end{aligned}$$

and  $E(k^2)$ ,  $K(k^2)$  elliptical integrals of the first and second type.

The loops are then summed up to obtain the field of each coil.

### 6.1.3. Horizontal Section

To achieve a sufficient horizontal transport the constraints mentioned in section 6.1 for to the horizontal part yield following conditions:

- The trapping gradient is set to a sufficient value (see eq. (6.1)).
- The magnetic field is 0 at the trap minimum  $|\mathbf{B}(\mathbf{r}_{\text{trap}})| = 0$ .
- The geometry has to stay constant i.e.  $A = 1.715$ .

To get the actual currents the above conditions are applied to the expressions from eq. (6.4) resulting in an equation system, which is solved with Mathematica. The resulting solutions were then manually edited to exclude unphysical solutions and obtain smooth curves. The resulting current sequences are shown in fig. 6.2. H5 is the last coil pair of the horizontal part, which is actually V1 and V2 the first coils of the vertical part.

### 6.1.4. Vertical Section

For the vertical transport section, slightly different conditions are necessary. To transport atoms vertically through coils, it is necessary to have at least 4 coils active at each time, since eventually each coil has to switch polarity when the atom cloud

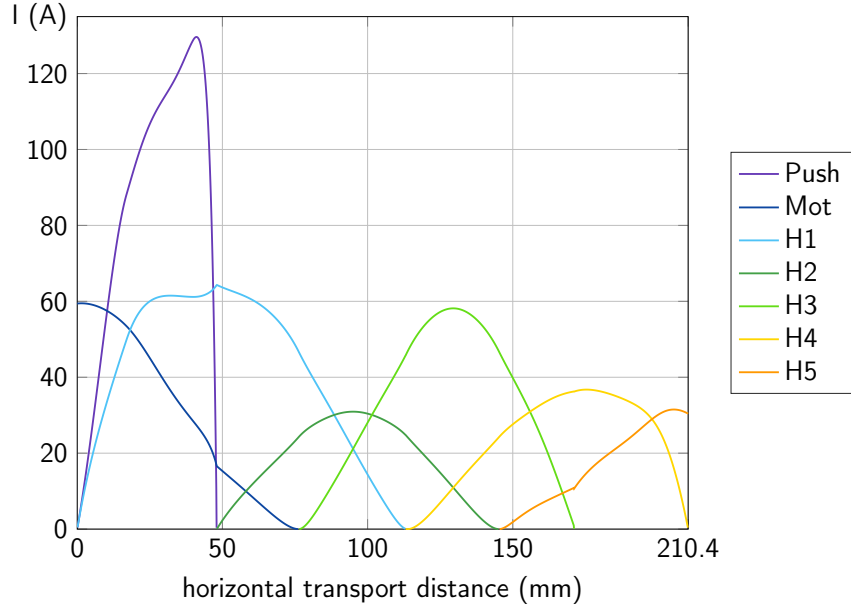


**Figure 6.2.:** Current sequence for the horizontal transport: The Push coil in the beginning oriented in transport direction unlike the others, prevents the trap from opening in one side and helps to smoothly change  $A$  from 1 to 1.1715.

passes right through it, as seen in fig. 6.9. Furthermore, the aspect ratio is here, as defined above, not of any meaning, due to the symmetry around the  $z$ -axis, which is also the transport direction. The changes conditions for the vertical part are:

- The trapping gradient is set to the same sufficient value (see eq. (6.1)).
- The magnetic field is 0 at the trap minimum  $|\mathbf{B}(\mathbf{r}_{\text{trap}})| = 0$ .
- The gradient should be maximal at the trap position, therefore  $\frac{\partial^2 B_z}{\partial z^2} = 0$ .

Analogous to the horizontal part, these conditions applied to the expressions for the magnetic field from eq. (6.4), produce equations leading to the desired current sequence. The third condition leads to discontinuities, which are manually fixed through interpolation. The final sequence for the vertical transport section is plotted in fig. 6.3.

### 6.1.5. Coil to Current Source Transducer

As mentioned in section 3.4, for synergy just 5 high current sources<sup>1</sup> are used for the 16 NC transport coils, each supplying at least 2 coils. The SC coils need to be bipolar and there are no switch boxes as for V1 to V5. Therefore, an additional 7 ultra stable

<sup>1</sup>Delta-Elektronika, see also [www.delta-elektronika.nl](http://www.delta-elektronika.nl)

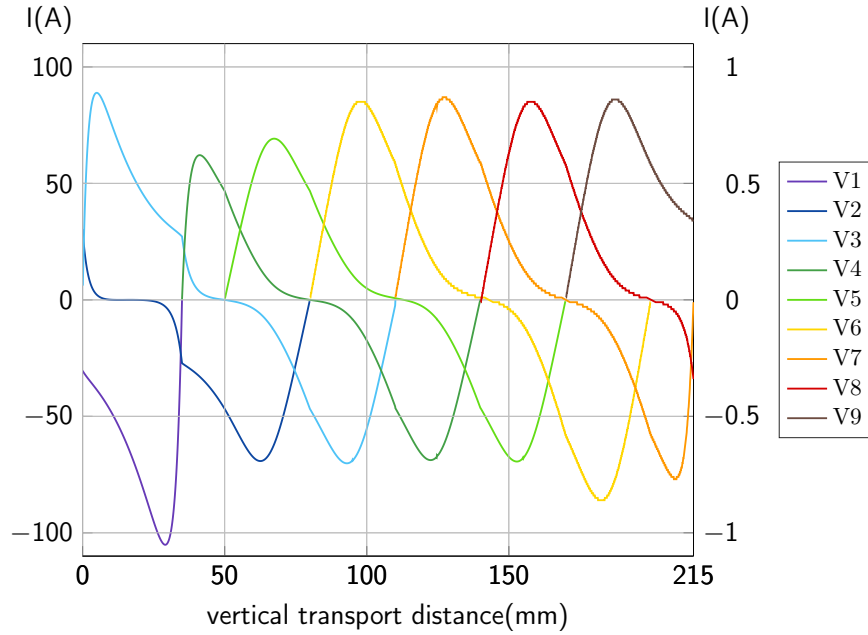


**Figure 6.3.:** Transport currents sequence for the vertical section. In x is the position of the trap and in y the necessary currents to produce such a trap plotted. The green and blue curves, V1 to V5 are NC coils with high currents (left axis). V6 to V9 are SC coils with small currents (right axis), but a lot more windings.

current sources<sup>1</sup>, for the 4 SC transport coils in each polarity, are required. These, have each a dedicated switch to separate the coil from the supply when not active, to prevent noise coupling into the cryostat from an idle current source. An overview of them is found in table 6.1.

To de-multiplex the NC coils' power supplies, switch boxes, which route the current from each power supply to two coils, are introduced. Each controls a bipolar and unipolar coil. The second switch box connected to Delta 2 is an exception, by having two simple switches and therefore being able to control two unipolar coils. These boxes are described in greater detail in [96]. Additionally the MOT coil pair has a dedicated switch,<sup>2</sup> suitable for fast switches, which is necessary in the optical pump and molasses phase. To control these switch boxes, two or three 5 V, TTL-signals are required. Table 6.2 shows the respective truth tables, denoting which state corresponds to which digital input configuration.

With the means of an Excel spreadsheet, the calculated currents fig. 6.2 and fig. 6.3 are de-multiplexed to the 5 high power current supplies for the horizontal and lower vertical part and the 7 Heidelberg current sources for bi-polar currents in the 4 SC

<sup>1</sup>in Heidelberg designed and at Atominstiut built, low noise current source

<sup>2</sup>TTL controlled 60 A switch build in Heidelberg

## 6. Atomic Recombination

Power Supply	Type	Current range (A)	Switch	Coils
Delta 1	SM 15-200D	0-200	switch box 1	Push, V1
Delta 2	SM 30-100D	0-100	switch box 2	MOT, H4, V4
Delta 3	SM 30-100D	0-100	switch box 3	H1, V2
Delta 4	SM 15-200D	0-200	switch box 4	H2, V3
Delta 5	SM 30-100	0-100	switch box 5	H3, V5
V6a	N142	0-2	V6a switch	V6a
V6b	N142	0-2	V6b switch	V6b
V7a	N142	0-2	V7a switch	V7a
V7b	N142	0-2	V7b switch	V7b
V8a	N142	0-2	V8a switch	V8a
V8b	N142	0-2	V8b switch	V8b
V9	N142	0-2	V9 switch	V9

**Table 6.1.:** Correspondence of coils, switches and current sources. The high power current source always supply several coils via a switch box, while each low current supply for the SC coils has its own dedicated switch.

coils in the upper vertical part.

This transducer process takes two parameters for each coil, a factor and the number of significant digits for the new in current sources decoded current matrix. The mentioned coil coefficient just multiplies all current values of a coil with the given factor. This feature has proved vital in debugging the newly calculated currents, e.g. H4 was off by a factor of 1.4. As an additional option the truth table of each switch box can be changed for faster debugging and easy re-configurability.

Analogously, another spreadsheet, de-multiplexes the spatial points, where the polarity of a coil is switched, when it goes to zero or starts to be active. These switch points require the state of a digital channel to be changed. In this spread sheet, the switch points can also be manually adapted, as required in the debugging process.

For recombination, these two files need to be adapted according to the recombination scheme. However, the recombination can also be done directly via the Experimental Controller by loading an external file or setting manual functions.

Switch Box 1		
	D11	D12
Push	1	0
V1	0	1

(a)

Switch Box 2				Mot switch
	D13	D15	D29	D10
MOT	1	0	0	1
H4	0	0	1	0
V4+	0	1	0	0
V4-	1	1	0	0

(b)

Switch Box 3		
	D16	D17
H1	1	0
V2+	0	1
V2-	1	1

(c)

Switch Box 4		
	D18	D19
H2	1	0
V3+	0	1
V3-	1	1

(d)

Switch Box 5		
	D20	D21
H3	1	0
V5+	0	1
V5-	1	1

(e)

**Table 6.2.:** Truth tables for the switch boxes. In (a) the H-bridge is not utilized since the current in V1 can only have one direction, while (b) controls with the MOT an additional unipolar coil and therefore needs an additional digital input. D10 needs also to be switched to enable the MOT, it controls a dedicated electronic switch for the MOT coils to enable a fast switch during the pump and molasses phase. (c) - (e) are standard switch boxes with one H-bridge and a simple switch for an unipolar coil.

## 6.2. Magnetic Transport Calculator

The resulting current sequences from above are in the spatial domain i.e. we know which coil needs how much current, to create the trap at a certain position. However, controlling the experiment needs obviously a time dependent current sequence, so the controller can regulate each current supply to the necessary value at each time step of the experimental cycle. For this, the variable transformation

$$\mathbf{I}(x) \rightarrow \mathbf{I}(t) = \mathbf{I}(s(t)), \quad (6.7)$$

where  $\mathbf{I}$  is the current vector containing the current for each coil and the chip as function of each time step  $t$  or space deviation  $x$ , is applied.  $s(t)$  is the trajectory calculated from the freely chosen acceleration profile. The Magnetic Transport Calculator was programmed for this main task. An excerpt of the source code's most important parts, is found in appendix A.

An overview of the program is given in the flowchart in fig. 6.4. First, all the necessary parameters are read from either a file or an user input dialog. Then, the polynomials for the horizontal and vertical part are initialized. Afterwards, the actual

transformation is done. While looping over the current matrix, the program transforms the switch matrix into the time domain as well. In the experimental, cycle the data files will be interpolated by the new control software (see section 3.8.2). Since each current sequence consist vastly of zeros, which would make the interpolation slow and inefficient, in another step, the data is cleaned of redundant entries. After this considerable reduction of the data set, it is written into data files for the experimental control software (see section 3.8.2).

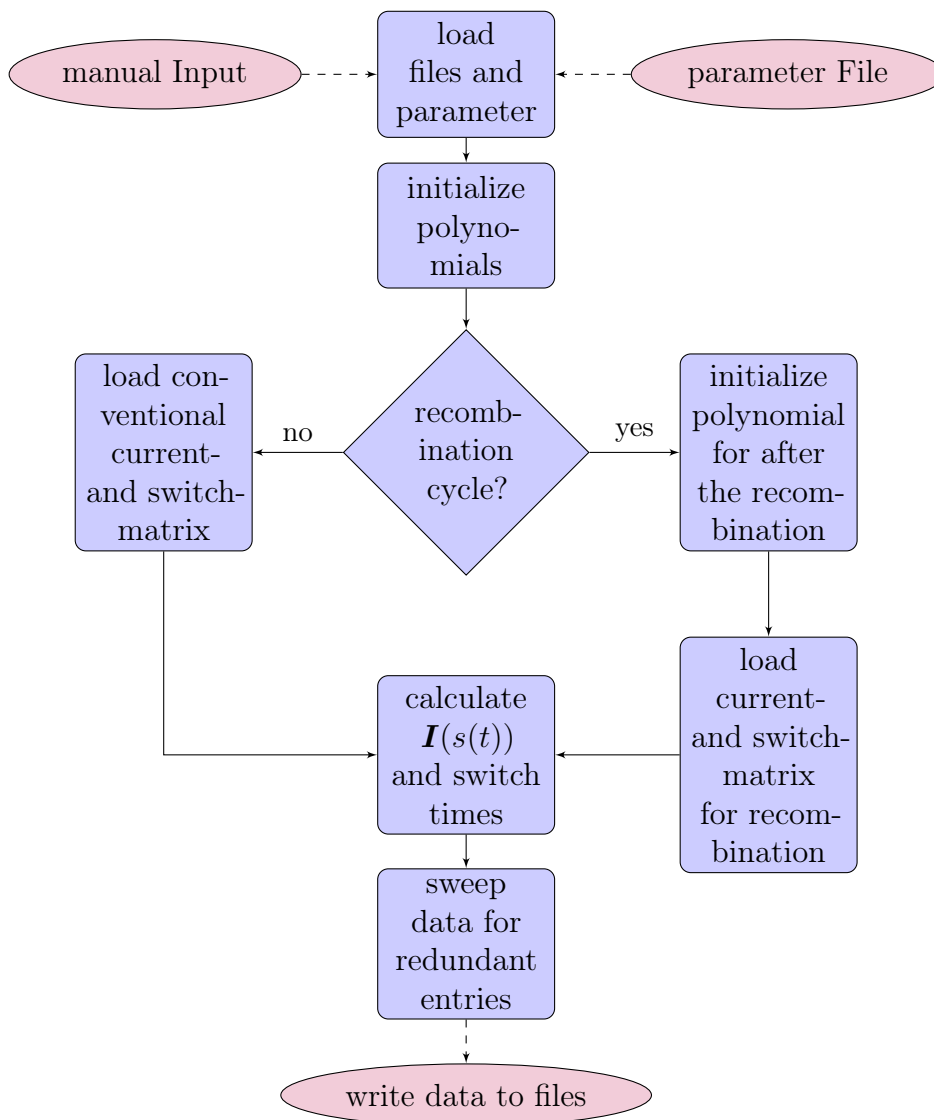


**Figure 6.4.:** Magnetic Transport Calculator flowchart

The calculator is implemented in a very flexible way. This makes it easy to adapt or reconfigure the system, as well as use it for similar magnetic conveyor belts. Apart

## 6. Atomic Recombination

---

of the current matrix and switch point matrix as input, the calculator needs a bunch of other parameters to create the trajectory and do the actual transformation. A complete list is found in table 6.3.

parameter	description	default value
userInput	input from file or as dialog in program	0
recomb	decide if recombination is done or not	0
timeStep	time increment for the calculation	50 ms
traveldistance[0]	hor. transport distance	210.4 mm
traveldistance[1]	vert. transport distance	215 mm
traveldistance[2]	vert. transport distance after recombination	30 mm
tHorizontal	time for the hor. transport	600 ms
tHorizontalVmax	acceleration time of the hor. transport	100 ms
aMax1	$a_{\max}$ of vert. transport before recombination	$3.8 \text{ m s}^{-2}$
vConst1	$v_{\max}$ of vert. transport before recombination	$0.15 \text{ m s}^{-1}$
tRecomb	duration of recombination process	500 ms
aMax2	$a_{\max}$ of vert. transport after recombination	$3.8 \text{ m s}^{-2}$
vConst2	$v_{\max}$ of vert. transport after recombination	$0.15 \text{ m s}^{-1}$

**Table 6.3.:** List of the Parameters the Magnetic Transport Calculator has. They can either be set in a parameter file or given in an user dialog.

With these parameters, the acceleration and, hence, the velocity of the atoms, is defined by a set of polynomials, mimicking the already established transport scheme. These polynomial are created by the class "Poly.h", as programmed in appendix A.3. It is designed in a rather general way to work as a basis for various transportation schemes. To create a polynomial, the constructor needs a pointer to a coefficient array, a name for it and the polynomial order. Furthermore, an offset for the variable and a flag for reverse can be set. These last two parameters enable to put several polynomials piece wise together and even use the same polynomial mirrored to create troughs as used for the acceleration and seen in fig. 6.6a. In fig. 6.5a and fig. 6.6a, these sections are indicated by the gray dashed lines. This gives the possibility to apply any kind of acceleration profile for the transport. The recombination on the other hand is currently manually coded into the recombination current matrix, which replaces then the one for conventional transport. This was done, to first try the simplest approach, as described in section 6.3.

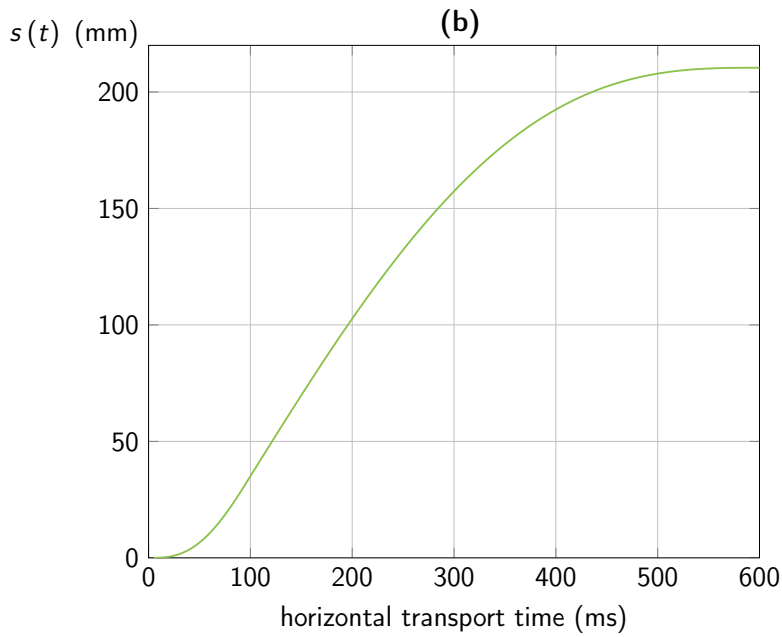
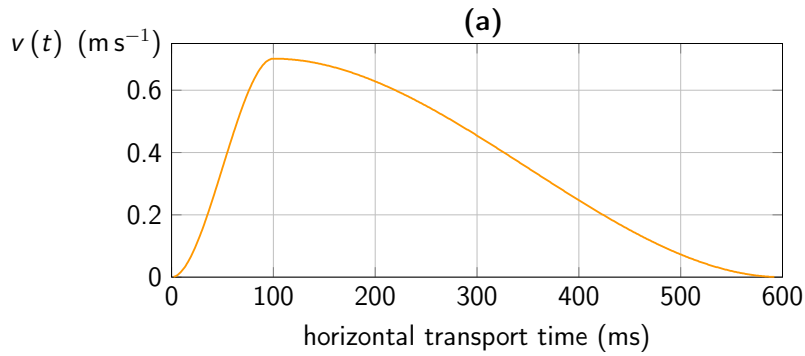
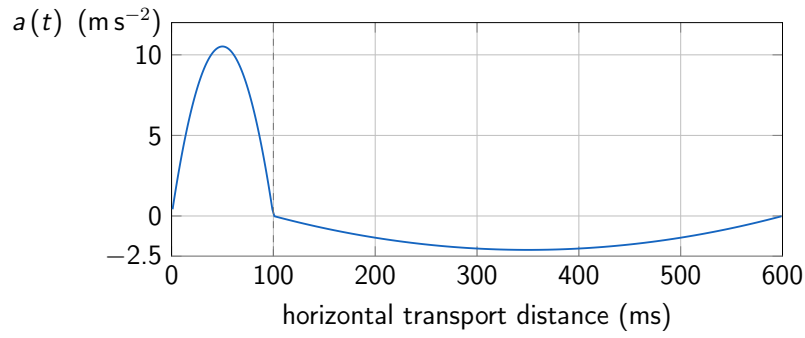
### 6.2.1. Temporal Behavior of transport

As described earlier, the trajectory of the atom cloud is set by piece wise joint polynomials for the acceleration. By integration  $s(t)$  depending on the parameters for the acceleration profile is calculated. These curves are plotted in fig. 6.5 for the horizontal part and fig. 6.6 for the vertical part. When recombination is done, the last 30 mm of the vertical part after the recombination, are done in the same manner as the lower vertical part. These trajectories are based on the ones already implemented in the old control software, which empirically proved to be good to transport atoms into the cryostat. However, due to the flexibility of the Magnetic Transport Calculator, it would be interesting to test other schemes to potentially increase the transport efficiency (see fig. 3.13) or reduce the transport time.



## 6. Atomic Recombination

---



(c)

**Figure 6.5.:** The acceleration for the horizontal transport, is given by two parabolas, a short one to accelerate and a longer one to decelerate. As a parameter, the length of the parabolas can be changed. This scheme tries to minimize the time around the small diameter differential pumping stage (see section 3.4). By simple integration, the velocity  $v(t)$  and trajectory  $s(t)$  are obtained.

## 6. Atomic Recombination

---

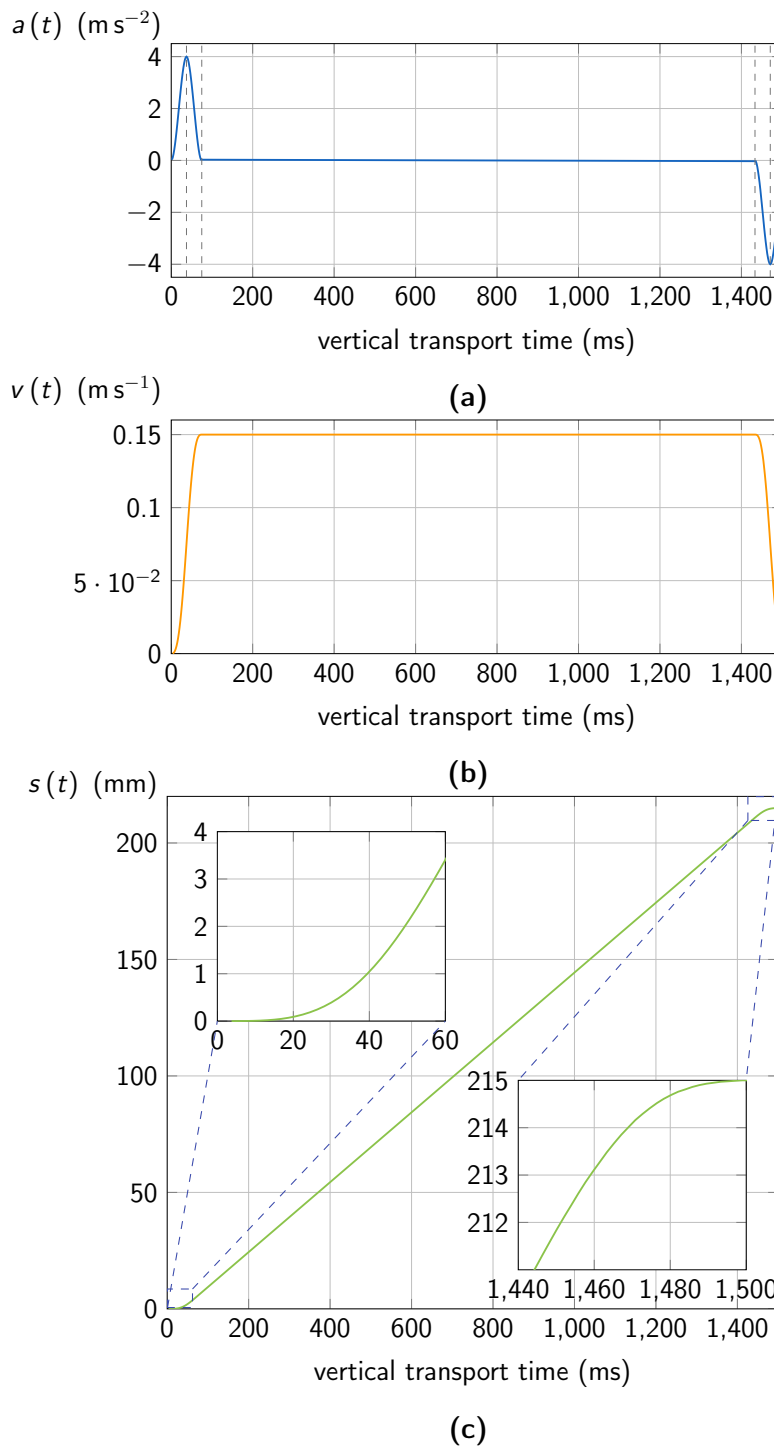


**Figure 6.6.:** For the vertical transport dynamics, the acceleration is empirically given by a short sixth order polynomial accelerating period, followed by a constant velocity and then, the previous acceleration period mirrored, deceleration phase at the end. Simple integration yields the velocity  $v(t)$  and trajectory  $s(t)$ .

### 6.2.2. Resulting Currents

Calculating the transformation, as described in section 6.2, yields the current sequences necessary for magnetic transport. They are plotted for the normal conducting coils in fig. 6.8 and those for the superconducting coils, are shown in fig. 6.7.

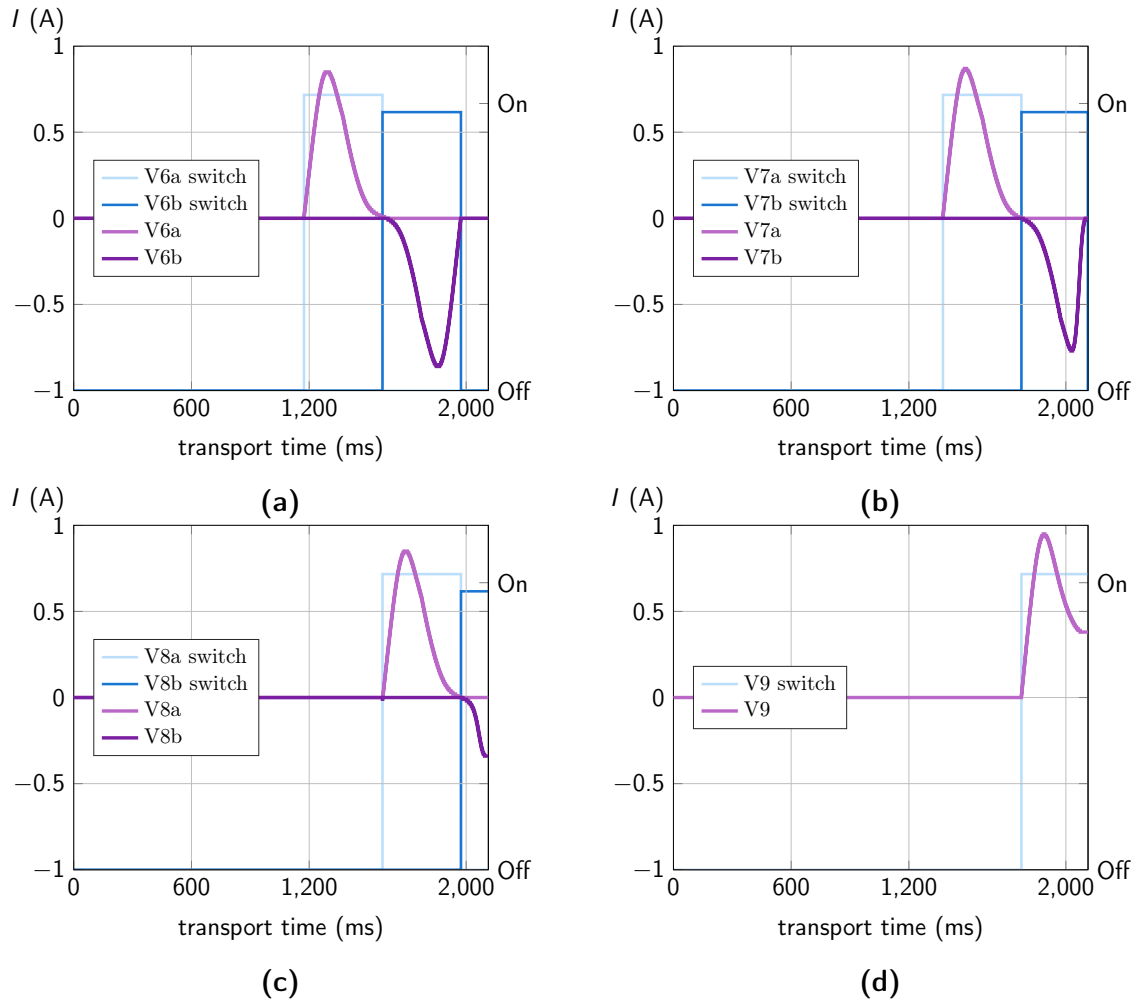


**Figure 6.7.:** Time resolved SC transport current sequences for each coil. (a) V6; (b) V7; (c) V8; (d) V9; The digital channels for the switches are 5 V TTL signals. For better readability their heights has been slightly altered.

## 6. Atomic Recombination

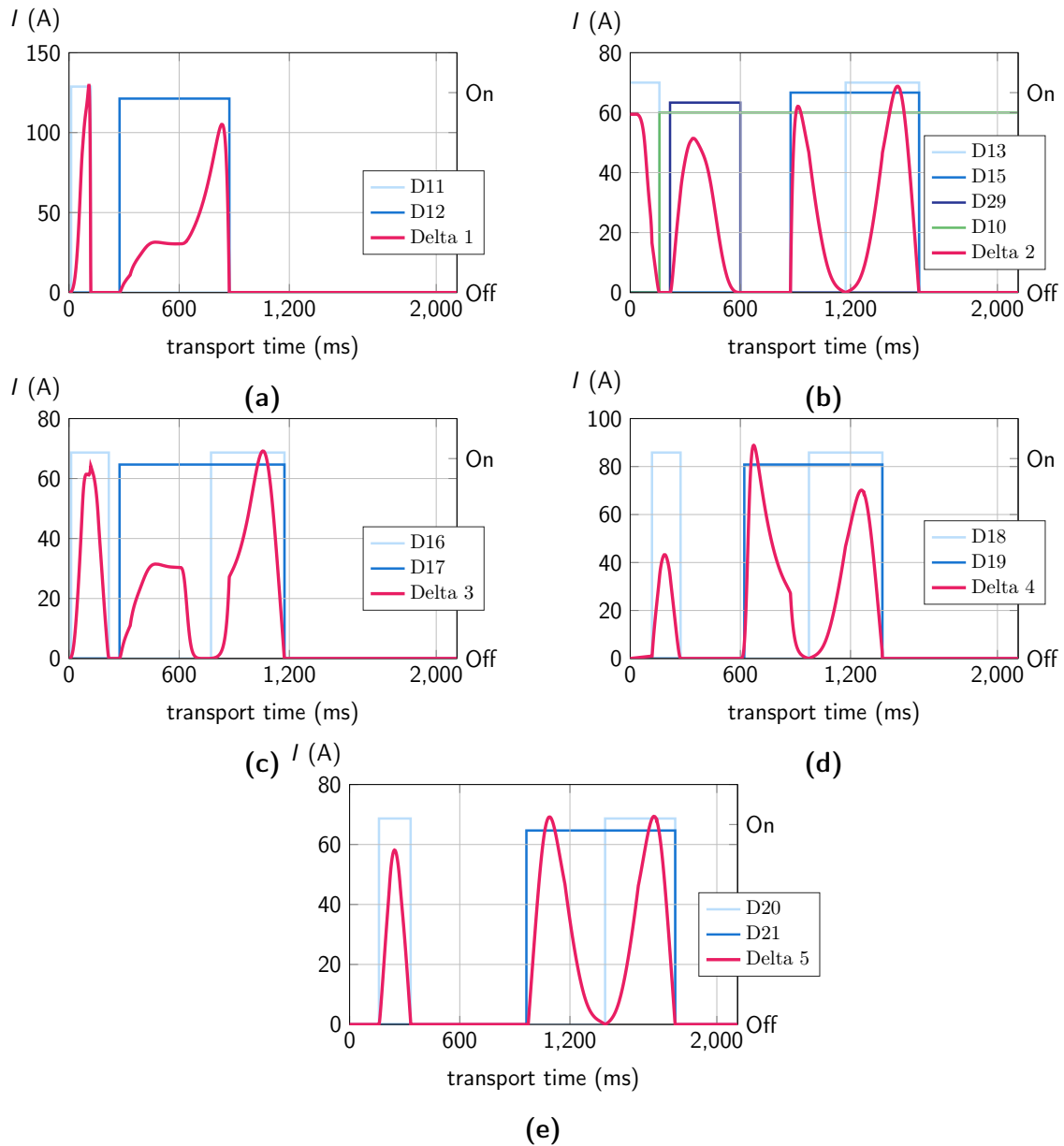


**Figure 6.8.:** Temporally resolved NC transport currents sequences for each power supply. (a) shows Delta 1, where the first spike is the push coil and the second one V1. (b) depicts Delta 2, with the first spike being the MOT coil still on from the pump phase and its additional inverted MOT switch for rapid switch off. The second spike is H4 and the last two are the two polarities of V4. (c) pictures Delta 3 supplying H1 fist and then V2+ and V2-. (d) shows Delta 4 responsible for H2 and V3. (e) is Delta 5 supplying H3 and the last NC coil V5. The digital channels have been slightly altered in height to better discern them. They are all 5 V TTL signals.

### 6.3. Attempted Recombination Scheme

To merge two atom clouds, we would first transport atoms all the way up to the upper yellow blob between V8 and V9 in fig. 6.9. There, they are stored while a new MOT (red blob in fig. 6.9) would be loaded. Once the second cloud is cold, it would be transported up to 155 mm, which corresponds to the lower yellow blob in fig. 6.9. This configuration is now the starting point of the actual recombination.

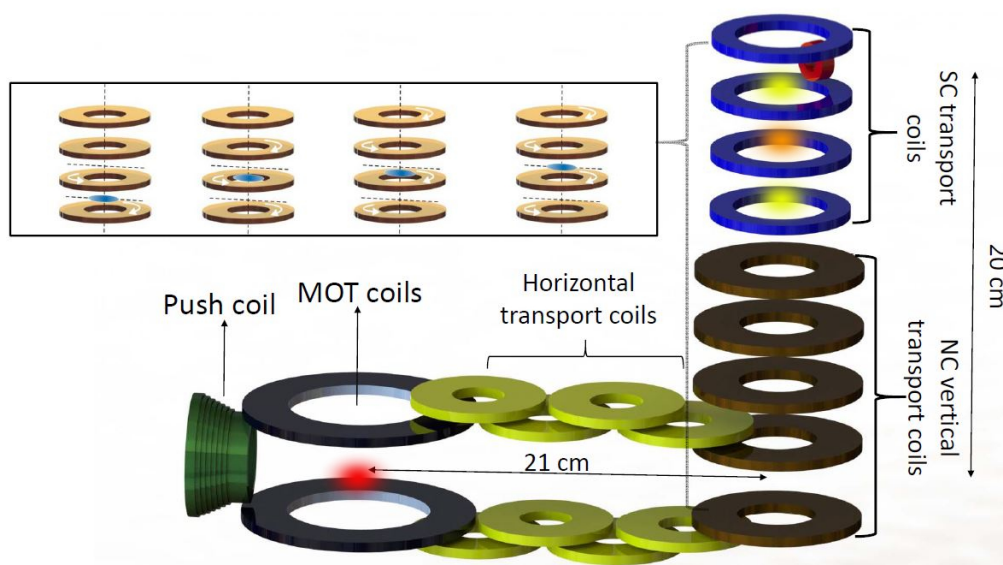


**Figure 6.9.:** Atomic recombination with magnetic conveyor belt: The big black coils are the MOT coils, while the brown and yellow ones are the vertical and horizontal part of the magnetic conveyor belt. The blue superconducting coils in the top part of the vertical transport are already inside the cryostat. The inset on the left shows how several coils have to be active to smoothly transport the atoms vertically upwards.

The simplest approach to recombine our two quadrupole traps stacked atop of each other, is to do linear ramps to form one combined quadruple trap in the middle, as shown in fig. 6.10. This was actually tested in the experiment, but failed, since no atoms were left after the process. These ramps were done rather slow in an arbitrary time frame of 500 ms, to ensure adiabaticity. Unfortunately, this approach does not work and all atoms are lost. Several variations with two linear ramps and unsymmetrical current ratios, between the upper and lower coils, were tried as well. With the result to be able to transport the atoms from the lower trap up, because the trap is deformed by gravity or alternatively. Or with the currents in favor of the upper trap, between V9 and V8, be able to load the upper cloud down into the lower trap. A combination where both traps could symmetrically merge in the center was not possible with this adiabatic time scales.

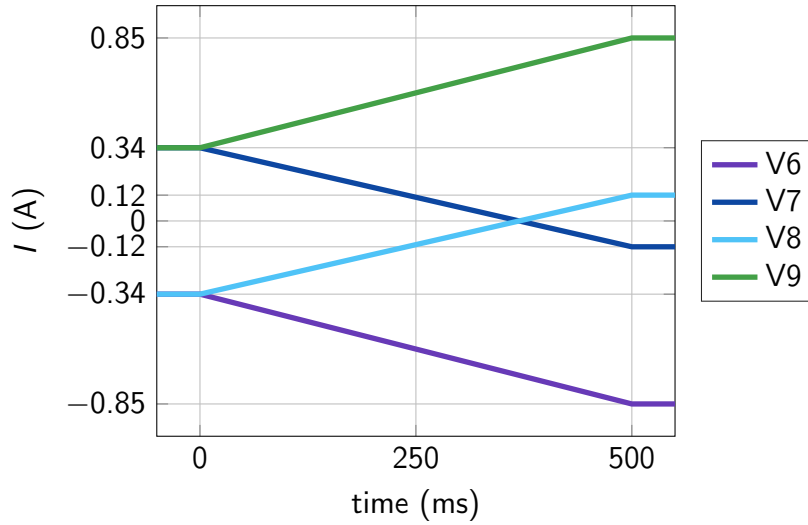


**Figure 6.10.:** Simple adiabatic current sequence attempt for recombination.

The problem is that during such merging schemes, the atoms are not trapped for a brief period of time. The traps with the increased current just survive on cost of the other one by reducing the time the trap, with increased current is open. As simulations showed [50], the necessary polarity change of the coils, between the two traps to combine, prohibits simple, adiabatic, linear current ramp approaches to merge.

However, using additional coils or dynamic current sequences, a merge with minimal heating and atom loss should be achievable in the cryostat. Since, the atoms are already laser cooled to several hundred  $\mu\text{K}$ , their velocity is small enough to not lose them if they are un-trapped only for a short period of time. Here, it is important to account for gravity, effectively deforming the magnetic field, as described in section 2.3. At these low temperatures, a fall of the atoms into the trap could significantly heat them. To solve this, experimental optimization methods like optimal control could also be employed.

# 7. Outlook

During the course of this thesis, several improvements have been made, as well many processes and aspects have been better understood. Although, the experimental stability has increased a lot through this, the main limitation for experimental progress remained the complexity and instability of the setup. This sensitivity of the experiment is due to the general nature of cold atom experiments as well as the particular complexity of this setup (e.g. 39 coils). Defined Benchmarks done, each day before starting any measurement or setup changes, were introduced. These Benchmarks helped to monitor the experiment and clearly support the previous statement.

The setup already reaches impressive experimental parameters, such as the extremely long lifetime of the atoms in the cryostat of about 200 s or the well optimized 3D MOT with up to  $3 \times 10^9$  atoms. Furthermore interesting novel tools were found, with possible applications in this and similar experiments. To fully employ these assets external influences, instable laser units and problems with electronics have to be further reduced and the monitoring capabilities should be expanded. This will let the experiment fully show its strengths like versatility and fast re-configurability, which will significantly accelerate the scientific output.

## 7.1. Hybrid Quantum System

The initial idea of this experiment to create a hybrid quantum system by coupling a recurring cloud of ultra cold atoms to a superconducting microwave resonator, is still the main goal of this setup. However, as showed in this thesis, this experiment has a lot of other prospects. Since the start of this project it became very clear, that in order to progress towards such a hybrid quantum system, one needs to look into how superconductors function and influence trapped atoms, instead of treating them as plain conductors with zero resistance.

A BEC has the advantage of being very cold and small in size, which also supports the assumption made, that in the proposed hybrid quantum system the MW field would be spatially constant. Nonetheless, evaporative cooling decreases the atom count by orders of magnitude. Therefore, the proposed  $10^6$  atoms will be difficult to achieve in a

BEC. Considering this one might also try to achieve strong coupling, by enhancing the coupling according to the  $\sqrt{N}$  behaviour, with a massive thermal cloud of  $^{87}\text{Rb}$  atoms. However, once the experimental stability has further increased and the RF-Ramps can be optimized for an extended period of time under the same circumstances, attempting to condensate into a BEC would be very interesting. Furthermore, so far the RF power has not been considered and was set to an arbitrary value, while actually it has to be strong enough in the beginning, but should be decreased during the cooling. This helps to avoid power broadening, which would reduce the energy selectivity for evaporative cooling [97]. Considering this, generating a BEC is just a matter of optimizing the RF-ramps, which could even be automatized by optimal control.

Another aspect is noise. As mentioned in section 4.1 electric noise is a limiting factor for the lifetime and atomic cloud to chip distance. A filter has already been installed after the current source. But through the long cable necessary to get into the science chamber into the cryostat, a lot of noise can still be picked up. Furthermore, the break-out-box, splitting all the wires coming from the cryostat in a bundle to the individual BNC cables, seems like a haywire and needs improvement. A new breakout box has already been designed with great effort on shielding and noise filtering and waits to be installed.

Apart from the atoms in the proposed hybrid quantum system, the superconducting MW resonators still require a lot of engineering. The first series of test co-planar wave guide resonators and lumped element resonators, as well as a probe stick to test them, have been designed and produced. Once resonators with high Q-factors and the correct resonance frequency can be produced, one can think and experiment how to install them on a superconducting atomchip next to a Z-wire, without influencing the chip trap to much. Which will be an intense material science endeavour.

## 7.2. Superconducting Atomchip Prospects

What sets this atomchip experiment apart from the vast amount of atomchip experiments already out there, is the cryostat allowing for superconducting atomchips. While this complicates the operation drastically, it opens up the possibility to explore novel techniques and investigate interesting combinations of cold atoms and superconducting structures.

One of these possibilities would be to build, with the far advanced means of lithography, superconducting structures capable of trapping single flux-vortices. Atoms could then, be trapped at each vortex site, leading to an 2D lattice of atoms. 2D lattices with trapped cold atoms are nothing new. However, so far this was always done with



an optical lattice. For an optical lattice the lattice spacing has a lower bound by the wavelength of laser light necessary. For  $^{87}\text{Rb}$ , this would be 780 nm. With lattices like this solid state physics can already be well simulated, although the lattice parameter is orders of magnitudes bigger as found in real solids. A Superconducting Vortex Lattice would only be bound by the capabilities of lithography. Therefore, at least an order of magnitude smaller lattice spacings could be realized, enabling to explore new domains in quantum simulations [98, 99]. To explore this, we would first start with mesoscopic structures [89] and then subsequently make them smaller.

As described in chapter 5 and [2, 3], we could successfully tailor the current distribution in our Z-wire, employing the hysteresis behaviour of niobium. Refining this technique could help to reduce the atom cloud to chip distance, which is an important parameter to obtain strong coupling in a hybrid quantum system. For that it will be important to upgrade the chip bonds and current supply. Currently they are the limiting factor for  $I_c$ .

Our quench laser allows to reliably and effectively reset superconducting structures on the chip back into their virgin state. This allows for a whole new branch of experiments investigating superconductors, where cold atoms would probe their magnetic field. Furthermore, the quench behaviour of superconductors could be studied that way. Due to the cryo pumping effect the turn around time to change a sample in the cryostat can be in the order of a day. Which is really short compared to conventional UHV techniques. This allows measurement of several samples in an reasonable time.

The fast re-configurability could be also employed to measure the lifetime and interaction of cold atoms close to various surfaces [100]. Due to the significantly decreased JOHNSON-NYQUIST noise, the lifetime is drastically enhanced. For superconductors MEISSNER screening currents will introduce additional loss mechanisms [101], which will be highly interesting to investigate. Understanding these processes will be necessary to ultimately design an atomchip capable of housing a hybrid quantum system.

### 7.3. Atomic Recombination

While making the experiment rather complicated in maintenance and operation, the magnetic conveyor belt proved to be the best solution to transport atoms from the MOT into the cryostat. Furthermore, it enables to recombine a previously cooled cloud of cold atoms with another one. This technique can increase the atom count by up to one order of magnitude or possibly be used to merge clouds of different species [93]. Unfortunately, a current sequence to successfully merge two clouds has not been found

## 7. Outlook

---

yet. Nonetheless, we are confident that such atomic recombination can be done with minimal heating. Since merging two clouds inherently opens the traps for a short time, the recombination sequence has to be done dynamically, in a quasi adiabatic regime or by employing additional coils.

# Appendix

## A. Magnetic Transport Calculator

```
+++++
+
+           QuIc Magnetic Transport Calculator           +
+                   TU Wien 2017                       +
+                   Thomas Weigner                     +
+                   tweigner@ati.ac.at                 +
+                   vers 3.4.1                         +
+
+
+-----+
Transport parameters:
x:210.4(mm)
z:215(mm)
-----
Loading file:currentmatrix_conventional.txt
Loading file:currentlimits.txt
Loading file:switchmatrix_conventional.txt
-----
              calculating transport:
[=====]
-----
              fixing data sets:
[=====]
-----
              writing data to files:
[=====]
-----
Write times and parameters to:transport_times.txt
-----
Press any key to continue . . .
```

**Figure 1.:** Screenshot of a Magnetic Transport Calculator run with default parameters for a full conventional transport. The parameters are read from the transport parameter file.

```
Timestep for calculation (in ms)?
0.05
Use recombination? (y/n)
y
How far shall the atoms travel HORIZONTALLY? (in mm)
If you enter 0 the atoms will travel all the way to the corner.
210.4
How far shall the atoms travel VERTICALLY, BEFORE recombination? (in mm)
If you enter 0 the atoms will travel all the way to z=155mm.
155
How far shall the atoms travel VERTICALLY, AFTER recombination? (in mm)
If you enter 0 the atoms will travel all the way to z=215mm.
30
Enter t_total[ms] of the HORIZONTAL transport:
600
Enter t_vmax[ms] of the HORIZONTAL transport:
100
-----
Enter a_max[mm/ms^2] of the VERTICAL transport:
0.0038
Enter v_max [mm/ms] of the VERTICAL transport:
0.15
Enter the recombination time [ms] as used in the control program:
1000
Enter a_max[mm/ms^2] of the VERTICAL transport AFTER recombination:
0.0038
Enter v_max[mm/ms] of the VERTICAL transport AFTER recombination:
0.15
-----
Transport parameters:
x:210.4(mm)
z:155(mm)
recombination routine and then contoninue transport to z:215(mm)
-----
Loading file:currentmatrix_recombination.txt
Loading file:currentlimits.txt
Loading file:switchmatrix_recombination.txt
```

Figure 2.: Magnetic Transport Calculator screenshot of a user input example sequecne.

Here is an overview of the most relevant parts of the source code of the magnetic transport calculator. The code is often truncated and many declarations are omitted for brevity.

### A.1. main.cpp

```
/*+++++++
+           QuIc Magnetic Transport Calculator           +
+                   TU Wien 2017                       +
+                   Thomas Weigner                     +
+                   weigner.thomas@gmail.com           +
+                   main.cpp                           +
+                   vers 3.4.1                         +
+******/
```

## Appendix

---

```
#include <header.h>
//---main program
int main(){
//---declare and initialize transport parameters
:
:
//---read parameter file or user input
:
:
//-----generating polynomial by solving equations for horizontal transport and create polynomial
:
Poly polArrayHor[2]; //Creating the polynomial objects with the default constructor
polArrayHor[0].setPolynom(c1, "accelerate_hor", 4, 0.0, false); //setting the polynomial
polArrayHor[1].setPolynom(c2, "deccelerate_hor", 4, 0.0, false); //setting the polynomial
Poly eins(c1, "s1", 4, 0.0, false);
Poly zwei(c2, "s2", 4, 0.0, false);
double timeIntervalsHor[3] = {0, tHorizontalVmax, tHorizontal}; //switchtimes bwtween the
sdifferent polynoms
int intervalsHor = size(timeIntervalsHor); //number of polynoms in the
array + 1
//-----generating polynomial for vertical transport
Poly polArrayVert1[5]; //Creating the Objects with the default constructor
double vMax1 = vConst1 / 2.0; //velocity after the maximum of the acceleration
double LMin1 = (4*pow(vMax1,2))/aMax1; //minimal vertical transport distance necessary to
reach v0
double dadtmax1 = 3*pow(aMax1,2)/(4*vMax1); //maximal change of acceleration
double tMax1 = 0; //time for half of a "dip"
double tLinear1 = 0; //time with const velocity
double tVertical1 = 0; //total time of the vertical transport without
recombination
double timeIntervalsVer1 [6]; //switchtimes bwtween the sdifferent polynoms
int intervalsVer1 = size(timeIntervalsVer1); //number of polynoms in the array + 1
//---set coefficients
double coef0_1[6] = {0.0, 0.0, 0.0, 0.0, pow(aMax1,3) / (16.0 * pow(vMax1,2)),
-pow(aMax1,4) / (80.0 * pow(vMax1,3))};
double coef1_1[6] = {- 4.0*pow(vMax1,2) / (5.0*aMax1), (2.0*vMax1), (-2.0*aMax1),
pow(aMax1,2) / vMax1,
(-3.0*pow(aMax1,3)) / (16.0 * pow(vMax1,2)), pow(aMax1,4) / (80.0 * pow(vMax1,3))};
double coef2_1[2] = {0.0, vConst1};
double coef3_1[6] = {4.0*pow(vMax1,2) / (5.0*aMax1), (-2.0*vMax1), (2.0*aMax1),
-pow(aMax1,2) / vMax1,
(3.0*pow(aMax1,3)) / (16.0 * pow(vMax1,2)), -pow(aMax1,4) / (80.0 * pow(vMax1,3))};
double coef4_1[6] = {0.0, 0.0, 0.0, 0.0, -pow(aMax1,3) / (16.0 * pow(vMax1,2)),
pow(aMax1,4) / (80.0 * pow(vMax1,3))};
//---set polynoms only if necessary
if( traveldistance [0] == XFINAL && traveldistance[1] > 0.0){ //is vertical transport relevant?
if ( traveldistance [1] / 2 >= LMin1){ // can aMax be even reached?
tMax1 = 2 * vMax1 / aMax1;
```

## Appendix

---

```

tLinear1 = (traveldistance[1] - 2 * LMin1) / vConst1;
tVertical1 = tLinear1 + 4*tMax1;

}
else{
  LMin1 = traveldistance[1] / 2.0; //set to LMin to minimum no lineat part
  vMax1 = pow(dadtmax1*pow(LMin1,2) / 12.0, 1.0/3.0); //calculate new vMax1
  aMax1 = 4*pow(vMax1,2)/LMin1; //calculate new aMax1
  tMax1 = 2*vMax1/aMax1;
  tVertical1 =4 *tMax1;
}
//---set interval array
double temp[intervalsVer1] = {0, tMax1, 2*tMax1, tLinear1 + 2*tMax1, tLinear1 + 3*tMax1,
  tVertical1};
for(int i = 0; i < intervalsVer1; i++){
  timeIntervalsVer1[i] = temp[i];
}
//---increase acceleration
polArrayVert1[0].setPolynom(coef0_1, "accelerate_vert1", 5, 0.0, false);
//---decrease acceleration
polArrayVert1[1].setPolynom(coef1_1, "accelerate_vert2", 5, tMax1, false);
//---constant velocity
polArrayVert1[2].setPolynom(coef2_1, "const_vert", 1, 0.0, false); //setting the polynom
polArrayVert1[2].addOffset(polArrayVert1[1].calculate(tMax1));
//---increase deceleration
polArrayVert1[3].setPolynom(coef3_1, "deccelerate_vert1", 5, 2*tMax1, true);
polArrayVert1[3].addOffset(polArrayVert1[2].calculate(tLinear1) +
  polArrayVert1[1].calculate(tMax1));
//---decrease deceleration
polArrayVert1[4].setPolynom(coef4_1, "deccelerate_vert2", 5, tMax1, true);
polArrayVert1[4].addOffset(polArrayVert1[2].calculate(tLinear1) +
  polArrayVert1[1].calculate(tMax1));
}
//-----generating polynom for vertical transport after recombination
Poly polArrayVert2[5]; //Creating the Objects with the default constructor
double vMax2 = vConst2 / 2.0; //velocity after the maximum of the accerleration
double LMin2 = (4*pow(vMax2,2))/aMax2; //minimal vertical transport distance necesary to
  reach v0
double dadtmax2 = 3*pow(aMax2,2)/(4*vMax2); //maximal change of acceleration
double tMax2 = 0; //time for half of a "dip"
double tLinear2 = 0; //time with const velocity
double tVertical2 = 0; //total time of the vertical transport without
  recombination
double timeIntervalsVer2 [6]; //switchtimes between the sdifferent polynoms
int intervalsVer2 = size(timeIntervalsVer2); //number of polynoms in the array + 1
//---set coefficients
double coef0_2[6] = {ZRECOMB2, 0.0, 0.0, 0.0, pow(aMax2,3) / (16.0 * pow(vMax2,2)),
  -pow(aMax2,4) / (80.0 * pow(vMax2,3))};

```

## Appendix

---

```

double coef1_2[6] = {ZRECOMB2 - 4.0*pow(vMax2,2) / (5.0*aMax2), (2.0*vMax2),
    (-2.0*aMax2), pow(aMax2,2) / vMax2,
    (-3.0*pow(aMax2,3)) / (16.0 * pow(vMax2,2)), pow(aMax2,4) / (80.0 * pow(vMax2,3))};
double coef2_2[2] = {0.0, vConst2};
double coef3_2[6] = {4.0*pow(vMax2,2) / (5.0*aMax2), (-2.0*vMax2), (2.0*aMax2),
    -pow(aMax2,2) / vMax2,
    (3.0*pow(aMax2,3)) / (16.0 * pow(vMax2,2)), -pow(aMax2,4) / (80.0 * pow(vMax2,3))};
double coef4_2[6] = {0.0, 0.0, 0.0, 0.0, -pow(aMax2,3) / (16.0 * pow(vMax2,2)),
    pow(aMax2,4) / (80.0 * pow(vMax2,3))};
//---set polynoms only if necessary
if( traveldistance [1] == ZRECOMB && recomb == 1){ //is vertival transport relevant?
    if ( traveldistance [2] / 2 >= LMin2){ //can aMax be even reached?
        tMax2 = 2 * vMax2 / aMax2;
        tLinear2 = (traveldistance [2] - 2 * LMin2) / vConst2;
        tVertical2 = tLinear2 + 4*tMax2;
    }
    else {
        LMin2 = traveldistance[2] / 2.0; //set to LMin to minimum no lineat part
        vMax2 = pow(dadtmax2*pow(LMin2,2) / 12.0, 1.0/3.0); //calculate new vMax2
        aMax2 = 4*pow(vMax2,2)/LMin2; //calculate new aMax2
        tMax2 = 2*vMax2/aMax2;
        tVertical2 =4 * tMax2;
    }
    //---set interval array
    double temp[intervalsVer2] = {0, tMax2, 2*tMax2, tLinear2 + 2*tMax2, tLinear2 + 3*tMax2,
        tVertical2};
    for(int i = 0; i < intervalsVer2; i++){
        timeIntervalsVer2[i] = temp[i];
    }
    //---increase acceleration
    polArrayVert2[0].setPolynom(coef0_2, "accelerate_vert_postrecomb1", 5, 0.0, false);
    //---decrease acceleration
    polArrayVert2[1].setPolynom(coef1_2, "accelerate_vert_postrecomb2", 5, tMax2, false);
    //---constant velocity
    polArrayVert2[2].setPolynom(coef2_2, "const_vert_postrecomb", 1, 0.0, false);
    polArrayVert2[2].addOffset(polArrayVert2[1].calculate(tMax2));
    //---increase deceleration
    polArrayVert2[3].setPolynom(coef3_2, "deccelerate_vert_postrecomb1", 5, 2*tMax2, true);
    polArrayVert2[3].addOffset(polArrayVert2[2].calculate(tLinear2) +
        polArrayVert2[1].calculate(tMax2) - ZRECOMB2);
    //---decrease deceleration
    polArrayVert2[4].setPolynom(coef4_2, "deccelerate_vert_postrecomb2", 5, tMax2, true);
    polArrayVert2[4].addOffset(polArrayVert2[2].calculate(tLinear2) +
        polArrayVert2[1].calculate(tMax2) - ZRECOMB2);
}
//-----read currentmatrix, currentlimits, switchmatrix
string temp, fileName; //dummy string to read labels from files , filename to read from
//---reading currentmatrix

```

```

double cm[CMROWS][ANALOGCHANNELS+1]; //curretnmatrix
int currentMatrixRows = 0; //number of rows in the curretnmatrix smaller than
    CWROWS if recombination is activated
ifstream currentmatrix;
if (recomb == 0){ //load currentmatrix conventional
    cout << "Loading file:" << CURRENTMATRIXCONVEN << endl;
    fileName = CURRENTMATRIXCONVEN;
}
else if (recomb == 1){ //load currentmatrix recombination
    cout << "Loading file:" << CURRENTMATRIXRECOMB << endl;
    fileName = CURRENTMATRIXRECOMB;
}
else{ //invalid parameter?
    cout << "+++error: invalid recomb variable: " << recomb << endl;
}
currentmatrix.open(fileName);
if (currentmatrix.is_open()){ //read currentmatrix
    for (int i=0; i<ANALOGCHANNELS+1; i++){
        currentmatrix >> temp;
    }
    while(currentmatrix.good()){
        for (int j=0; j<ANALOGCHANNELS+1; j++){
            currentmatrix >> cm[currentMatrixRows][j];
        }
        currentMatrixRows++;
    }
    currentmatrix.close();
}
else{ //unable to open file?
    cout << "+++error: unable to open: " << fileName << endl;
}
//---read current limits from file
cout << "Loading file:" << CURRENTLIMITS << "\n";
double currentLimits[ANALOGCHANNELS];
ifstream currentLimit(CURRENTLIMITS);
if (currentLimit.is_open()){ //read current limits
    int j = 0;
    while(currentLimit.good() && j<ANALOGCHANNELS){
        currentLimit >> currentLimits[j] >> temp;
        j++;
    }
    currentLimit.close();
}
else{ //unable to open file?
    cout << "+++error: unable to open: " << CURRENTLIMITS << endl;
}
//---read switch matrix from file
if (recomb == 0){ //load switchmatrix conventional

```



```

cout << "Loading file:" << SWITCHMATRIXCONVEN << endl;
fileName = SWITCHMATRIXCONVEN;
}
else if (recomb == 1){ //load switchmatrix recombination
cout << "Loading file:" << SWITCHMATRIXRECOMB << endl;
fileName = SWITCHMATRIXRECOMB;
}
ifstream switchmatrix(fileName);
double sw[SWROWS][DIGITALCHANNELS+1];
int switchMatrixRows = 0;
if (switchmatrix.is_open()){ //read switchmatrix
while (switchmatrix.good() && switchMatrixRows < DIGITALCHANNELS+1){ //read first line
with labels to dummy string
switchmatrix >> temp;
switchMatrixRows++;
}
switchMatrixRows = 0;
while (switchmatrix.good() && switchMatrixRows < SWROWS){
for (int j = 0; j < DIGITALCHANNELS+1; j++){
switchmatrix >> sw[switchMatrixRows][j];
}
switchMatrixRows++;
}
switchmatrix.close();
}
else { //unable to open file?
cout << "+++error: unable to open: " << fileName << endl;
}
//---set up temporary coilsetting storage
double preCoilSetting[DIGITALCHANNELS+1]; //temporary stores the previous coilsetting to
later compare if there were any changes
for (int j = 0; j < DIGITALCHANNELS+1; j++){
preCoilSetting[j] = sw[0][j];
}
//-----initialize main calculation
//---initialize lists to store the datafiles, and set progressbar
double tTotal = tHorizontal+tVertical1+tVertical2;
//---declare lists which contain structs with two double values (time, value)
list <dataP> currents[ANALOGCHANNELS]; //contains all analog channels, each timestep adds
an element to columns time and I
list <dataP> switches[DIGITALCHANNELS]; //contains all digital channels, each switch adds an
element to columns time and binary state
list <dataP>::iterator it; //master iterator for data lists
//---declare transport section parameters
int currIndex = 0; //index for the currentmatrix (continuous over all sections)
int switchIndex = 0; //index for the switchmatrix (continuous over all sections)
int interval; //index for the intervals array
double time; //time variable

```

## Appendix

---

```

double x;           //spatial variable sideways
double z;           //spatial variable sideways
int maxSwitchIndex; //highest index in the switch matrix
int maxCurrIndex;  //highest index in the current matrix
//---initialize digital channels (let each digital channel start with off ("0") except MOT)
for(int digiCh = 0; digiCh < DIGITALCHANNELS; digiCh++){
    dataP temp;
    temp.time = sw[switchIndex][0]; //set time stamp
    temp.value = sw[switchIndex][digiCh+1];
    switches[digiCh].push_back(temp);
}
//-----horizontal part, get digitalchannels(t) and I(t)
//---initialize for horizontal part
interval = 0;
time = -timeStep; //start with - one timeStep so the first loop has a time of 0
x = 0;
maxSwitchIndex = intIndexDivison(traveldistance[0], SWITCHMATRIXSTEPsize, false);
maxCurrIndex = intIndexDivison(traveldistance[0], CURRENTMATRIXSTEPsize, false);
//---increase time and calculate the correspondig x values for the horizontal part
//the time goes from the beginning to the end since the polynoms are the solution for the
    equations for the whole horizontall transport
while(time <= tHorizontal){
    time = time + timeStep;
    x = polArrayHor[interval].calculate(time);
    check4DigiChSwitches(x, time, switches, sw, switchIndex, maxSwitchIndex, preCoilSetting);
    calculateCurrents(x, time, currents, cm, currIndex, currentLimits, maxCurrIndex);
    setInterval(time, timeIntervalsHor, interval, intervalsHor, timeStep);
}
//-----first vertical part, get digitalchannels(t) and I(t)
if( traveldistance [1] > 0.0 && traveldistance[0] == XFINAL){
    //---initialize for vertical part
    interval = 0;
    time = -timeStep; //start with - one timeStep so the first loop has a time of 0
    z = 0;
    maxSwitchIndex = intIndexDivison(XFINAL + traveldistance[1],
        SWITCHMATRIXSTEPsize, true); //the switch matrix is continous => true => +1 for
        the 0 starting the vertical part
    maxCurrIndex = intIndexDivison(XFINAL + traveldistance[1],
        CURRENTMATRIXSTEPsize, false); //the current matrix
    //---increase time and calculate the correspondig x values for the horizontal part
    while(time <= tVertical){
        time = time + timeStep;
        //time goes always just from zero to the end of one interval since the polynomes are put
            together piecewise
        z=polArrayVert1[interval].calculate(time-timeIntervalsVer1[interval]);
        check4DigiChSwitches(z, time+tHorizontal, switches, sw, switchIndex, maxSwitchIndex,
            preCoilSetting);
    }
}

```

## Appendix

---

```

    calculateCurrents(z + XFINAL, time + tHorizontal, currents, cm, currIndex, currentLimits,
        maxCurrIndex);
    setInterval (time, timeIntervalsVer1, interval , intervalsVer1 , timeStep);
}
}
//-----recombination, add node where porlatiy of V7 and V8 switches
double swTimeRecomb = 0.0; //declare polarity switch time for recombination
if (recomb == 1 && traveldistance[1] == ZRECOMB){ //verticval transport after recombination
    necessary?
    swTimeRecomb = tHorizontal + tVertical1 + cm[currIndex][V7a] * tRecomb /
        (cm[currIndex][V7b] + cm[currIndex][V7a]); //calculate time polarity switches during
        recomb
    //---add polarity switchpoint in linear ramp
    currents[V7a].push_back({swTimeRecomb, 0});
    currents[V7b].push_back({swTimeRecomb, 0});
    currents[V8a].push_back({swTimeRecomb, 0});
    currents[V8b].push_back({swTimeRecomb, 0});
    //---set digital channel switchtimes
    //V7
    switches[VERT7a].push_back({swTimeRecomb + SWITCHOFFDELAY -
        DIGIFRINGETIME, 1});
    switches[VERT7a].push_back({swTimeRecomb + SWITCHOFFDELAY, 0});
    switches[VERT7b].push_back({swTimeRecomb + SWITCHONHOLDBACKTIME -
        DIGIFRINGETIME, 0});
    switches[VERT7b].push_back({swTimeRecomb + SWITCHONHOLDBACKTIME, 1});
    //V8
    switches[VERT8b].push_back({swTimeRecomb+ SWITCHOFFDELAY -
        DIGIFRINGETIME, 1});
    switches[VERT8b].push_back({swTimeRecomb + SWITCHOFFDELAY, 0});
    switches[VERT8a].push_back({swTimeRecomb + SWITCHONHOLDBACKTIME -
        DIGIFRINGETIME, 0});
    switches[VERT8a].push_back({swTimeRecomb + SWITCHONHOLDBACKTIME, 1});
}
//-----vertical part after recombination, get digitalchannels(t) and I(t)
if (traveldistance [2] > 0.0 && recomb == 1 && traveldistance[1] == ZRECOMB){
    //---initialize for vertical part after recombination
    interval = 0;
    time = -timeStep; //start with - one timeStep so the first loop has a time of 0
    z = 0;
    maxSwitchIndex = 1 + intIndexDivison(XFINAL + ZRECOMB + traveldistance[2],
        SWITCHMATRIXSTEPSIZE, true); //the switch matrix is continous => true => +1 for
        the 0 starting the vertical part
    maxCurrIndex = intIndexDivison(XFINAL + ZRECOMB + traveldistance[2],
        CURRENTMATRIXSTEPSIZE, false); //the current matrix
    //reset check for digital switches since during recombination they are done manually
    for (int digiCh = 0; digiCh < DIGITALCHANNELS+1; digiCh++){
        preCoilSetting [digiCh] = sw[switchIndex+1][digiCh];
    }
}

```

## Appendix

---

```
//---increase time and claculate the correspondig x values for the horizontal part
//time goes always just from zero to the end of one interval since the polynomes are put
  together piecewise
while(time <= tVertical2){
  time = time + timeStep;
  z=polArrayVert2[interval].calculate(time-timeIntervalsVer2[interval]);
  check4DigiChSwitches(z, time + tHorizontal + tVertical1 + tRecomb, switches, sw,
    switchIndex, maxSwitchIndex, preCoilSetting);
  calculateCurrents(z + XFINAL, time + tHorizontal + tVertical1 + tRecomb, currents, cm,
    currIndex, currentLimits, maxCurrIndex);
  setInterval (time, timeIntervalsVer2, interval, intervalsVer2, timeStep);
}
}
//-----clean up analog channel data lists (delet unnecessary entries)
for (int anaCh=0; anaCh < ANALOGCHANNELS; anaCh++){
  int delCount = 0;
  if (currents[anaCh].size() > 2){
    list <dataP>::iterator last, next2Last;    //additional iterartors for data lists
    it = currents[anaCh].begin();
    last = currents[anaCh].begin();
    next2Last = currents[anaCh].begin();
    advance(it, 2);
    advance(last, 1);
    while(it != currents[anaCh].end()){
      if ( next2Last->value == last->value && last->value == it->value){
        currents[anaCh].erase(last++);
        delCount ++;
        advance(it, 1);
        next2Last = last;
        --next2Last;
      }
      else{
        ++next2Last;
        ++last;
        ++it;
      }
    }
  }
}
else{
  cout << "error no data in currents, channel:" << anaCh;
}
}
//-----write data to files and end program
:
```

## A.2. header.h

```

/*+++++
+           QuIc Magnetic Transport Calculator           +
+           TU Wien 2017                               +
+           Thomas Weigner                             +
+           weigner.thomas@gmail.com                   +
+           header.h                                   +
+           vers 3.4.1                                 +
+++++*/
//---struct for a datapoint containing a time stamp and a value
struct dataP{
    double time;
    double value;
};
//---calculates the length of an array
template<class T, size_t N>
constexpr size_t size(T (&)[N]) { return N;}
//---linearly interpolates the currentmatrix and checks if any currenlimit of the
    currensources gets exceeded
double interPolCurr(double x1, double x2, double y1, double y2, double x, double currentLimit){
    double y = y1 + (y2-y1)*((x-x1)/(x2-x1));
    if(y < currentLimit){
        return y;
    }
    else{
        logFile << "+++error: currentlimit " << currentLimit << " (A) exceeded at " << x <<
            endl;
        return y;
    }
};
//---calculate the highest index of the switch matrix and current matrix for a transport section
int intIndexDivison(double distance, double step, bool zero){
    int index = (int) distance / step;
    double remainder = distance - (double) index * step;
    if(remainder / step < 1.0){
        index = index + 1;
    }
    else{
        index = index + remainder / step;
    }
    if(zero){
        index = index + 1;
    }
    return index;
};
//---check if index iteration is necessary, iterate and check if switch is necessary

```

```

void check4DigiChSwitches(double x, double time, list<dataP>
(&switches)[DIGITALCHANNELS], double sw[SWROWS][DIGITALCHANNELS+1], int
&switchIndex, int maxSwitchIndex, double (&preCoilSetting)[DIGITALCHANNELS+1]){
while(x > (sw[switchIndex+1][0]-SWITCHPOINTMARGIN) && switchIndex <
maxSwitchIndex){
switchIndex++;
char buffer [BUFFERSIZE];
sprintf (buffer , "=== pos:%3.3f(mm) sw_index:%4d pos in SW_matrix:%3.3f(mm)
maxSw_index:%4d t:%3.3f(ms)", x, switchIndex, sw[switchIndex][0], maxSwitchIndex,
time);
for (int digiCh = 0; digiCh < DIGITALCHANNELS; digiCh++){
if (sw[switchIndex][digiCh+1] != preCoilSetting[digiCh+1]){
string switchMessage = selectDigiChannel(digiCh);
if (sw[switchIndex][digiCh+1] == 1){
switchMessage = switchMessage + " on ";
switches[digiCh].push_back({time - SWITCHONHOLDBACKTIME, 0});
switches[digiCh].push_back({time - SWITCHONHOLDBACKTIME +
DIGIFRINGETIME, 1});
}
if (sw[switchIndex][digiCh+1] == 0){
switchMessage = switchMessage + " off ";
switches[digiCh].push_back({time + SWITCHOFFDELAY -
DIGIFRINGETIME, 1});
switches[digiCh].push_back({time + SWITCHOFFDELAY, 0});
}
}
}
//---add final entry in switchvector
else if (switchIndex >= maxSwitchIndex-1){ // max switch index is never reached; at
last execution of an transport section also the last point is print so the for
interpolating
switches[digiCh].push_back({time, sw[switchIndex][digiCh+1]});
}
preCoilSetting[digiCh+1] = sw[switchIndex][digiCh+1];
}
}
};
//---calculate I(t) for all channels by interpolating at the curretn matrix at currIndex
void calculateCurrents(double x, double time, list <dataP> (&currents)[ANALOGCHANNELS],
double (&cm)[CMROWS][ANALOGCHANNELS+1], int &currIndex, double
currentLimits[ANALOGCHANNELS], double maxCurrIndex){
//---iterate current matrix index if necessary
while(x > (cm[currIndex+1][0]-SWITCHPOINTMARGIN) && currIndex <
maxCurrIndex-1){
currIndex++;
logFile << x << " " << currIndex << " " << cm[currIndex][0] << endl;
}
//---write I(t) to the lists by interpolating the curretnmatrix
for (int anaCh = 0; anaCh < ANALOGCHANNELS; anaCh++){

```

```

dataP temp;
temp.time = time; //set time stamp
/*linearly interpolate cm and round I(t)*/
temp.value = fround(interPolCurr(cm[currIndex][0], cm[currIndex+1][0],
    cm[currIndex][anaCh+1], cm[currIndex+1][anaCh+1], x, currentLimits[anaCh]),
    ROUNDPRECISION); //set current
currents[anaCh].push_back(temp); //write struct to list
if (printLogFile){
    if (temp.value != 0.0){
        char buffer [BUFFERSIZE];
        sprintf (buffer , " I_limit:%3.0f(A) I:%6.2f(A) I_index:%4d x:%3.2f(mm)
            t:%6.2f(ms)", currentLimits[anaCh], temp.value, currIndex, x, time);
        logFile << selectAnaChannel(anaCh) << buffer << endl;
    }
}
};
//---switch to the next interval / polynom if the end of the interval is reached
void setInterval (double &time, double *timeIntervals,int &interval, int maxIntervals, double
    timeStep){
    if ((time >= timeIntervals[interval + 1]) && (time <= (timeIntervals[interval + 1] +
        timeStep))){
        if (printLogFile){
            char buffer [BUFFERSIZE];
            sprintf (buffer , "+++ change time interval at t:%6.2f(ms) from %6.2f to %6.2f
                int:%3d", time, timeIntervals[interval], timeIntervals [interval + 1], interval);
            logFile << buffer << endl;
        }
        interval++;
        if (interval < maxIntervals-1){
            time = timeIntervals [interval ];
        }
    }
};

```





```

coef = c;
if (polynomialOrder < 0){
    order = 0;
    cout << "error: negative polynomial order! order was set to 0";
}
else{
    order = polynomialOrder;
}
};
//---add and double value to the 0 order coefficient
void Poly::addOffset(double offset){
    coef[0] = coef[0] + offset;
};
//---print the coefficient on the screen for debugging purpose
void Poly::printcoef(){
    cout << "Die Funktion " << name << " hat folgende Koeffizienten:" << endl;
    for (int i=0; i <= order; i++){
        cout << coef[i] << endl;
    }
};
//---calculates p(x)
double Poly::calculate(double x){
    double y = 0;
    if (reverse){
        for (int i=0; i<=order; i++){
            y = y + coef[i]*pow(offset - x,i);
        }
    }
    else{
        for (int i=0; i<=order; i++){
            y = y + coef[i]*pow(offset + x,i);
        }
    }
    return y;
};
//---calculates p'(x)
double Poly::calculateD1(double x){
    double y = 0;
    if (order < 1){
        return 0;
    }
    for (int i = 1; i <= order; i++){
        y = y + coef[i]*pow(x+ offset,(i-1))*i;
    }
    return y;
};
//---calculates p''(x)
double Poly::calculateD2(double x){

```

```
double y = 0;
if (order < 2){
    return 0;
}
for (int i = 2; i <= order; i++){
    y = y + coef[i]*pow(x,(i-2))*i*(i-1);
}
return y;
};
```

---

## B. <sup>87</sup>Rb Zeeman Sublevels

Starting from the linearised interaction term eq. (2.4), we want to derive the ZEEMAN splitting. The magnetic moments occurring in it, can be also expressed with the gyro-magnetic ratio  $\gamma$  in terms of angular momentum,

$$\gamma = \frac{\boldsymbol{\mu}}{\mathbf{L}} = \frac{\frac{q}{2}\mathbf{r} \times \mathbf{v}}{m\mathbf{r} \times \mathbf{v}} = \frac{q}{2m}. \quad (1)$$

This holds for a classical point particle with mass  $m$ , charge  $q$ , and velocity  $\mathbf{v}$  around a disk with radius  $r$ , which would correspond to the trivial BOHR model for an atom. Therefore, we need to correct  $\gamma$  by a factor  $g$  depending on the type of magnetic moment. We then can write gyro-magnetic ratio in multiples of the constant  $\mu_B$ , which is called BOHR-magneton, .

$$\mu_B = \frac{e\hbar}{2m_e} \approx 9.274 \times 10^{-24} \text{ J T}^{-1}, \quad (2)$$

$$\gamma = \frac{g\mu_B}{\hbar}. \quad (3)$$

The spin g-factor  $g_S$  can be derived using QED and is approximately 2. While the orbital g-factor  $g_L$  accounts for the finite nuclear mass and is written as

$$g_L = 1 - \frac{m_e}{m_{\text{nucleus}}}, \quad (4)$$

which can be approximated by 1. The nucleus is not a DIRAC-particle since it has an inner structure, made of protons and neutrons, with the nucleus g-factor  $g_I$ , which is normally experimentally determined [22].

Rewriting eq. (2.4), using angular momenta and spin, the ZEEMAN Hamiltonian writes as

$$\hat{H} = \left( g_L \hat{\mathbf{L}} + g_S \hat{\mathbf{S}} + g_I \hat{\mathbf{I}} \right) \mu_B \mathbf{B} = \left( g_L \hat{L}_z + g_S \hat{S}_z + g_I \hat{I}_z \right) \mu_B B_z \quad (5)$$

where it makes sense to set the  $z$ -axis in direction of the magnetic field and therefore choose  $z$ -direction as quantizations axis, thus  $\mathbf{B} = B_z \hat{\mathbf{z}}$ .  $\hat{L}_z, \hat{S}_z, \hat{I}_z$  are then angular momenta and spin operators along the direction of the magnetic field.

The eigenvalues of the  $z$ -axis operators are  $m_L, m_S$  and  $m_I$  which are called magnetic quantum numbers. Using these, the Energy shift can be written as

$$\Delta E = (g_L m_L + g_S m_S + g_I m_I) \mu_B B_z. \quad (6)$$

Since  $\mathbf{L}$  and  $\mathbf{S}$  couple to the electron momentum, it makes sense to also introduce a  $g_J$ -factor, which is also called LANDÉ factor

$$\widehat{\mathbf{J}} = \widehat{\mathbf{L}} + \widehat{\mathbf{S}}, \quad (7)$$

$$\boldsymbol{\mu}_J = \boldsymbol{\mu}_L + \boldsymbol{\mu}_S, \quad (8)$$

$$g_J \mu_B \widehat{\mathbf{J}} = g_L \mu_B \widehat{\mathbf{L}} + g_0 \mu_B \widehat{\mathbf{S}}. \quad (9)$$

multiplying by  $\widehat{\mathbf{J}}$  yields:

$$g_J \widehat{\mathbf{J}} \cdot \widehat{\mathbf{J}} = g_L \left( \widehat{L}^2 + \widehat{\mathbf{L}} \cdot \widehat{\mathbf{S}} \right) + g_S \left( \widehat{S}^2 = \widehat{\mathbf{S}} \cdot \widehat{\mathbf{L}} \right) \quad (10)$$

$$g_J \widehat{J}^2 = g_L \left( \widehat{L}^2 + \frac{1}{2} \left( \widehat{J}^2 - \widehat{L}^2 - \widehat{S}^2 \right) \right) + g_S \left( \widehat{S}^2 + \frac{1}{2} \left( \widehat{J}^2 - \widehat{L}^2 - \widehat{S}^2 \right) \right) \quad (11)$$

$$g_J = g_L \frac{J(J+1) + L(L+1) - S(S+1)}{2J(J+1)} + g_S \frac{J(J+1) + S(S+1) - L(L+1)}{2J(J+1)} \quad (12)$$

Approximating  $g_S = 2$  and  $g_L = 1$ , one gets the simplified expression

$$g_J \simeq \frac{3}{2} + \frac{S(S+1) - L(L+1)}{2J(J+1)} \quad (13)$$

Measured  $g$ -factors from [20] for  $^{87}\text{Rb}$  are given in table 1

$g_L$	0.999993	$g_S$	2.002319	$g_I$	-0.000995
$g_J(5^2S_{1/2})$	2.002331	$g_J(5^2P_{1/2})$	0.666	$g_J(5^2P_{3/2})$	1.3362

**Table 1.:** Experimental  $^{87}\text{Rb}$  values for  $g$ -factors

As described in section 2.1.1, the various magnetic moments can also be described as the total angular momentum  $\mathbf{F}$

$$\widehat{H} = -\boldsymbol{\mu}_F \mathbf{B} = g_F \widehat{F}_z \mu_B B_z. \quad (14)$$

According to eq. (2.1) the corresponding  $g$ -factor is calculated analogue to eq. (12) as

$$g_F = g_J \frac{F(F+1) + J(J+1) - I(I+1)}{2F(F+1)} + g_I \frac{F(F+1) + I(I+1) - J(J+1)}{2F(F+1)}, \quad (15)$$

whereas  $g_I$  as seen in table 1, is negligible to  $g_J$  and leaves only the first term.

Inserting eq. (13) in eq. (15) we obtain

$$g_F \simeq \left( \frac{3}{2} + \frac{S(S+1) - L(L+1)}{2J(J+1)} \right) \frac{F(F+1) + J(J+1) - I(I+1)}{2F(F+1)}. \quad (16)$$

With  $I = \frac{3}{2}$  for  $^{87}\text{Rb}$  we get the  $g_F$  factors for the D2 line in table 2.

State	$g_F$		
	F = 1	F = 2	F = 3
$5^2\text{S}_{1/2}$	$-\frac{1}{2}$	$\frac{1}{2}$	
$5^2\text{P}_{1/2}$	$-\frac{1}{6}$	$\frac{1}{6}$	
$5^2\text{P}_{3/2}$	$\frac{2}{3}$	$\frac{2}{3}$	$\frac{2}{3}$

**Table 2.:** Calculated values for  $g_F$ -factors using the above described approximations

In an external magnetic field  $B_z$ , the magnetic moment  $\boldsymbol{\mu}_F$  will start precessing around the  $z$ -axis, depending on the orientation of  $\hat{\mathbf{F}}$ , with  $\omega_L$  the LARMOR frequency. Therefore, it makes sense to introduce the quantum number  $m_F$ ,

$$\langle \hat{F}_z \rangle = m_F F \hbar. \quad (17)$$

The degenerated hyperfine state splits in  $2F + 1$  ZEEMAN-levels since  $m_F$  describes the orientation of  $\mathbf{F}$  to the quantization axis, it is called the magnetic quantum number and can take values

$$-F \leq m_F \leq F. \quad (18)$$

With this the ZEEMAN splitting energy gap writes as

$$\Delta E = g_F m_F \mu_B B_z = \hbar \omega_L. \quad (19)$$

Figure 3 shows the complete  $^{87}\text{Rb}$  D2 line manifold with a small external field.

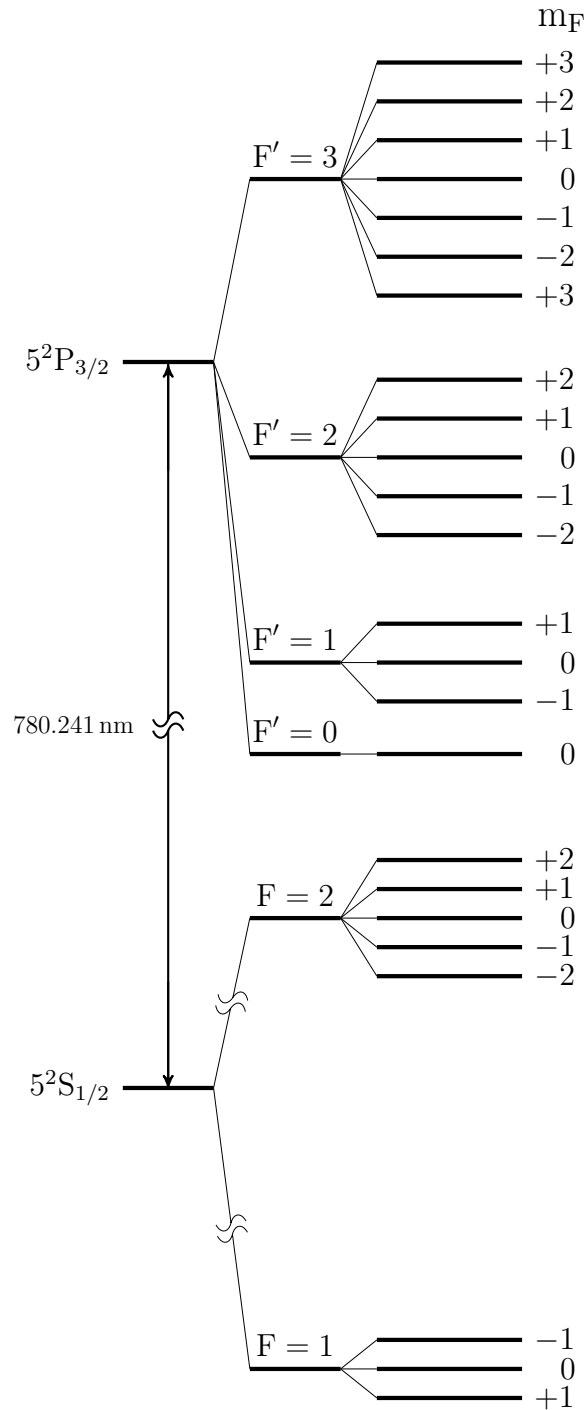


**Figure 3.:** To scale diagram of all  $^{87}\text{Rb}$  D2 line hyperfine ZEEMAN sublevels. The groundstate hyperfine splitting scaled by a factor 10, while the different ZEEMAN splittings through  $g_F = \frac{1}{2}, -\frac{1}{2}$  and  $\frac{2}{3}$  is to scale.

# C. Young Atomic Opticians Conference Poster



TECHNISCHE  
UNIVERSITÄT  
WIEN  
Vienna University of Technology

## Ultracold atoms in a cryogenic environment

Thomas Weigner, Fritz Diorico, Stefan Minniberger, Žaneta Kurpias, Naz Shokrani,  
Jörg Schmiedmayer



ATOMINSTITUT



VCQ  
Vienna Center for Quantum  
Science and Technology

Atominstytut TU Wien– Vienna Center for Quantum Science and Technology  
Stationale 2, 1020 Vienna, Austria

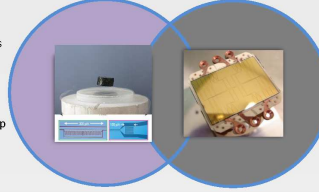


AtomChip

### Cryogenic environment -> Superconductors

Cryogenic environments allow the use of superconductors as well as very good UHV due to cryo-pumping.

Superconductors have several unique properties such as remanent magnetization (for type II) and the lack of Johnson-Nyquist noise. These can be used as a new tool for manipulating ultracold atoms on a superconducting atomchip and creating Hybrid Quantum Systems with ultracold atoms and superconducting circuits.

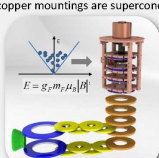


### Ultracold atoms on a Atomchip

Atomchips are an ideal platform to combine the long lived magnetic hyperfine states of trapped atoms as quantum memory with the processing capabilities of super-conducting qubits through coupling, mediated by micro wave photons in coplanar waveguide resonators (CPWR).

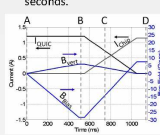
### Magnetic Transport for Ultracold Atoms

We use a magnetic conveyor belt to transport ultra-cold <sup>85</sup>Rb atoms from a room temperature magnetic-optical trap (MOT) into a cryostat. The colored coils are all at room temperature. While the coils on the copper mountings are superconducting.



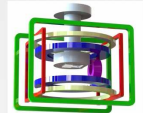
$E = g_F m_F \mu_B |B|$

gold-plated 4K experimental stage of a two-stage cryogen-free Gifford-McMahon refrigerator. The setup is suspended from the ceiling and vibration damped via a He-bulder and a below. The insets show our atom chip, made of 500nm Niobium film on a Sapphire substrate.



### Transport Performance and Reloading Sequence

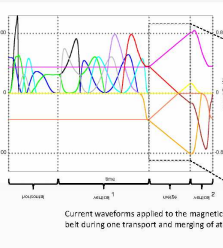
After the transport of initially about 10<sup>5</sup>, with an efficiency of around 60%, we convert the quadrupole trap to a Quadrupole-Ioffe configuration, to allow for RF evaporative precooling and lifetimes of up to 300 seconds.



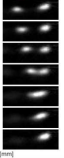
the blue coils are the last two transport coils, the small purple one is the Ioffe coil and the white cylinder is the chip mount with the chip glued to its bottom. The others coils provide bias fields in all directions.

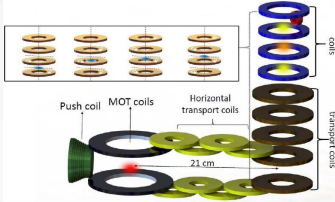
### Atomic Recombination with the Magnetic Conveyor Belt Transport

Merging of atom clouds has already been done in a small scale on an atomchip with an array of antennas. With our magnetic conveyor belt we plan to scale this up to a multi MOT experiment cycle.



Current waveforms applied to the magnetic conveyor belt during one transport and merging of atomic clouds





Push coil MOT coils Horizontal transport coils

20 cm  
SC transport coils  
21 cm  
Non-vertical transport coils

While a new batch of atoms (red) are cooled in the MOT, the previous ones are transported to the cryogenic environment and then recombine with the atom cloud, already there (yellow) in the center of the superconducting coils (orange).

This procedure can repeat until an equilibrium between atom loss and atom growth is reached. We estimate to be able to increase the atom count beneath the chip by one order of magnitude.

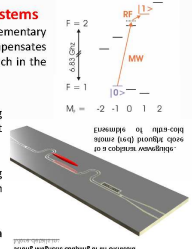
### Hybrid Quantum Systems

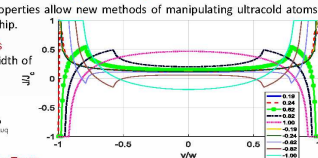
Combining different physical systems with complementary functionalities, where the strength of one system compensates for the weaknesses of another, is a promising approach in the field of quantum information.

**Superconducting Qubits** like transmon qubits, allow for very fast processing and promise dense integration, but have very short coherence times.

**Quantum Memories** can be realised by exploiting the exceptional long coherence times in atomic ensembles (Bose-Einstein condensates).

**Photon Bus-Systems** would mediate via a virtual photon between a collective Dicke-state of atoms and a solid-state Qubit.



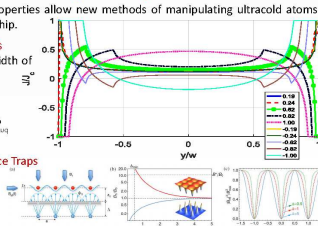


### Novel Superconducting Microtraps for Cold Atoms

Superconductors' unique properties allow new methods of manipulating ultracold atoms on a superconducting atomchip.

**Remnant magnetization traps** allow tuning the effective width of the wire by controlling the current history.

**Superconducting Vortex Lattice Traps** could trap single atoms analogue to optical lattices



# List of Figures

2.1.	$^{87}\text{Rb}$ D1,D2 line . . . . .	6
2.2.	ZEEMAN splitting . . . . .	8
2.3.	$^{87}\text{Rb}$ $5^2\text{S}_{1/2}$ clock state . . . . .	10
2.4.	DFS setup . . . . .	11
2.5.	velocity distributions for laser spectroscopy . . . . .	13
2.6.	MOT setup . . . . .	14
2.7.	magnetic field of quadrupole field in AH configuration . . . . .	17
2.8.	trapping atoms wiht a wire (chip trap) . . . . .	19
3.1.	experimental setup overview . . . . .	22
3.2.	laser types . . . . .	24
3.3.	$^{87}\text{Rb}$ D2 $F = 2$ DOPPLER valley . . . . .	26
3.4.	laser transitions . . . . .	28
3.5.	reflective imaging setup . . . . .	31
3.6.	main imaging setup . . . . .	32
3.7.	reflective imaging chip . . . . .	33
3.8.	overview MOT chamber . . . . .	34
3.9.	MOT live camera . . . . .	34
3.10.	rubidium dispenser . . . . .	35
3.11.	magnetic conveyor belt . . . . .	36
3.12.	switchbox . . . . .	37
3.13.	atom loss during transport . . . . .	39
3.14.	overview of cryogenic setup . . . . .	40
3.15.	ARS cryostat head . . . . .	41
3.16.	vacuum pumps . . . . .	42
3.17.	4 K heat shield . . . . .	43
3.18.	heat anchoring . . . . .	45
3.19.	short cut in cryostat . . . . .	46
3.20.	antennas in the experimental chamber . . . . .	47
3.21.	RF setup . . . . .	48
3.22.	superconducting atomchip . . . . .	49
3.23.	chip bonding . . . . .	51



List of Figures

---

3.24. Matlab interface . . . . .	52
3.25. Experimental Controller . . . . .	53
3.26. control voltages for round-trip transport . . . . .	53
4.1. atomchip loading sequence . . . . .	56
4.2. swing by maneuver during the atom chip loading . . . . .	56
4.3. trapping frequency quic . . . . .	58
4.4. trapping frequency chip . . . . .	59
4.5. trap bottom spectroscopy . . . . .	60
4.6. PSD increase . . . . .	62
4.7. RF knife . . . . .	63
4.8. probe stick . . . . .	64
4.9. co-planar wave guide resonators . . . . .	66
4.10. lumped element resonators . . . . .	66
5.1. current distribution depending on current history . . . . .	69
5.2. sketch of the chip trap . . . . .	70
5.3. current sequence for trap tailoring . . . . .	70
5.4. trap distance programming . . . . .	71
5.5. remanent current distribution for zero current . . . . .	72
6.1. aspect ratio change . . . . .	75
6.2. horizontal transport currents . . . . .	77
6.3. transport currents vertically . . . . .	78
6.4. magnetic transport calculator flowchart . . . . .	81
6.5. horizontal transport dynamics . . . . .	84
6.6. vertical transport dynamics . . . . .	85
6.7. time resolved SC transport current sequences . . . . .	86
6.8. temporally resolved NC transport current sequences . . . . .	87
6.9. recombination with magnetic conveyor belt . . . . .	88
6.10. recombination sequence attempt . . . . .	89
1. magnetic transport calculator interface . . . . .	94
2. magnetic transport calculator user input . . . . .	95
3. <sup>87</sup> Rb hyperfine ZEEMAN sublevels . . . . .	113

# List of Tables

4.1.	trapping frequencies parameters . . . . .	58
6.1.	coils to current sources and switch correspondence . . . . .	79
6.2.	truth labels for switch boxes . . . . .	80
6.3.	magnetic transport calculator parameters . . . . .	82
1.	g-factors . . . . .	111
2.	$g_F$ -factors . . . . .	112

# List of Symbols

## Acronyms / Abbreviations

AH anti-HELMHOLTZ

AOM acusto optical modulator

APD avalanche photo diode

BNC bayonet NEILL CONCELMAN

CF Ultra high vacuum sealed Conflat flange

CO Cross Over

CO cross over

CPW co-planar wave

DFB distributed feedback

DFS DOPPLER free spectroscopy

ECDL external cavity diode laser

EM electro magnetic

FWHM Full Width Half Maximum

MOT Magneto Optical Trap

MW microwave

NC normalconducting

NTC negative temperature coefficient

OIso Optical Isolator

PBS Polarizing Beam Splitter  
 PD Photo Diode  
 PID proportional integrational derivative  
 PSD phase space density  
 QED Quantum Electro Dynamic  
 QuIc Quantum Interconnect  
 quIC quadrupole IOFFE configuration  
 SC superconducting  
 TA tapered amplifier  
 TTL transistor transistor logic, digital family standard  
 UHV ultra high vacuum  
 VCO voltage controlled oscillator  
 YBCO Yttrium Barium Copper Oxide  
 BCS BARDEEN COOPER SCHIEFER

**Physical Symbols**

$A$  aspect ratio

$\mu_B$  BOHR-magneton  $\mu_B = \frac{e\hbar}{2m_e} \approx 9.274 \times 10^{-24} \text{ J T}^{-1}$

$\omega_L$  LARMOR-frequency

$\mathbf{F}$  total angular momentum

$\mathbf{J}$  total electron angular momentum

$\mathbf{L}$  orbital angular momentum

$\mathbf{S}$  electron spin

$\hat{\mathbf{F}}$  total angular momentum operator

$e$  elementary charge  $1.602 \times 10^{-19} \text{ C}$

## List of Tables

---

$\hbar$  reduced PLANCK-constant  $\frac{h}{2\pi} = 1.054\,57 \times 10^{-34}$  J s

$h$  PLANCK-constant  $6.626\,07 \times 10^{-34}$  J s

$\kappa$  thermal conductivity

$L_0$  LORENTZ-number  $L_0 \approx 2.45 \times 10^{-8}$  A<sup>2</sup> Ω<sup>2</sup> K<sup>-2</sup>

$\mu_0$  magnetic permeability of vacuum  $4\pi \times 10^{-7}$

$m_e$  electron mass  $9.109 \times 10^{-31}$  kg

$\rho$  electric resistivity

$T_D$  DEBYE-temperature

$T_D$  DOPPLER-limit

TOF time of flight

## Acknowledgements

This Document has devoured quite some of my time. However, writing its approximately 15000 lines of  $\LaTeX$ code, summarizing this extensive Diploma-thesis, has taught me a lot.

For the opportunity to do my Diploma-thesis in this group, I want to thank my professor JÖRG SCHMIEDMAYER as well as my supervisors STEFAN MINNIBERGER and FRITZ DIORICO. During the course of this work, I learned not only about quantum optics, ultra cold atoms, atom chips, lasers, cryogenics and superconductors, it was a lesson for life. I had the privilege to be a member of a very successful, active and supportive research group. I could visit two conferences and participate in one publication. For that, I am grateful to all current and previous members of the atomchip group, as well as the staff from the Institute for Atomic and Subatomic Physics in Vienna. Special thanks go to the low temperature group for letting us use their bath cryostats and the lithium experiment for being so considerate, in the difficult situation of sharing a lab.

For the fantastic working atmosphere in the QuIc experiment and interesting work I could do in more than 3000 hours, I thank the QuIc staff: FRITZ DIORICO, STEFAN MINNIBERGER, BENEDIKT GERSTENECKER, NAZ SHOKRANI and ŽANETA KURPIAS.

Finally, I owe them a great debt of gratitude to my family, godfather and friends for encouraging me on the endeavour of studying physics and supporting me in this pivotal and eventful phase of my life.

# References

- [1] J. Verdú, H. Zoubi, Ch. Koller, et al. “Strong magnetic coupling of an ultracold gas to a superconducting waveguide cavity”. In: *Physical Review Letters* 103.4 (2009), pp. 1–4. DOI: [10.1103/PhysRevLett.103.043603](https://doi.org/10.1103/PhysRevLett.103.043603).
- [2] Fritz Randulf S. Diorico. “Novel Atomchip Technologies with Superconductors”. [10.1016/j.aqpro.2013.07.003](https://doi.org/10.1016/j.aqpro.2013.07.003). PhD Thesis. Vienna: Technische Universität Wien, Oct. 2016. 159 pp.
- [3] Fritz Diorico, Stefan Minniberger, Thomas Weigner, et al. “Current-induced magnetization hysteresis defines atom trapping in a superconducting atomchip”. In: *SciPost Physics* 4.6 (June 22, 2018), p. 036. DOI: [10.21468/SciPostPhys.4.6.036](https://doi.org/10.21468/SciPostPhys.4.6.036).
- [4] Stefan Minniberger, Fritz Diorico, Stefan Haslinger, et al. “Magnetic conveyor belt transport of ultracold atoms to a superconducting atomchip”. In: *Applied Physics B* 116.4 (Sept. 2014), pp. 1017–1021. DOI: [10.1007/s00340-014-5790-5](https://doi.org/10.1007/s00340-014-5790-5).
- [5] M. H. Anderson, J. R. Ensher, M. R. Matthews, C. E. Wieman, and E. A. Cornell. “Observation of Bose-Einstein Condensation in a Dilute Atomic Vapor”. In: *Science* 269.5221 (July 14, 1995), pp. 198–201. DOI: [10.1126/science.269.5221.198](https://doi.org/10.1126/science.269.5221.198).
- [6] Ron Folman, Peter Krüger, Donatella Cassettari, et al. “Controlling Cold Atoms using Nanofabricated Surfaces: Atom Chips”. In: *Physical Review Letters* 84.20 (May 15, 2000), pp. 4749–4752. DOI: [10.1103/PhysRevLett.84.4749](https://doi.org/10.1103/PhysRevLett.84.4749).
- [7] J Bardeen, L N Cooper, and J R Schrieffer. “Theory of Superconductivity”. In: *Phys. Rev.* 108.8 (1957), pp. 1175–1204. DOI: <https://doi.org/10.1103/PhysRev.108.1175>.
- [8] H. J. Kimble. “The quantum internet”. In: *Nature* 453.7198 (June 2008), pp. 1023–1030. DOI: [10.1038/nature07127](https://doi.org/10.1038/nature07127).
- [9] Gavin Brennen, Elisabeth Giacobino, and Christoph Simon. “Focus on Quantum Memory”. In: *New Journal of Physics* 17.5 (May 6, 2015), p. 050201. DOI: [10.1088/1367-2630/17/5/050201](https://doi.org/10.1088/1367-2630/17/5/050201).
- [10] Richard P. Feynman. “Simulating physics with computers”. In: *International Journal of Theoretical Physics* 21.6-7 (1982), pp. 467–488. DOI: [10.1007/BF02650179](https://doi.org/10.1007/BF02650179).
- [11] David P. DiVincenzo. “Topics in Quantum Computers”. In: (Dec. 12, 1996).
- [12] M. H. Devoret and R. J. Schoelkopf. “Superconducting Circuits for Quantum Information: An Outlook”. In: *Science* 339.6124 (Mar. 8, 2013), pp. 1169–1174. DOI: [10.1126/science.1231930](https://doi.org/10.1126/science.1231930).

- 
- [13] Peter W. Shor. “Polynomial-Time Algorithms for Prime Factorization and Discrete Logarithms on a Quantum Computer”. In: *SIAM Journal on Computing* 26.5 (Oct. 1997), pp. 1484–1509. DOI: [10.1137/S0097539795293172](https://doi.org/10.1137/S0097539795293172).
- [14] R. J. Schoelkopf and S. M. Girvin. “Wiring up quantum systems”. In: *Nature* 451.7179 (Feb. 2008), pp. 664–669. DOI: [10.1038/451664a](https://doi.org/10.1038/451664a).
- [15] Ze-Liang Xiang, Sahel Ashhab, J. Q. You, and Franco Nori. “Hybrid quantum circuits: Superconducting circuits interacting with other quantum systems”. In: *Reviews of Modern Physics* 85.2 (Apr. 9, 2013), pp. 623–653. DOI: [10.1103/RevModPhys.85.623](https://doi.org/10.1103/RevModPhys.85.623).
- [16] T. Astner, J. Gugler, A. Angerer, et al. “Solid-state electron spin lifetime limited by phononic vacuum modes”. In: *Nature Materials* 17.4 (Apr. 2018), pp. 313–317. DOI: [10.1038/s41563-017-0008-y](https://doi.org/10.1038/s41563-017-0008-y).
- [17] David Petrosyan, Guy Bensky, Gershon Kurizki, et al. “Reversible state transfer between superconducting qubits and atomic ensembles”. In: *Physical Review A* 79.4 (Apr. 14, 2009). DOI: [10.1103/PhysRevA.79.040304](https://doi.org/10.1103/PhysRevA.79.040304).
- [18] Kathrin Henschel, Johannes Majer, Jörg Schmiedmayer, and Helmut Ritsch. “Cavity QED with an ultracold ensemble on a chip: Prospects for strong magnetic coupling at finite temperatures”. In: *Physical Review A* 82.3 (Sept. 13, 2010). DOI: [10.1103/PhysRevA.82.033810](https://doi.org/10.1103/PhysRevA.82.033810).
- [19] *Karlsruher Nuklidkarte*. In collab. with J. Magill, Gerda Pfennig, and J. Galy. 2006.
- [20] Daniel A. Steck. *Rubidium 87 D Line Data*. 2001.
- [21] Daniel A. Steck. *Rubidium 85 D Line Data*. 2001.
- [22] E. Arimondo, M. Inguscio, and P. Violino. “Experimental determinations of the hyperfine structure in the alkali atoms”. In: *Reviews of Modern Physics* 49.1 (Jan. 1, 1977), pp. 31–75. DOI: [10.1103/RevModPhys.49.31](https://doi.org/10.1103/RevModPhys.49.31).
- [23] G. Breit and I. I. Rabi. “Measurement of Nuclear Spin”. In: *Physical Review* 38.11 (1931), pp. 2082–2083. DOI: [10.1103/PhysRev.38.2082.2](https://doi.org/10.1103/PhysRev.38.2082.2).
- [24] D. M. Harber, H. J. Lewandowski, J. M. McGuirk, and E. A. Cornell. “Effect of cold collisions on spin coherence and resonance shifts in a magnetically trapped ultracold gas”. In: *Physical Review A* 66.5 (Nov. 22, 2002). DOI: [10.1103/PhysRevA.66.053616](https://doi.org/10.1103/PhysRevA.66.053616).
- [25] Philipp Treutlein, Peter Hommelhoff, Tilo Steinmetz, Theodor W. Hänsch, and Jakob Reichel. “Coherence in Microchip Traps”. In: *Physical Review Letters* 92.20 (May 21, 2004). DOI: [10.1103/PhysRevLett.92.203005](https://doi.org/10.1103/PhysRevLett.92.203005).
- [26] T W Hänsch and A L Schawlow. “Cooling of Gases by Laser Radiation”. In: *Optics Communications* 13.I (1975), pp. 68–69.
- [27] S. Abend, M. Gebbe, M. Gersemann, et al. “Atom-Chip Fountain Gravimeter”. In: *Physical Review Letters* 117.20 (Nov. 11, 2016). DOI: [10.1103/PhysRevLett.117.203003](https://doi.org/10.1103/PhysRevLett.117.203003).



- 
- [28] K. N. Jarvis, J. A. Devlin, T. E. Wall, B. E. Sauer, and M. R. Tarbutt. “Blue-Detuned Magneto-Optical Trap”. In: *Physical Review Letters* 120.8 (Feb. 20, 2018). DOI: [10.1103/PhysRevLett.120.083201](https://doi.org/10.1103/PhysRevLett.120.083201).
- [29] Daryl W Preston. “Doppler free saturated absorption Laser spectroscopy”. In: *American Journal of Physics* 64.11 (1996), pp. 1432–1436. DOI: [10.1119/1.18457](https://doi.org/10.1119/1.18457).
- [30] P. D. Lett, W. D. Phillips, S. L. Rolston, et al. “Optical molasses”. In: *JOSA B* 6.11 (Nov. 1, 1989), pp. 2084–2107. DOI: [10.1364/JOSAB.6.002084](https://doi.org/10.1364/JOSAB.6.002084).
- [31] J. Dalibard and C. Cohen-Tannoudji. “Laser cooling below the Doppler limit by polarization gradients: simple theoretical models”. In: *Journal of the Optical Society of America B* 6.11 (1989), p. 2023. DOI: [10.1364/JOSAB.6.002023](https://doi.org/10.1364/JOSAB.6.002023).
- [32] A. Ashkin and J. P. Gordon. “Stability of radiation-pressure particle traps: an optical Earnshaw theorem”. In: *Optics Letters* 8.10 (Oct. 1, 1983), pp. 511–513. DOI: [10.1364/OL.8.000511](https://doi.org/10.1364/OL.8.000511).
- [33] S Earnshaw. “On the nature of the molecular forces which regulate the constitution of the luminiferous ether”. In: 7 (1848), pp. 97–112.
- [34] Wolfgang Petrich, Michael H. Anderson, Jason R. Ensher, and Eric A. Cornell. “Stable, Tightly Confining Magnetic Trap for Evaporative Cooling of Neutral Atoms”. In: *Physical Review Letters* 74.17 (Apr. 24, 1995), pp. 3352–3355. DOI: [10.1103/PhysRevLett.74.3352](https://doi.org/10.1103/PhysRevLett.74.3352).
- [35] Tilman Esslinger, Immanuel Bloch, and Theodor W. Hansch. “Bose Einstein condensate in a quadrupole Ioffe configuration trap”. In: *Physical Review A* 58.4 (1998), pp. 2664–2667. DOI: [10.1103/PhysRevA.58.R2623](https://doi.org/10.1103/PhysRevA.58.R2623).
- [36] Jörg Schmiedmayer. “Guiding and trapping a neutral atom on a wire”. In: *Physical Review A* 52.1 (July 1, 1995), R13–R16. DOI: [10.1103/PhysRevA.52.R13](https://doi.org/10.1103/PhysRevA.52.R13).
- [37] Markus Bartenstein, Donatella Cassettari, Tommaso Calarco, et al. “Atoms and wires: Toward atom chips”. In: *IEEE Journal of Quantum Electronics* 36.12 (2000), pp. 1364–1376. DOI: [10.1109/3.892555](https://doi.org/10.1109/3.892555).
- [38] S. Groth, P. Krüger, S. Wildermuth, et al. “Atom chips: Fabrication and thermal properties”. In: *Applied Physics Letters* 85.14 (Oct. 4, 2004), pp. 2980–2982. DOI: [10.1063/1.1804601](https://doi.org/10.1063/1.1804601).
- [39] T. Schumm, S. Hofferberth, L. M. Andersson, et al. “Matter-wave interferometry in a double well on an atom chip”. In: *Nature Physics* 1.1 (Oct. 2005), pp. 57–62. DOI: [10.1038/nphys125](https://doi.org/10.1038/nphys125).
- [40] M. Gring, M. Kuhnert, T. Langen, et al. “Relaxation and Prethermalization in an Isolated Quantum System”. In: *Science* (Sept. 6, 2012), p. 1224953. DOI: [10.1126/science.1224953](https://doi.org/10.1126/science.1224953).
- [41] Tim Langen, Sebastian Erne, Remi Geiger, et al. “Experimental observation of a generalized Gibbs ensemble”. In: *Science* 348.6231 (Apr. 10, 2015), pp. 207–211. DOI: [10.1126/science.1257026](https://doi.org/10.1126/science.1257026).

- 
- [42] Thomas Schweigler, Valentin Kasper, Sebastian Erne, et al. “Experimental characterization of a quantum many-body system via higher-order correlations”. In: *Nature* 545.7654 (May 2017), pp. 323–326. DOI: [10.1038/nature22310](https://doi.org/10.1038/nature22310).
- [43] T. Arpornthip, C. A. Sackett, and K. J. Hughes. “Vacuum Pressure Measurements using a Magneto-Optical Trap”. In: *Physical Review A* 85.3 (Mar. 16, 2012). DOI: [10.1103/PhysRevA.85.033420](https://doi.org/10.1103/PhysRevA.85.033420).
- [44] A. J. Moerdijk, H. M. J. M. Boesten, and B. J. Verhaar. “Decay of trapped ultracold alkali atoms by recombination”. In: *Physical Review A* 53.2 (Feb. 1, 1996), pp. 916–920. DOI: [10.1103/PhysRevA.53.916](https://doi.org/10.1103/PhysRevA.53.916).
- [45] Wolfgang Ketterle and N. J. Van Druten. “Evaporative Cooling of Trapped Atoms”. In: *Advances In Atomic, Molecular, and Optical Physics* 37 (Jan. 1, 1996). Ed. by Benjamin Bederson and Herbert Walther, pp. 181–236. DOI: [10.1016/S1049-250X\(08\)60101-9](https://doi.org/10.1016/S1049-250X(08)60101-9).
- [46] Ulrich Hohenester, Asier Eiguren, Stefan Scheel, and E. A. Hinds. “Spin-flip lifetimes in superconducting atom chips: Bardeen-Cooper-Schrieffer versus Eliashberg theory”. In: *Physical Review A* 76.3 (Sept. 21, 2007). DOI: [10.1103/PhysRevA.76.033618](https://doi.org/10.1103/PhysRevA.76.033618).
- [47] S. Scheel, P. K. Rekdal, P. L. Knight, and E. A. Hinds. “Atomic spin decoherence near conducting and superconducting films”. In: *Physical Review A* 72.4 (Oct. 11, 2005). DOI: [10.1103/PhysRevA.72.042901](https://doi.org/10.1103/PhysRevA.72.042901).
- [48] B. Kasch, H. Hattermann, D. Cano, et al. “Cold atoms near superconductors: Atomic spin coherence beyond the Johnson noise limit”. In: *New Journal of Physics* 12.6 (June 28, 2010), p. 065024. DOI: [10.1088/1367-2630/12/6/065024](https://doi.org/10.1088/1367-2630/12/6/065024).
- [49] R Fermani, T Müller, B Zhang, M J Lim, and R Dumke. “Heating rate and spin flip lifetime due to near-field noise in layered superconducting atom chips”. In: *Journal of Physics B: Atomic, Molecular and Optical Physics* 43.9 (May 14, 2010), p. 095002. DOI: [10.1088/0953-4075/43/9/095002](https://doi.org/10.1088/0953-4075/43/9/095002).
- [50] Stefan Minniberger. “Ultracold atoms on superconducting atomchips”. PhD Thesis. Vienna: Technische Universität Wien, 2018.
- [51] A L Schawlow and C H Townes. “Infrared and Optical Masers”. In: *Phys. Rev.* 112.6 (1958), pp. 1940–1949. DOI: [10.1103/PhysRev.112.1940](https://doi.org/10.1103/PhysRev.112.1940).
- [52] Walter Koechner and Michael Bass. *Solid-State Lasers, A graduate Text*. 1st ed. New York: Springer Verlag, 2003.
- [53] Christopher Palmer and Erwin Loewen. *Diffraction Grating Handbook*. 6th ed. New York: Newport Coperation, 2004.
- [54] H. Kogelnik and C. V. Shank. “Coupled Wave Theory of Distributed Feedback Lasers”. In: *Journal of Applied Physics* 43.5 (1972), pp. 2327–2335. DOI: [10.1063/1.1661499](https://doi.org/10.1063/1.1661499).
- [55] H. Kogelnik and C. V. Shank. “Stimulated Emission in a Periodic Structure”. In: *Applied Physics Letters* 18.4 (1971), pp. 152–154. DOI: [10.1063/1.1653605](https://doi.org/10.1063/1.1653605).

- 
- [56] Carl E Wieman and Leo Hollberg. “Using diode lasers for atomic physics”. In: *Rev. Sci. Instrum.* 62.1 (1991), p. 20.
- [57] Thomas Angerler. “Building and alignment of an ECDL- and a DFB-laser set-up for a laser-cooling experiment of Rubidium 87”. Bachelor Thesis. Vienna: Technische Universität Wien, 2017.
- [58] U. Schünemann, H. Engler, R. Grimm, M. Weidemüller, and M. Zielonkowski. “Simple scheme for tunable frequency offset locking of two lasers”. In: *Review of Scientific Instruments* 70.1 (Jan. 1999), pp. 242–243. DOI: [10.1063/1.1149573](https://doi.org/10.1063/1.1149573).
- [59] Benedikt Gerstenecker. “Tailoring trap current distributions in superconducting atomchips”. Diploma Thesis. Vienna: Technische Universität Wien, 2017.
- [60] Christoph Hufnagel. “Superconducting microtraps for ultracold atoms”. PhD Thesis. Vienna: Technische Universität Wien, 2011.
- [61] Robert Amsüss. “Development of a Source of Ultracold Atoms for Cryogenic Environments”. Diploma Thesis. Vienna: Technische Universität Wien, 2008.
- [62] Nils Lippok. “A Magnetic Transport for Ultracold Atoms - 2008 - N.Lippok”. Diploma Thesis. Vienna: Technische Universität Wien, 2008.
- [63] Markus Greiner, Immanuel Bloch, Theodor W. Hänsch, and Tilman Esslinger. “Magnetic transport of trapped cold atoms over a large distance”. In: *Physical Review A* 63.3 (Feb. 9, 2001). DOI: [10.1103/PhysRevA.63.031401](https://doi.org/10.1103/PhysRevA.63.031401).
- [64] Stefan Haslinger. “Cold Atoms in a Cryogenic Environment”. PhD Thesis. Vienna: Technische Universität Wien, 2011.
- [65] Christian Novotny. “Transport of ultracold atoms into a superconducting QuIC-Trap”. Diploma Thesis. Vienna: Technische Universität Wien, 2011.
- [66] V. R. Karasik and I. Y. Shebalin. “Superconducting properties of pure niobium”. In: *Sov-Phys JETP* 30.6 (1970), pp. 1068–1076.
- [67] R. Franz and G. Wiedemann. “Über die Wärme-Leitungsfähigkeit der Metalle”. In: *Annalen der Physik und Chemie* 89.8 (1853), pp. 497–531. DOI: [10.1002/andp.18531650802](https://doi.org/10.1002/andp.18531650802).
- [68] P. Drude. “Zur Elektronentheorie der Metalle”. In: *Annalen der Physik* 306.3 (1900), pp. 566–613. DOI: [10.1002/andp.19003060312](https://doi.org/10.1002/andp.19003060312).
- [69] J. G. Weisend. *Handbook of Cryogenic Engineering*. Taylor and Francis, 1998.
- [70] A. C. Leuthold and R. T. Wakai. “Superconducting wire contact to niobium thin films”. In: *Cryogenics* 35.2 (Jan. 1, 1995), pp. 149–150. DOI: [10.1016/0011-2275\(95\)92884-U](https://doi.org/10.1016/0011-2275(95)92884-U).
- [71] James R. B. Garfield. “Superconducting contacts for use in niobium thin film applications”. In: *Review of Scientific Instruments* 68.4 (Apr. 1997), pp. 1906–1907. DOI: [10.1063/1.1147965](https://doi.org/10.1063/1.1147965).
- [72] Qi Liang. “PHD Thesis, in preparation”. PhD Thesis. TU Wien, 2019.

- 
- [73] C. Roux, A. Emmert, A. Lupascu, et al. “Bose-Einstein condensation on a superconducting atom chip”. In: *EPL (Europhysics Letters)* 81.5 (Mar. 2008), p. 56004. DOI: [10.1209/0295-5075/81/56004](https://doi.org/10.1209/0295-5075/81/56004).
- [74] Bose, Satyendranath. “Plancks Gesetz und Lichtquantenhypothese.” In: *Z.Phys.* 26 (1924), pp. 178–181.
- [75] Albert Einstein. “Quantentheorie des einatomigen idealen Gases (zweite Abhandlung)”. In: *Sitzungsberichte der Preussischen Akademie der Wissenschaften* 1 (1924), pp. 261–267.
- [76] Albert Einstein. “Quantentheorie des einatomigen idealen Gases (erste Abhandlung)”. In: *Sitzungsberichte der Preussischen Akademie der Wissenschaften* 2 (1925), pp. 245–257.
- [77] C.J. Pethick and H. Smith. *Bose Einstein Condensation in Dillute Gases*. 2nd. Cambridge: Cambridge University Press, 2001.
- [78] Louis V. de Broglie. “The wave nature of the electron”. In: *Nobel lectures, Physics 1922-1941* (1929), pp. 244–256.
- [79] W. J. Mullin. “Bose-Einstein condensation in a harmonic potential”. In: *Journal of Low Temperature Physics* 106.5-6 (Mar. 1997), pp. 615–641. DOI: [10.1007/BF02395928](https://doi.org/10.1007/BF02395928).
- [80] E. A. L. Henn, J. A. Seman, G. B. Seco, et al. “Bose-Einstein condensation in 87Rb: characterization of the Brazilian experiment”. In: *Brazilian Journal of Physics* 38.2 (June 2008), pp. 279–286. DOI: [10.1590/S0103-97332008000200012](https://doi.org/10.1590/S0103-97332008000200012).
- [81] Christian Koller. “Towards the realization of hybrid quantum systems”. PhD Thesis. Vienna: Technische Universität Wien, 2012.
- [82] A. A. Abrikosov. “Nobel Lecture: Type-II superconductors and the vortex lattice”. In: *Reviews of Modern Physics* 76.3 (Dec. 2, 2004), pp. 975–979. DOI: [10.1103/RevModPhys.76.975](https://doi.org/10.1103/RevModPhys.76.975).
- [83] Charles P. Bean. “Magnetization of hard superconductors”. In: *Physical Review Letters* 8.6 (1962), pp. 250–253. DOI: [10.1103/PhysRevLett.8.250](https://doi.org/10.1103/PhysRevLett.8.250).
- [84] Charles P. Bean. “Magnetization of high-field superconductors”. In: *Reviews of Modern Physics* 36.1 (1964), pp. 31–39. DOI: [10.1103/RevModPhys.36.31](https://doi.org/10.1103/RevModPhys.36.31).
- [85] Ernst Helmut Brandt and Mikhail Indenbom. “Type-II-superconductor strip with current in a perpendicular magnetic field”. In: *Physical Review B* 48.17 (Nov. 1, 1993), pp. 12893–12906. DOI: [10.1103/PhysRevB.48.12893](https://doi.org/10.1103/PhysRevB.48.12893).
- [86] T. Müller, B. Zhang, R. Fermani, et al. “Programmable trap geometries with superconducting atom chips”. In: *Physical Review A* 81.5 (May 24, 2010). DOI: [10.1103/PhysRevA.81.053624](https://doi.org/10.1103/PhysRevA.81.053624).
- [87] T Müller, B Zhang, R Fermani, et al. “Trapping of ultra-cold atoms with the magnetic field of vortices in a thin-film superconducting micro-structure”. In: *New Journal of Physics* 12.4 (Apr. 13, 2010), p. 043016. DOI: [10.1088/1367-2630/12/4/043016](https://doi.org/10.1088/1367-2630/12/4/043016).

- 
- [88] B. Zhang, R. Fermani, T. Müller, M. J. Lim, and R. Dumke. “Design of magnetic traps for neutral atoms with vortices in type-II superconducting microstructures”. In: *Physical Review A* 81.6 (June 8, 2010). DOI: [10.1103/PhysRevA.81.063408](https://doi.org/10.1103/PhysRevA.81.063408).
- [89] B. Zhang, M. Siercke, K. S. Chan, et al. “Magnetic confinement of neutral atoms based on patterned vortex distributions in superconducting disks and rings”. In: *Physical Review A* 85.1 (Jan. 4, 2012). DOI: [10.1103/PhysRevA.85.013404](https://doi.org/10.1103/PhysRevA.85.013404).
- [90] M. Siercke, K. S. Chan, B. Zhang, et al. “Reconfigurable self-sufficient traps for ultracold atoms based on a superconducting square”. In: *Physical Review A* 85.4 (Apr. 23, 2012). DOI: [10.1103/PhysRevA.85.041403](https://doi.org/10.1103/PhysRevA.85.041403).
- [91] Naz Shokrani. “Exploring Field-Induced Remanent Magnetization Traps for Ultracold Atoms on a Niobium Atomchip”. Diploma Thesis. Vienna: Technische Universität Wien, 2018.
- [92] Christoph Hufnagel, Tetsuya Mukai, and Fujio Shimizu. “Stability of a superconductive atom chip with persistent current”. In: *Physical Review A* 79.5 (May 29, 2009). DOI: [10.1103/PhysRevA.79.053641](https://doi.org/10.1103/PhysRevA.79.053641).
- [93] Jesper Fevre Bertelsen, Henrik Kjaer Andersen, Sune Mai, and Michael Budde. “Mixing of ultracold atomic clouds by merging of two magnetic traps”. In: *Physical Review A* 75.1 (Jan. 4, 2007). DOI: [10.1103/PhysRevA.75.013404](https://doi.org/10.1103/PhysRevA.75.013404).
- [94] Stefan Reuter. “Magnetic Transport and Recombination of an Atomic Cloud”. Bachelor Thesis. Vienna: Technische Universität Wien, 2017.
- [95] James Simpson, John Lane, Christopher Immer, and Robert Youngquist. *Simple Analytic Expressions for the Magnetic Field of a Circular Current Loop*. 20010038494. NASA, 2001.
- [96] Lukas Achatz and Dominik Ilk. “Magnetic coupling of ultracold Rubidium 87 atoms with a superconducting atom chip”. Bachelor Thesis. Vienna: Technische Universität Wien, 2015.
- [97] H. J. Lewandowski, D. M. Harber, D. L. Whitaker, and E. A. Cornell. “Simplified System for Creating a Bose–Einstein Condensate”. In: *Journal of Low Temperature Physics* 132.5 (Sept. 1, 2003), pp. 309–367. DOI: [10.1023/A:1024800600621](https://doi.org/10.1023/A:1024800600621).
- [98] T. Nirrengarten, A. Qarry, C. Roux, et al. “Realization of a Superconducting Atom Chip”. In: *Physical Review Letters* 97.20 (Nov. 17, 2006). DOI: [10.1103/PhysRevLett.97.200405](https://doi.org/10.1103/PhysRevLett.97.200405).
- [99] O. Romero-Isart, C. Navau, A. Sanchez, P. Zoller, and J. I. Cirac. “Superconducting vortex lattices for ultracold atoms”. In: *Physical Review Letters* 111.14 (2013), pp. 1–16. DOI: [10.1103/PhysRevLett.111.145304](https://doi.org/10.1103/PhysRevLett.111.145304).
- [100] A. Emmert, A. Lupaşcu, G. Nogues, et al. “Measurement of the trapping lifetime close to a cold metallic surface on a cryogenic atom-chip”. In: *The European Physical Journal D* 51.2 (Feb. 2009), pp. 173–177. DOI: [10.1140/epjd/e2009-00001-5](https://doi.org/10.1140/epjd/e2009-00001-5).

## References

---

- [101] D. Cano, B. Kasch, H. Hattermann, et al. “Impact of the Meissner effect on magnetic microtraps for neutral atoms near superconducting thin films”. In: *Physical Review A* 77.6 (June 5, 2008), p. 063408. DOI: [10.1103/PhysRevA.77.063408](https://doi.org/10.1103/PhysRevA.77.063408).